Combustion, Heat Transfer and Soot Formation in Biomass-Burning Cookstoves

Anamol Pundle

A dissertation
submitted in partial fulfillment of the
requirements for the degree of

Doctor of Philosophy

University of Washington

2019

Reading Committee:
John C. Kramlich, Chair
Jonathan D. Posner, Chair
James J. Riley

Program Authorized to Offer Degree:
Department of Mechanical Engineering

University of Washington

Abstract

Combustion, Heat Transfer and Soot Formation in Biomass-Burning Cookstoves

Anamol Pundle

Chairs of the Supervisory Committee:

Professor John C. Kramlich
Department of Mechanical Engineering

Professor Jonathan D. Posner
Department of Mechanical Engineering

Over three billion people in the world rely on biomass for their cooking and heating needs. Indoor cooking using biomass has been identified as a significant contributor to cancer, respiratory illnesses and cardiovascular ailments in humans, resulting in over four million premature deaths every year. Improved biomass cookstoves that are more energy efficient and emit less particulate matter may help mitigate this public health crisis. This work examines combustion, fluid flow, and heat transfer in biomass-burning cookstoves, and soot formation in turbulent ethylene flames impinging on a cookpot, a simplified configuration that allows study of particulate matter behavior during the interaction of a flame with a cold surface. The goal of this work is to develop generalizable results and methodologies for understanding and predicting the performance of biomass-burning cookstoves.

A two-dimensional steady-state axisymmetric CFD model of a natural-draft, biomass-burning cookstove is developed. The model includes coupled sub-models representing combustion, turbulence, and heat transfer. The model is validated against experimental data and used to predict temperatures and flow inside the cookstove, including the airflow rate through the cookstove and heat transfer to the cookpot. Excess air is found to be typically many times stoichiometric air during standard operating conditions and is sensitive to flow field obstructions. The effects of geometric and operational features such as the pot support height, secondary air entrainment, cone-deck shape, and baffle placement within the cookstove on the flow, airflow rate, mixing, and stove thermal efficiency are analyzed. The model shows that secondary air entrainment, though ineffective by itself, increases turbulent mixing when used in conjunction with a central baffle but reduces thermal efficiencies due to enhanced heat transfer to the walls. Thirty-six cone-deck configurations are modeled, and it is found that the cone-deck shape primarily affects the airflow rate through the stove, with more constricted designs leading to higher thermal efficiencies. The modeling shows that merely restricting the airflow is not a sufficient condition for increasing the thermal efficiency; different constrictions resulted in different thermal efficiencies. A similar mathematical model is applied to three variations of a three-dimensional geometry representing a real cookstove to study the effects of secondary air entrainment. The results show that a choke ring just upstream of the riser leads to relatively well-mixed flow in the riser. Secondary air from cut-outs in the front of the stove of all three configurations is found to be ineffective for entraining air into the combustion chamber but is effective for cooling the front of the combustion chamber, possibly increasing the durability of the cookstove.

Soot formation is investigated experimentally in turbulent non-premixed ethylene flames impinging on a cold surface, which is a combustion configuration closely related to the biomass-burning cookstove. The cold surface is a stainless-steel receptacle containing water maintained at the boiling point (373 K). The jet diameter, jet velocity, and the distance of the surface the flame impinges from the jet nozzle is varied. Soot mass emissions are measured using a tapered element oscillating microbalance (TEOM) and size distributions using a scanning mobility particle sizer (SMPS). For free flames, both the soot yield factor and the mean aerodynamic diameter are strongly correlated with Richardson's ratio and the jet exit strain rate. The particle size distribution of soot emitted from free flames is found to be bimodal at low jet exit strain rates and tends towards unimodal distributions as the strain rate is increased. When impinging on the cold surface, it is observed that for most flames the soot yield factor initially increases with non-dimensional surface height h* (defined as the surface height divided by the flame length), reaches a maximum when the surface is at approximately half the flame height, and then decreases. The particle size distributions of emitted soot for nearly all configurations are found to be bimodal.

A two-dimensional axisymmetric CFD model is developed in order to gain insight into the soot formation process and to understand and interpret the experimental results obtained. Combustion is modeled by the non-premixed, non-adiabatic flamelet method and soot formation modeled by the Method of Moments by Interpolative Closure, with oxidation by O_2 modeled by the method developed by Khosousi et al., based on the thermal age of soot particles. The model's predictions are compared with in-flame soot and temperature data from literature. The model correctly predicts the trend of increasing, then decreasing soot mass emissions from a flame impinging on a pot, but consistently under-predicts soot mass

emissions. The model is also found to be sensitive to a parameter in the formulation of the thermal age-based oxidation model, $T_{a,max}$, the value of the thermal age at the point of maximum soot volume fraction.

In order to understand the increase in soot mass emissions when a cold surface is placed in the flame, the environment experienced by soot particles in a representative flame with and without a cold surface is explored. The path traced by a particle exhibiting maximum soot in both configurations is considered. Analyzing the oxidation and surface growth along these pathlines shows that both processes are essentially concluded by a residence time of 30 ms. Surface growth for both configurations reaches a maximum at approximately the same residence time but falls much quicker for the free flame. Oxidation for the free flame reaches a higher peak value, and the absence of the pot results in greater oxidation. These two effects of greater soot surface growth and reduced soot oxidation lead to increased soot emission when a pot is present as opposed to a free flame. The increasing, then decreasing trend of soot emission with increasing pot height is investigated by analyzing the soot surface growth term for a representative flame. A lower surface height causes surface growth to be disrupted, leading to a lower mass of soot generated and emitted.

Acknowledgements

I would like to take this opportunity to express my deepest gratitude to my advisor John C. Kramlich who provided guidance, wisdom and support (as well as numerous cups of coffee) during the course of my PhD. This work truly could not have been possible without him. I would also like to express my gratitude to my co-advisor Jonathan D. Posner for his support and guidance, especially on clearly communicating ideas in written and verbal form. I am a better researcher owing to his guidance. I wish to thank James J. Riley for his valuable lessons on turbulence modeling and also for serving on my committee. I would like to thank James C. Hermanson for serving on my committee and for his valuable inputs. In addition, I would also like to thank Philip C. Malte who advised me during my Master's degree and from whom I learnt the fundamentals of the science of combustion.

I wish to thank my fellow graduate students and labmates Devin Udesen, Benjamin Sullivan, Garrett Allawatt and Roytor Charoensin-O-Larn for their help and support. I appreciate the countless discussions we had and the hours we spent working on advancing cookstove technology. I would also like to thank the staff at the Department of Mechanical Engineering, especially Wanwisa Kisalang for her unlimited support as my graduate academic advisor.

This work was financially supported by the Department of Mechanical Engineering and the US Department of Energy through the BETO Clean Cookstoves Program. Additional financial support was provided by Intellectual Ventures through their Global Good Fund.

Lastly, I would like to thank my family and friends for their unending love, support and encouragement throughout my time at the University of Washington.

Table of Contents

List of Figures

List of Tables

Chapter 1 : Introduction

1.1 Overview and Motivation

Nearly three billion people, largely in regions of Africa and Southeast Asia, depend on biomass for their cooking needs [1]. Cooking with biomass produces particulate matter, which has been identified as a significant contributor to cancer, respiratory diseases, and cardiovascular ailments. Women and children are disproportionally affected because the vast majority of cooking in developing countries is performed by women in the presence of their children [2]. Indoor air pollution has been estimated to contribute to over 4 million deaths every year [3], much of which is attributed to biomass combustion. Biomass combustion also contributes to climate change through the emission of greenhouse gases and black carbon, which is considered to be the second most important contributing species to climate change after CO_2 [4]. About 25% of the worldwide black carbon emission is due to biomass combustion [5]. Gathering wood for fuel contributes to deforestation, and the scarcity of wood fuel is a growing problem in several developing countries [6].

Figure 1.1: Biomass burning improved natural draft cookstoves

The health and environmental impacts of cooking with rudimentary biomass stoves and 'three stone fires', so named due to three stones being used to support the cookpot under which biomass fuel is burned, drive the need to develop low emission, high efficiency improved cookstoves. A commonly used improvement is a natural draft, biomass burning cookstove called a 'rocket' stove. Several rocket cookstoves are shown in Figure 1.1. These stoves typically consist of a cylindrical shell that encloses the fire, with the combustion gas being directed towards the cookpot that sits atop the cylinder. The fuel is introduced through an opening in the side of the combustion chamber. The performance of these cookstoves is usually established through testing guidelines developed by the International Standards

Organization (ISO). The ISO 19867-1:2018 guidelines provide a 4-tier system for cookstove performance (1 being the lowest level of performance and 4 being the highest), measured using the Water Boiling Test protocol [7]. Performance parameters measured include fuel use (thermal efficiency), emissions (CO, $PM_{2.5}$) and indoor emissions (CO, $PM_{2.5}$). Jetter et al. [8] examined the laboratory performance of 22 different cookstoves and a three stone fire burning six kinds of fuel. Several rocket stoves showed significant improvements in thermal efficiency, combustion efficiency and pollutant emissions over the three stone fire; however, improvements still need to be made to natural draft stoves' $PM_{2.5}$ emissions and thermal efficiency to meet the WHO recommended guidelines. The problem is exacerbated by the fact that field performance is generally much worse than lab performance. Roden et al. [9] found that, on average, $PM_{2.5}$ emission factors measured in the field were over three times larger than laboratory measured $PM_{2.5}$ emission factors for the same cookstove. In a 2007 study, Smith el al. [10] investigated three sites where improved cookstoves were introduced, and found that the site with the lowest ambient $PM_{2.5}$ concentration exceeded WHO guidelines by a factor of ten.

Stoves are often designed using an iterative process, i.e., building a prototype, testing it, then refining stove parameters until an acceptable design is found [11]. This process is resource intensive, time consuming, and does not provide insight into the physics governing the performance of the cookstove. Computational modeling can serve as a complement to iterative design in order to reduce time and resources required to meet the target goals of a particular stove. Numerical models can also provide details about physical processes inside the cookstove, the knowledge of which can be used by stove designers to design better performing cookstoves. The effect of geometric parameters on combustion and mixing may

also be studied without undergoing the expensive and time-consuming process of building and testing cookstoves.

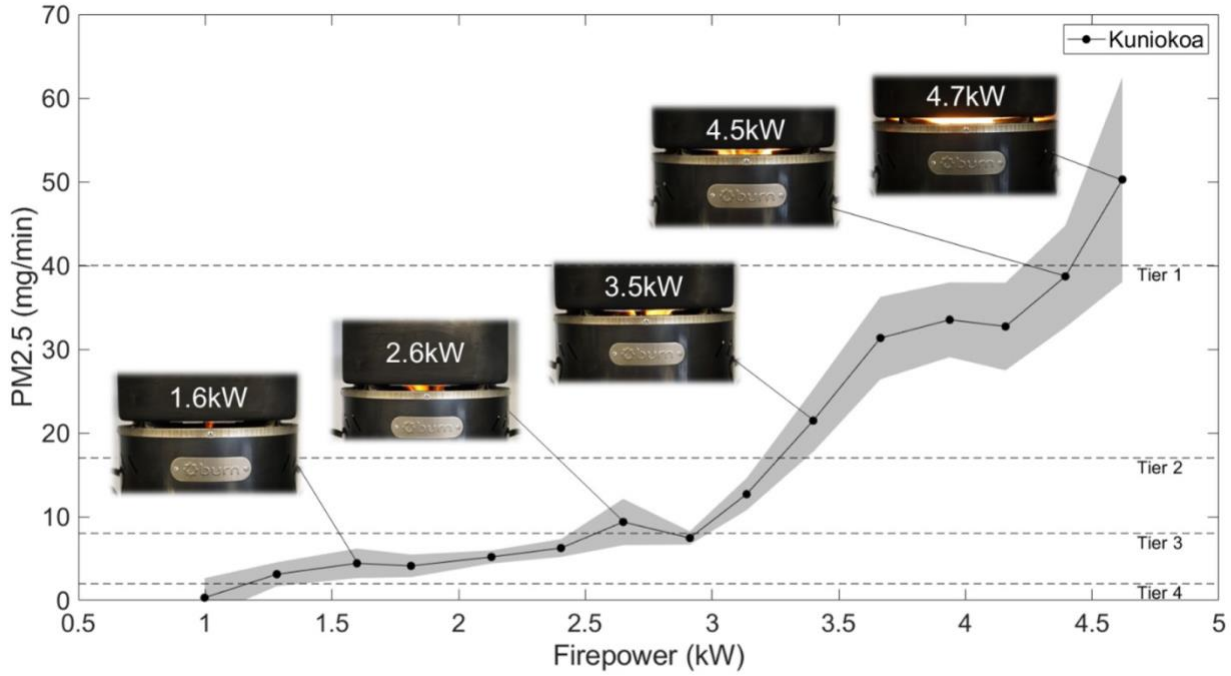

Figure 1.2: Soot emission from the BURN Kuniokoa as a function of firepower taken from Udesen [12].

An example where numerical simulation may help explain a physical process occurring in natural draft rocket cookstoves is shown in Figure 1.2, which shows a plot of soot emitted from the BURN Kuniokoa rocket stove, a natural draft, wood-burning cookstove as a function of its heating rate, or firepower [12]. Soot emission stays low and varies linearly with firepower until approximately 3 kW. Firepowers greater than 3 kW result in a substantial increase in the rate of soot emission. This point of inflection in the curve corresponds to the firepower at which the flame contacts the bottom of the cookpot, observed visually. However, analyses of soot emission and soot formation mechanisms for this fundamental configuration have not been reported in the literature. In this case,

numerical simulation can help explain the physical processes responsible for the increase in the rate of soot emission with increasing firepower.

1.2 Literature Review

The relevant literature can be separated into studies regarding previous cookstove modeling efforts, soot formation mechanisms in flames, soot emissions from non-premixed flames and biomass-burning cookstoves, and mathematical models for predicting soot in flames.

1.2.1 Previous Cookstove Modeling Efforts

While much research and development has been done on improved biomass burning cookstoves, very little of it has been focused on numerical simulation and modeling. In the last 30 years (as of 2018), out of over 500 journal articles published on cookstove development, fewer than 30 have focused on numerical modeling [13]. Early modeling work was done by Baldwin [14] who developed a steady-state heat transfer model to study how the geometry of the channel between the cookpot and pot skirt influenced the heat transferred to the cookpot. Combustion was not modeled, but rather the combustion zone was assumed to be uniform at 700 K, with convective and radiative heat transfer coefficients for the walls calculated using empirical correlations. 20% of the heating value of the fuel was assumed to go to the bottom of the pot, while the heat transfer to the side of the pot was calculated by discretizing the channel gap between the pot skirt and the pot, and calculating the heat transferred to each segment of the pot, assuming the temperature at the beginning of channel to be 900 K. The temperature drop as the gas moved through the channel was calculated by an energy balance. The model predicted that a smaller channel gap and longer

channel length increased the heat transfer to the pot, but this was not experimentally validated. The model also made many assumptions, and the author cautioned against its use as a predictive tool. Agenbroad et al. [15,16] developed a Bernoulli equation based model with a constant loss coefficient to predict the flow rate through a rocket elbow without a pot, shown in Equation 1.1.

$$\dot{m}_A = \mathrm{CA}\left(\frac{P}{R_S}\right)\left(\frac{1}{T_H}\right)\sqrt{2gh\left(\frac{T_H - T_{amb}}{T_{amb}}\right)} \tag{1.1}$$

where C is the loss coefficient, A is the flow area, P is the pressure, T_H is the temperature of hot gas, and T_{amb} is the ambient temperature. The inputs to the model were the geometry of the elbow and the firepower. The firepower was used to calculate a temperature, which was used to calculate a pressure drop and hence, the flow rate. The walls were assumed to be adiabatic, and heat transfer and combustion were not modeled. The model was validated with excess air and temperature measurements for a range of firepowers.

CFD based models of cookstoves have also been developed [13,17–20]. While computationally more demanding, CFD based models can be applied to complex geometries, and can provide vital information about heat transfer, mixing and combustion processes within the cookstove. Burnham-Slipper [17] developed a two dimensional axisymmetric steady state Reynolds Averaged Navier Stokes (RANS) model coupled with a pyrolysis sub-model. The model considered the simple geometry of a cylinder as the riser with an aluminum plate on top to simulate the cooking surface. Combustion was modeled using a single step chemical mechanism. Heat transfer through conduction, convection and radiation was modeled, though radiation due to soot was neglected. The model was compared to temperature and heat transfer data from the rocket stove modeled. Six stove dimensions,

such as stove diameter, stove height, wall thickness and the distance between the plate and the stove body were assigned a low and high value in both experiment and simulation. The model predicted burn rates and temperatures inside the stove for some cases but not for others, such as when the stove diameter, stove height and distance between the plate and body were changed. The model was used to optimize an Eritrean wood-burning stove using a genetic algorithm, but results were not validated. Miller-Lionberg [20] developed a three dimensional transient LES model with combustion modeled by a mixture fraction method and soot predicted by the Moss-Brookes model, along with heat transfer to the environment through convection, conduction and radiation. Inputs to the model were a realistic geometry of an improved rocket stove and fuel flow rates based on both low and high firepower values. The model generated time resolved temperature and velocity data. Time-averaged results of heat transfer to the pot side and bottom, CO and PM emissions from the model were compared to experimental data. The model predicted the overall heat transfer to the pot accurately for high firepower, but the low firepower case had an error of 28.8%. However, the heat transfer to the bottom of the pot was overpredicted, and the heat transfer to the side of the pot was predicted to be negative in both cases. CO emissions were underpredicted by four orders of magnitude, and soot emissions were underpredicted by ten orders of magnitude. Since the model was computationally demanding, results from only two simulations were shown. Wohlgemuth et al. [18] studied the effect of the gap between the pot and pot skirt using a two dimensional axisymmetric RANS CFD model. Combustion was not modeled, and the velocity, temperature and turbulent intensity was specified when the gas exited the combustion chamber. The study suggested that an optimum distance for skirt placement exists and that insulating the pot skirt increases the efficiency of the stove. Bryden

et al. [19] used a graph-based genetic algorithm coupled with a three dimensional CFD model to spatially minimize the differences in temperature on the cooking surface of a 'plancha' stove by placing baffles in the flow. An extensive review of cookstove modeling is provided in MacCarty and Bryden [13], and the reader is directed to the publication for further information.

1.2.3 Mechanism of Soot Formation in Flames

Soot formation comprises of four major processes: particle inception or nucleation, surface reactions (including surface growth and oxidation), particle coagulation, and agglomeration [21]. The first step in soot growth is the formation of benzene rings from aliphatic hydrocarbons, followed by the formation of polycyclic aromatic hydrocarbons (PAHs). The forming of the first benzene ring is thought to be the rate limiting step in the sequence to larger aromatics. Several pathways from small hydrocarbons to the first aromatic ring have been proposed in the literature. These include the addition of acetylene to n-C_4H_3 and n-C_4H_5 to form the phenyl radical and benzene, respectively [22], the combination of propargyl radicals [23,24] to form benzene, and the reaction of the propargyl radical with acetylene to form cyclopentadienyl, which reacts rapidly to form benzene [25]. If the fuel has aromatic compounds as its constituents, larger PAHs can form from it, as was shown by Griesheimer and Homann who detected various biaryl compounds in a rich, premixed naphthalene flame [26]. Once formed, aromatics continue to grow mainly through a two-step repetitive reaction sequence consisting of the abstraction of a hydrogen atom from the aromatic species by another hydrogen atom in the gaseous phase, followed by the addition of an acetylene molecule. This reaction sequence has been termed HACA (H-

abstraction/C_2H_2-addition) [27], and is the most widely accepted growth mechanism for PAHs. Other mechanisms for PAH growth also exist, such as the addition of methyl (CH_3), vinyl (C_2H_3), propargyl (C_3H_3) and cyclopentadienyl (C_5H_5) radicals [25,27–31], instead of an acetylene molecule. Due to the relatively low concentration of these radicals in the post-flame zone of a real flame environment, however, these pathways have been observed to relax to HACA [21]. PAH addition reactions, where two PAHs combine to form a biaryl radical is another mechanism of PAH growth [26].

The process of soot nucleation, or transition from gaseous phase PAHs to solid phase soot is possibly the least understood process in soot formation [21]. Two mechanisms of soot nucleation are found in literature, chemical growth [32] and coagulation [22,27,33]. Chemical growth involves the accumulation of mass by a PAH molecule until the molecule crosses the threshold to becoming a particle. Growth by physical coagulation assumes that a new particle is formed when two PAHs collide and stick, hence forming a PAH dimer. Several numerical studies assume pyrene dimerization to be the nucleation step [34–36], though the role of pyrene in soot nucleation in flames has been debated [37,38].

Soot growth occurs mainly through three processes: chemical growth via C_2H_2 addition, condensation of PAHs on soot, and coagulation of soot particles. The first two result in an increase in total mass, while the third results in an increase in mean diameter without affecting the total mass. Growth via C_2H_2 addition is always observed to be significant irrespective of the fuel, and follows first order kinetics [21,39–41]. Soot oxidation in flames occurs mainly though the reaction of soot with O_2 and OH [42,43]. Commonly used models for predicting oxidation by O_2 are the expressions derived by Nagle and Strickland-Constable

[44] and Frenklach [33], while a temperature-independent reaction probability was determined in laminar premixed flames by Neoh et al. [45] for oxidation by the OH radical.

The reactivity of soot to radials such as the H radical is observed to decrease as the soot particle increases in size [21]. This phenomenon is referred to as thermal ageing or surface ageing in the literature. This is generally thought to occur due to the reduction in active sites as the size of the soot particle increases. Surface ageing has also been used to explain the reduction in oxidation rates in the post-flame region of laminar diffusion flames [46,47]. The effect of surface ageing is generally modeled by multiplying a factor, alpha, to the rate equations for soot growth and oxidation. Several expressions for alpha exist, including constants [33,48,49], functions depending on temperature and size [34,40,50,51], and expressions that take into account the thermal age of the particle [46,47]. A commonly used expression for calculating alpha based on the average size and temperature of soot particles is given by,

$$\alpha = \tanh\left(\frac{a}{\log\mu_1} + b\right) \tag{1.2}$$

where μ_1 is the first size moment of particle size distribution, and a and b are fitted parameters dependent on the temperature [34]. A more recent formulation of α for oxidation, dependent on the thermal age is given by [47],

$$\alpha_{ox} = \left(\frac{T_{a,max}}{T_a}\right)^2 \exp\left(2\left(1 - \frac{T_{a,max}}{T_a}\right)\right) \tag{1.3}$$

where T_a is the thermal age, defined as $\int T dt$, where T is the temperature of the soot particle, and t is the residence time. $T_{a,max}$ is the value of the thermal age at the point of maximum soot volume fraction.

1.2.4 Soot Emissions from Non-Premixed Flames

Predicting the mass and size distribution of soot emissions from both turbulent and laminar non-premixed flames remains a challenging problem. Experimental studies on non-premixed flames have focused mainly on characterizing in-flame soot volume fractions [52–60]. The importance of these studies for understanding soot formation and validating mathematical models is undeniable; however, the data from these investigations often do not extend into the overfire region where soot oxidation ceases. Therefore, they provide limited information about the rate of soot emissions from the flame. Relatively few studies have focused on investigating the rate of soot emissions from non-premixed flames. In addition, soot emission from a non-premixed flame impinging on a cold surface, to the best of the author's knowledge, has not been investigated before. This latter configuration has special relevance to the problem of understanding soot emissions from cookstoves.

Soot emission from turbulent non-premixed flames has previously been investigated. Becker and Liang [61] studied the emission of soot and thermal radiation from free non-premixed flames of CO, H_2, CH_4, C_2H_6, C_3H_8, C_2H_4 and C_2H_2, with fuel issuing out of round nozzles between 0.9 mm and 10.9 mm. Soot was measured by sampling the flow in the duct leaving the exhaust hood using a Millipore aerosol sampling filter. Thermal radiation was measured by a radiometer placed at some distance from the flame assuming a symmetric spherical radiation flux density. The flames studied ranged from momentum driven to nearly buoyancy driven. The results indicated that both the soot emission and radiation cooling increase with the buoyancy Richardson's ratio, Ri_L and tend to plateau as natural convection became dominant. Soot emission was also found to be strongly correlated with the second Damköhler ratio. In a follow-up paper [62], they explored the upper limits of soot emission

from non-premixed turbulent acetylene flames and found that the peak soot emission was $\sim 12\%$ of the mass of input fuel carbon at $Ri_{\mathrm{L}} = 600$. Kent and Bastin [63] investigated turbulent acetylene flames and showed that soot volume profiles scale with the flame time constant, defined as D/U_o, where D is the diameter of the jet and U_0 is the average jet exit velocity. Their study also suggested that soot burnout rates were strongly dependent on temperature, and that slow flames emit more smoke because the rapid temperature drop by radiation loss in the overfire region freezes burnout while the soot volume fraction is relatively high. Delichatsios [64] examined buoyant turbulent non-premixed flames burning gaseous, liquid and solid fuels and developed correlations for smoke yields based on these data.

Soot formation and emission in laminar non-premixed flames has also been investigated. Santoro et al. [65] examined the formation, growth, and burnout of soot particles in a series of co-annular ethylene laminar diffusion flames experimentally while varying the ethylene jet velocity and the annular airflow rate. They examined detailed temperature and velocity field measurements to investigate soot growth along individual particle trajectories and concluded that increased residence times were an important factor for the observed increase in soot formation in the flames studied. They further observed that the time-temperature history of soot particles appeared to be identical for all flames examined until the start of the oxidation process. Wright [66] examined the effect of oxygen premixing on soot emission in laminar ethylene, propane, and propylene diffusion flames, and found that soot emission increases until 11% of stoichiometric oxygen is premixed with the fuel, after which soot emission reduces drastically for all fuels. He hypothesized that the increase in soot emissions at low O_2 concentrations was due to increased polymerization of

carbon to higher molecular weight soot precursors, while further increases in O_2 premixing resulted in increased oxidation. Elzhey et al. [67] investigated the soot yield from a laminar propane diffusion flame in cross-flow, with the jet velocity and cross-flow velocity varied independently. They found that a flame in cross-flow produces more soot than the same flame in co-flow, and that increasing either the jet velocity or air velocity reduces the soot yield. Moss et al. [68] presented measured soot volume fraction data from an ethylene diffusion flame and developed a two-equation model to predict in-flame soot volume fractions. Smooke et al. [69] studied the effect of nitrogen dilution on laminar ethylene co-flow non-premixed flames experimentally and numerically, and found that the soot profiles obtained from laser-induced soot incandescence undergo a shift towards the wings of the flame as the ethylene fraction increases. Flower and Bowman [70] examined the effect of pressure on soot emission from laminar diffusion flames. The fuel used was ethylene and the pressure was varied from 0.1 MPa to 10 MPa. Soot emission was observed to increase as the pressure was increased, which was attributed to increased soot production and reduced soot oxidation.

Non-premixed flames impinging on cold surfaces have previously been investigated. The focus of these studies has been identifying the mechanism and characteristics of soot deposition onto the surface [71–74], characterizing heat transfer to the surface [75–78], or investigating emissions such as CO and NOx [78–80] from the system. Soot emission from a non-premixed flame impinging on a cold surface, to the best of the authors' knowledge, has not been investigated. This configuration, however, has special relevance to the problem of understanding soot emissions from cookstoves.

1.2.4 Mathematical Models of Soot Formation

The processes of nucleation, coagulation, surface growth/reduction and agglomeration result in a population comprising of different particle sizes. This can be mathematically modeled as a number density function (NDF), which is a probability density function (PDF) of the number of particles, with the mass/volume of the particles being the independent variable. Recent advances have modeled the NDF as a joint PDF, with the independent variables usually being the mass/volume and surface area of the particles. This approach allows the particle morphology to be treated mathematically as an independent variable. The evolution of the NDF is governed by the population balance equation (PBE) [81]. The PBE is usually rewritten and solved in one of three ways: Monte Carlo (MC) methods, sectional methods, and statistical methods which solve for moments of the NDF.

MC methods model the interaction of a large population of particles with each other and with the environment by stochastic processes, with each particle being tracked individually [82]. This class of methods gives the most accurate results, but requires a large amount of computational power, which often renders this method impractical for real-world applications (e.g., coupling with CFD codes). Hence, the MC method has mostly been used to model zero-dimensional reactors and laminar diffusion flames [36]. Several variables used to describe soot can, however, be tracked without an appreciable increase in computational power [83]. The MC method has been used to study soot precursor growth [84,85], and is often used to benchmark other soot models [86,87].

Sectional methods discretize the NDF into bins, and solve equations to model the evolution of particles in each bin [35,88,89]. These methods can accurately predict the soot NDF, but the number of bins increases exponentially with an increase in the independent

variables of the NDF [90]. Hence, they are almost exclusively used with single-variable NDFs, where the independent variable is usually particle volume. The definition of the bins themselves can be either fixed or evolving as the NDF evolves (referred to as moving sections). Fixed sectional models may lead to excessive numerical diffusion if a large enough number of sections is not used [35].

The method of moments solves for various moments of the soot NDF. While the NDF itself cannot be reproduced by this method, quantities such as average soot volume fraction, average particle size and total mass of soot produced can be predicted, since they can be derived from the moments of the NDF. The method of moments is computationally much less expensive than the sectional and MC methods, which has contributed to its wide usage. One of the issues with the method of moments is the need to close source terms since more moments are required to calculate source terms than are solved for. The method was first developed for a single-variable NDF, and closure was attained by using Lagrangian interpolation of the logarithms of the moments to find fractional moments (MOMIC) [33]. While widely used, this method was observed to deviate significantly from experimental measurements for bimodal NDFs. In contrast, the Quadrature Method of Moments (QMOM) gives excellent results for bimodal distributions. Closure in QMOM is achieved by approximating the NDF as a set of delta functions using Gaussian quadrature and calculating their abscissas and corresponding weights by the Product-Difference algorithm [91]. However, the extension of the QMOM method to multivariate distributions is mathematically complex and computationally demanding. Therefore, the Direct Quadrature Method of Moments (DQMOM) is used for bivariate distributions, in which a transport equation is solved to find the weights and abscissas of the delta functions [92]. The DQMOM can also be

easily extended to model multivariate distributions. Other method of moments include a bivariate extension to the original MOMIC [86], and the Hybrid Method of Moments, which combines MOMIC and DQMOM into a simpler framework, such that the bimodal NDF properties are captured [87].

1.3 Research Objectives and Document Organization

The literature review above indicates that previous models of cookstove behavior, while having significantly furthered the state of the art, have largely been validated and used for a limited number of often simple geometries, often with simplified physics. Combustion and soot formation are often not modeled, and heat transfer is often modeled without considering the presence of soot, which significantly affects the temperature distribution and heat transfer from the cookstove. The influence of design features that improve performance, such as custom shaping of the cone deck, secondary air entrainment ports, and baffles, on the stove performance has not been studied. The underlying physics behind why certain configurations result in better performance has not been well explained.

While in-flame soot formation in both turbulent and laminar non-premixed flames has been investigated numerous times, soot emissions from these flames have received significantly less attention. In addition, the mechanisms of soot formation in cookstoves have also not been investigated. One of the difficulties in studying soot formation in cookstoves is the significant chemical variability in the different kinds of available biomass and their combustion, as well as the inability of the investigator to directly control experimental parameters such as firepower. While a flame impinging on a cold surface has been shown to lead to increased soot emission when compared to a free flame [12] in cookstoves, this configuration has not been investigated before with respect to soot emission either

numerically or experimentally. A possible solution to this problem is the investigation of non-premixed flames impinging on a cold surface. This would capture the physics of soot emission from this configuration, while avoiding the inherent variability in experimentation with biomass flames. Parameters such as the heat release and the distance of the surface from the flame would be within the investigators control and their effect on soot emissions could be identified. This would serve as important information for stove designers and would guide the design of biomass-burning stoves.

The mathematical modeling of soot formation has received much attention in the last 30 years. Recent advances have shown promising results when predicting soot emissions from free non-premixed flames running on simple fuels. These models have not been applied to the study of non-premixed flames impinging on a cold surface, which could provide valuable insight into the soot formation mechanisms and the control of soot emission from this configuration.

The main objective of this study is to develop numerical models that can accurately capture the fluid flow, mixing and heat transfer in natural draft, wood burning cookstoves, and the experimental and numerical investigation of soot emission from a non-premixed turbulent flame striking a cold surface, a configuration closely related to the biomass-burning cookstove . These models should accurately predict quantities of interest such as the airflow rate, thermal efficiency and mass of soot emitted, in order to guide the design of biomass burning cookstove, as well as understand and improve their performance. Specific objectives include:

- Understanding the effect of operational and geometric parameters on performance parameters, such as the airflow rate through the cookstove, heat transfer to the

cookpot and mixing in the stove, in order to guide the design of energy efficient cookstoves.

- Develop an understanding of the soot formation behavior accompanying a turbulent flame striking a cold surface in order to guide the design of a cleaner burning cookstove.

CFD models are first developed without soot formation being taken into account in order to study mixing and heat transfer in cookstoves. These models are used to study the effects of design features such as secondary air entrainment, baffle placement and cone-deck shape on the airflow rate, mixing and energy efficiency of the rocket cookstove in order to guide the design of more energy efficient cookstoves. Turbulent ethylene flame impinging on a cold surface, a configuration closely related to the biomass-burning cookstove are considered. Soot mass emission and size distribution data obtained from experiment is analyzed and a CFD-based numerical model for soot formation for this configuration is developed.

The remainder of this thesis is divided into four chapters and three appendices. Chapter 2 presents the development of two CFD models for predicting heat transfer and fluid flow in cookstoves. These models are then used to predict the excess air, energy efficiency and other quantities of interest, along with the analysis of fluid flow for various cookstove configurations. The effect of changing geometric parameters on the airflow rate, mixing and thermal efficiency is also studied. Soot formation in turbulent ethylene flames impinging on a cold surface is investigated experimentally in Chapter 3. The development of a numerical model for predicting in-flame soot emissions and the total mass of soot emitted is presented in Chapter 4. The model is used to predict the total mass of soot emitted by a turbulent flame

impinging on a pot and analyze the pathways to soot formation for this configuration. Chapter 5 summarizes the results and conclusions of this work and concludes the dissertation. The possible impact of this work and directions for future research are also explored in this chapter.

Chapter 2 : Modeling Combustion and Heat Transfer in Cookstoves

2.1 Overview

This chapter presents the development of two CFD models for predicting combustion, fluid flow and heat transfer in cookstoves. The two models are a two dimensional axisymmetric steady-state model and a three-dimensional steady state model. The axisymmetric model is less computationally intensive and is used to study the effects of various geometric parameters, while the three-dimensional model, being computationally more intensive, is used to study fluid flow in specific geometries. The models are applied to the various configurations of a rocket cookstove, and results such as the flow field, temperature and species distributions, excess air and heat transfer efficiency are predicted for several configurations of the cookstove. The role played by several components of the cookstove with respect to the heat transfer efficiency, flame position and mixing within the cookstove is examined. Finally, the results of optimizing a cookstove part using the axisymmetric CFD model are presented.

2.2 Two-Dimensional Axisymmetric Model

2.2.1 Model Geometry

The computational domain is a simplified representation of a side-fed natural draft rocket stove, a schematic of which is shown in Figure 2.1. Air enters from the primary air inlet at the bottom of the stove and wood volatiles are discharged uniformly from three toroidal fuel inlets. The toroidal fuel inlets have approximately the same surface area as the nominal four sticks of wood used in the experimental work. The wood volatiles and air mix in the combustion chamber, which is a cylindrical cavity of 100 mm diameter and 291 mm height, giving rise to flaming combustion. The riser provides a flow path above the combustion chamber. Secondary air is entrained into the riser 150 mm above the primary air inlet. The hot combustion gases flow towards the 280 mm diameter pot that is placed above the riser atop a conical-shaped cone deck. The cone deck serves as a gradual area expansion for the gas flow, to prevent flow separation, and directs flow over the bottom of the pot and out to the 340 mm diameter pot skirt. A pot skirt is an optional stove feature that directs hot combustion gases along the sides of the pot and improves heat transfer to the pot [93].

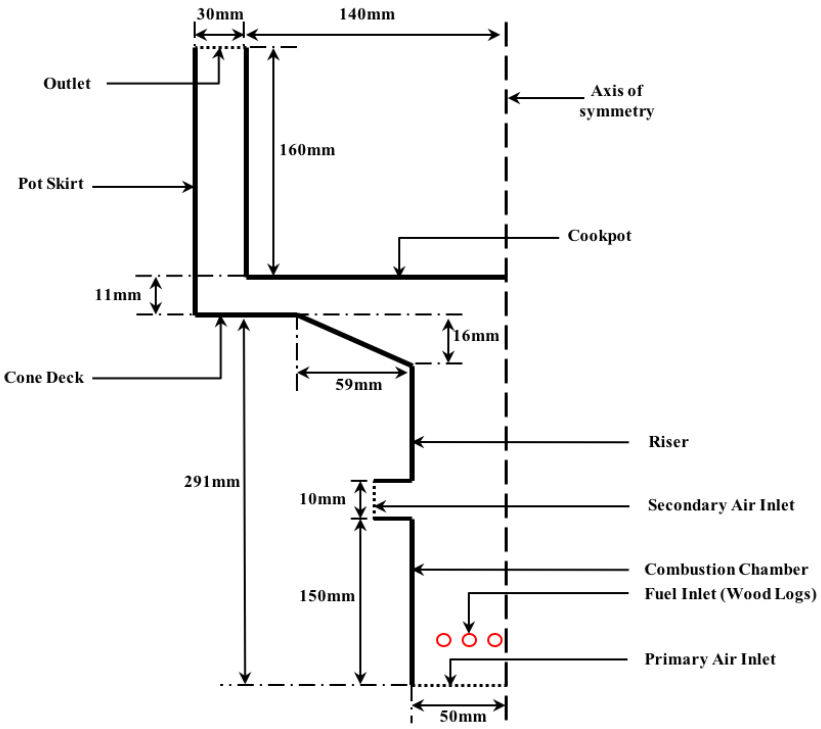

Figure 2.1: Schematic of axisymmetric computational domain. Air enters from the primary and secondary air inlets; fuel enters from the fuel inlet. The flow exits at the outlet.

2.2.2 Mathematical Model

The mathematical model consists of conservation equations for mass, momentum, energy, chemical species, and turbulence parameters. The Favre-averaged conservation equations of mass, momentum, energy, and species transport are solved. Turbulence is modeled by the Realizable $k-\varepsilon$ turbulence model, which is a modified form of the standard two-equation $k-\varepsilon$ model [94]. The model solves transport equations for turbulent kinetic energy, k, and the turbulent dissipation rate, ε [95]. The momentum equation is closed by calculating the turbulent eddy viscosity,

$$\mu_T = \rho C_\mu \frac{k^2}{\varepsilon} \tag{2.1}$$

from the turbulent kinetic energy k, the turbulent dissipation rate ε, the density ρ, and C_μ, a model parameter that is a function of the strain rate tensor, k, and ε [94]. The energy equation in closed by assuming a turbulent Prandtl number of 0.9 [95] .The specific heat at constant pressure of each species is assumed to vary as a polynomial function of temperature, while the specific heat of the mixture is a mass-weighted average of the specific heats of the individual species [96]. The laminar dynamic viscosity is computed using Sutherland's Law [97]. The molecular diffusivity of the mixture is calculated from the Schmidt number and the thermal conductivity from the Lewis number, assumed to be constant at 1.0 [98]. The turbulent Schmidt number is assumed to be constant at 0.9 [99]. Radiation is modeled by solving the radiative transfer equation (RTE) by the discrete ordinates method, using the S_4 approximation [98]. Soot is not explicitly modeled, with a uniform and constant absorption coefficient of the gas used as a surrogate instead, as was done by Wohlgemuth et al. [93]. Following Wohlgemuth, an increased absorption coefficient due to the presence of soot is accounted for by calibrating the model with experimentally measured temperature data. All surfaces are assumed to be black and the gas is assumed to be gray.

Combustion is modeled by the laminar finite rate model, in which reaction rates are determined by Arrhenius kinetic expressions [96]. This is appropriate given the laminar/transitional nature of the flow. The source term for each species transport equation is given by the Arrhenius expression for each reaction involving that species in the chemical kinetic mechanism. The 11-species, 21-step reaction mechanism proposed by Hawkes et al [100] is used. This is a combined CO/H_2 combustion skeletal mechanism which was created by reducing a full chemical kinetic mechanism proposed by Li et al. [101] by analyzing data

from laminar diffusion and premixed flames, homogeneous ignitions, and 2D unsteady jets. This mechanism is chosen because the predominant flammable components in the wood volatile composition considered are CO and H_2. The mechanism is shown in Table 2.1.

Reaction No.	Reaction	Pre-exponential factor, A	Temperature exponent, n	Activation Energy (cal mol^{-1})
1	$H + O_2 \Leftrightarrow O + OH$	3.547×10^{15}	-0.406	1.6599×10^4
2	$O + H_2 \Leftrightarrow H + OH$	5.08×10^4	2.67	6.24×10^3
3	$H_2 + OH \Leftrightarrow H_2O + H$	2.16×10^8	1.51	3.43×10^3
4	$O + H_2O \Leftrightarrow 2OH$	2.97×10^6	2.02	1.34×10^4
5	$H_2 + M \Leftrightarrow 2H + M$	4.577×10^{19}	-1.40	1.0438×10^5
6	$2O + M \Leftrightarrow O_2 + M$	6.165×10^{15}	-0.5	0.00
7	$O + H + M \Leftrightarrow OH + M$	4.714×10^{18}	-1.0	0.00
8	$H + OH + M \Leftrightarrow H_2O + M$	3.8×10^{22}	-2.0	0.00
9	$H + O_2 + M \Leftrightarrow HO_2 + M$	1.475×10^{12}	0.6	0.00
10	$HO_2 + H \Leftrightarrow H_2 + O_2$	1.66×10^{13}	0.0	8.23×10^2
11	$HO_2 + H \Leftrightarrow 2OH$	7.079×10^{13}	0.0	2.95×10^2
12	$HO_2 + O \Leftrightarrow O_2 + OH$	3.25×10^{13}	0.0	0.00
13	$HO_2 + OH \Leftrightarrow H_2O + O_2$	2.89×10^{13}	0.0	-4.97×10^2
14	$CO + O + M \Leftrightarrow CO_2 + M$	1.8×10^{10}	0.0	2.384×10^3
15	$CO + HO_2 \Leftrightarrow CO_2 + OH$	3.01×10^{13}	0.0	2.3×10^4
16	$CO + OH \Leftrightarrow CO_2 + H$	2.229×10^5	1.89	-1.158×10^3
17	$HCO + M \Leftrightarrow H + CO + M$	4.7485×10^{11}	0.659	1.4874×10^4
18	$HCO + O_2 \Leftrightarrow CO + HO_2$	7.58×10^{12}	0.0	4.1×10^2
19	$HCO + H \Leftrightarrow CO + H_2$	7.23×10^{13}	0.0	0.00
20	$CO + O_2 \Leftrightarrow CO_2 + O$	2.5×10^{12}	0.0	4.77×10^4
21	$HCO + O \Leftrightarrow CO_2 + H$	3.0×10^{12}	0.0	0.00

Table 2.1: Reaction mechanism for wood volatile combustion, taken from Hawkes, et al.

2.2.3 Boundary Conditions

The model requires boundary conditions for the inlets, outlet, and stove walls. The air at the inlet is entrained by natural convection and thus we specify atmospheric pressure and

temperature (300 K) and a turbulent intensity of 7.5%. Turbulent intensity values between 5% and 10% were considered, but no significant difference was found for these values. The fuel inlet is specified as a mass flow rate with the flux of volatiles set by the desired burn rate of 2 to 5 kW, which is consistent with burn rates in cookstove modeling literature, as well as observed in the lab and field[8,15,20]. The flux rate of volatiles entering the computational domain is set to match the desired burn rate. We do not model the conversion of solid fuel to volatiles, and the model does not provide a feedback mechanism from the flame to the fuel devolatilization process. A simplified composition of wood volatiles is taken from Galgano et al. [102] with minor modifications, shown in Table 2.2. The original composition contains $\sim 6\%$ CH_4, which we have converted to an equivalent amount of hydrogen on a heating value basis. This has a negligible effect on the heat release but has the advantage of drastically reducing the size of the chemical kinetic mechanism since accurate modeling of CH_4 combustion requires roughly 50 species. The presence of tar has also been neglected.

Species	CO	CO_2	H_2	H_2O
Mass Fraction	0.383	0.273	0.032	0.312

Table 2.2: Mass fraction of species in wood volatile mix

The boundary condition at the outlet of the pot skirt is specified as atmospheric pressure. The cookpot is isothermal at the boiling point of water at atmospheric pressure (373 K). The combustion chamber, riser, cone deck, and pot skirt are modeled using a mixed convection, conduction, and radiation boundary condition. By this procedure, a heat transfer coefficient for each of the boundaries mentioned above is calculated. This combined heat transfer coefficient includes the effect of the wall thickness, insulation thickness and

convection and radiation from the outer body to the environment. The external heat transfer coefficients are calculated using standard heat transfer correlations [103].

The axisymmetric simulations are carried out using the STAR-CCM+ commercial software package using the finite volume method [104]. An unstructured polyhedral mesh selected after grid independence studies is used. Prism layers are added near the walls to adequately resolve the boundary layer in order to eliminate the need of wall functions in the turbulence model and accurately predict the heat transfer to the walls and the pot.

2.2.4 Model Assumptions and Limitations

In this work, it is assumed that the flow is statistically steady, and that a cylindrical symmetry exists, such that the 3D geometry can be treated as an axisymmetric 2D geometry. A uniform absorption coefficient of gas inside the domain is also assumed. Due to these assumptions, some non-axisymmetric geometric aspects of a side-fed stove are impossible to model accurately, such as the front entrance for the wood sticks and air, and the presence of a fuel grate. The presence of the grate is not considered, and a simplified geometry is used upstream of the combustion chamber, which includes air entrainment from the primary air inlet at the bottom of the stove, and wood volatiles discharged uniformly from three toroidal fuel inlets. Due to the steady-state nature of the model, transient phenomena, such as the difference in flaming and char combustion at different times during the experiment and the changing water temperature, cannot be captured by the model. The advantage of the simplicity of the model is that it can be carried out with relatively modest computational resources and can accurately predict air flow characteristics and thermal efficiency as a function of stove geometry.

2.3 Three-Dimensional Model

2.3.1 Model Geometry

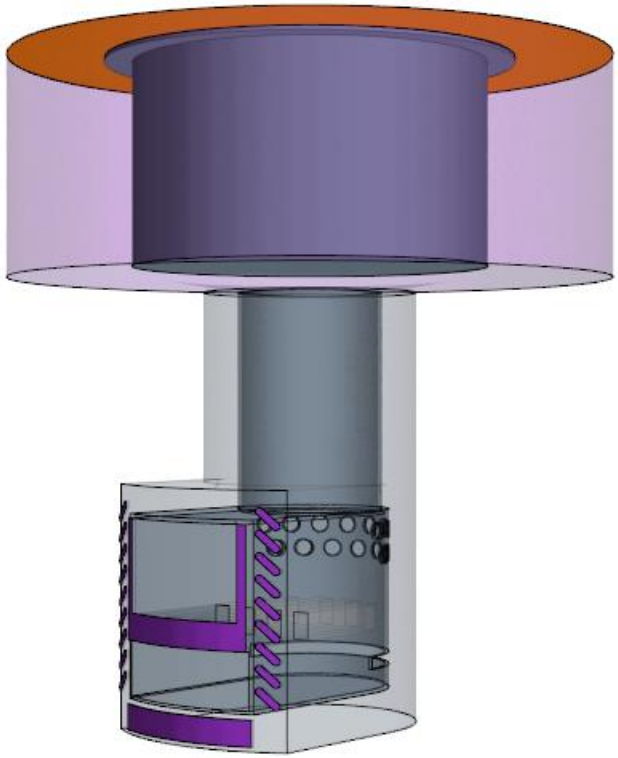

Figure 2.2: Schematic of three-dimensional computational model. Air enters from the surfaces shown in purple. The fuel volatiles enter from the surfaces shown in light brown. Flow exits from the orange surface.

Figure 2.2 shows a representative schematic of the computational domain. Air enters from the surface shown in purple. Fuel enters from the light brown surfaces inside the domain, shaped like wood sticks. Secondary air is entrained into the combustion chamber through a set of holes at the front of the combustion chamber, as well as a rectangular aperture at the bottom of the combustion chamber. The sheet of metal separating the primary and secondary flow paths is modeled as a 1 mm thick sheet of stainless steel. The

flow travels upwards due to buoyancy and exits from the surface shown in orange in Figure 2.2.

2.3.2 Mathematical Model

Fluid flow, turbulence, energy, radiation and properties of the fluid are modeled as detailed in Section 2.2.2, with the corresponding three-dimensional equations instead of the two-dimensional cylindrical equations used therein. Combustion is modeled by the hybrid Eddy Breakup Model [105], which assumes that the reaction rate is controlled by turbulent mixing or chemical kinetics, whichever rate is lower. A simple four-step reaction mechanism by Galgano et al. [106] is chosen. The mechanism is used to describe all reactions through the combustion and post-combustion zone and is shown in Table 2.3. Wood volatiles are approximated as a mixture of CO, CO_2, H_2, H_2O and CH_4 [102]. The mass fractions of each species in the mixture are given in Table 2.3.

No.	Reaction Mechanism	Pre-exponential factor, A	Activation Energy, Ea (kJ/mol)
S1	$CO + \frac{1}{2}O_2 \rightarrow CO_2$	$3.98 \times 10^{17} (m^3/mol)^{0.75}/s\ K$	166
S2	$H_2 + \frac{1}{2}O_2 \rightarrow H_2O$	$10^{11} m^3/s\ mol$	42
S3	$CH_4 + 2O_2 \rightarrow CO_2 + 2H_2O$	$9.2 \times 10^{6} (m^3/mol)^{0.5}/s\ K$	80
S4	$CO + H_2O \Leftrightarrow CO_2 + H_2$	$2.78\ m^3/s\ mol$	65.8

Table 2.2: Four step chemical kinetic mechanism for wood volatile combustion.

Species	CO	CO_2	H_2	H_2O	CH_4
Mass fraction	0.383	0.237	0.006	0.312	0.062

Table 2.3: Mass fractions of species in wood volatile mix.

2.3.3 Boundary Conditions

The model includes realistic boundary conditions, including radiation from the gas and the walls, as well as heat loss from the sides of the cookstove and heat delivered to the cookpot. To simulate the presence of soot, the absorption coefficient of the gas is adjusted, which is assumed to be constant throughout the domain, as is described in Section 2.2.2. Since the domain contains the metal sheet between the secondary and primary flow path, we require a separate mesh and physics continuum for it. It is treated as a metal sheet made of stainless steel of constant density. Heat transfer between the fluid domain and metal sheet through conduction, convection and radiation, as well as heat conduction within the metal sheet is also modeled.

2.3.4 Model Assumptions and Limitations

Like in the two-dimensional axisymmetric model, it is assumed that the flow is statistically steady. A uniform absorption coefficient of gas inside the domain is also assumed. Due to the steady-state nature of the model, transient phenomena, such as the difference in flaming and char combustion at different times during the experiment and the changing water temperature, cannot be captured by the model. Detailed combustion is not included in this model; instead, a global chemical mechanism (shown in Table 2.2) with the Eddy Breakup Model is used for modeling combustion. The advantage of the simplicity of the model is that it can be carried out with relatively modest computational resources and can

accurately predict air flow characteristics and thermal efficiency as a function of stove geometry.

2.4 Experimental Methods

Experiments are conducted with a prototype wood stick side-fed, natural draft, rocket stove shown in Figure 2.3. Engineering drawings of the stove are given in Appendix A. The stove is 33 cm tall and 28 cm in diameter, with an 11 cm x 12 cm rectangular tunnel on one side for fueling. The feed tunnel extends towards the central vertical riser, which directs the hot combustion gases up towards the pot. The stove is equipped with a pot skirt, which keeps the hot gases in contact with the side of the pot. The fuel used is Douglas fir wood with an average moisture content of 9.2%. The results of proximate and ultimate analyses of the wood performed according to the ASTM E870 standard are provided in Table 2. Wood sticks of approximate cross-section 20 mm x 20 mm are used. This is typically different from in-field use of biomass stoves, where biomass of several different sizes is burned.

Proximate Analysis (% mass)	Ash		Volatile Matter		Fixed Carbon
	0.11		85.11		14.78
Ultimate Analysis (% mass)	C	H	N	O	S
	50.62	5.92	0.09	43.21	0.05

Table 2.4: Proximate (dry basis) and ultimate analysis (dry, ash-free basis) of Douglas Fir wood.

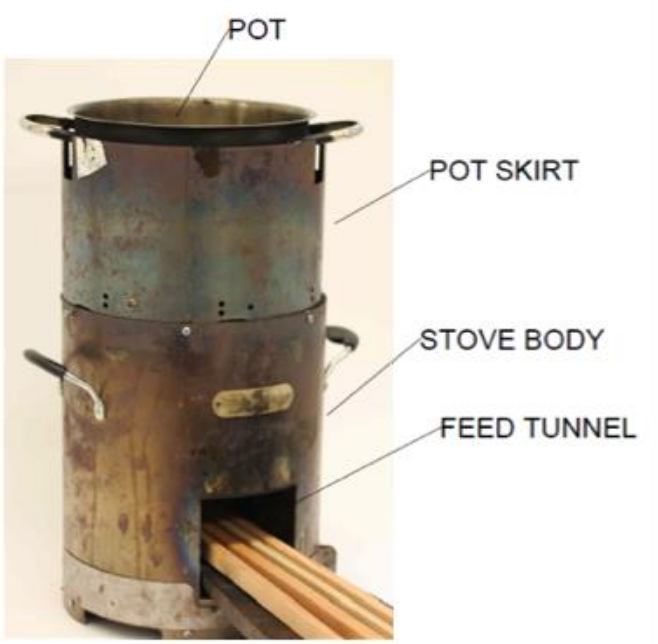

Figure 2.3: Wood side fed, natural draft rocket stove used for experimental validation. The pot skirt sits on top of the stove body to keep the combustion gases in contact with the pot.

2.4.1 Excess Air Measurement

Excess air flowing through the cookstove is calculated using measured CO_2 exit concentrations. If it is assumed that the fuel nitrogen content is negligible and that the fuel undergoes complete combustion (experiments show that the concentration of CO is less than 2% the concentration of CO_2), the excess air can be determined by rearranging the balanced combustion equation to give us the excess air as a function of CO_2 concentration.

$$C_xH_yO_z + \phi\left(x + \frac{y}{4} - \frac{z}{2}\right)(O_2 + 3.76N_2) \rightarrow xCO_2 + \frac{y}{2}H_2O + 3.76\phi\left(x + \frac{y}{4} - \frac{z}{2}\right)N_2 + (\phi - 1)(x + \frac{y}{4} - \frac{z}{2})O_2 \quad (2.3)$$

where x, y and z are kmoles of carbon, hydrogen and oxygen per 100 g of wood, calculated from the ultimate analysis of the fuel shown in Table 2.4. The measured CO_2 concentration y_{CO_2} can be written as the moles of CO_2 divided by the total moles of the products on the right

hand side of the balanced reaction equation, which can then be rearranged to give us the air fuel ratio ϕ, or excess air,

$$\text{Excess Air } = (\phi - 1) = \left(\frac{\frac{x}{y_{CO_2}} - x - \frac{y}{2} + \left(x + \frac{y}{4} - \frac{z}{2}\right)}{4.76\left(x + \frac{y}{4} - \frac{z}{2}\right)} - 1 \right) \tag{2.4}$$

During a test the stove is initially run on 4 sticks of wood as show in Figure 2.4 (A). Five liters of water is boiled from room temperature and then kept simmering within 5 °C of the local boiling temperature. We vary firepower between 1.5 kW and 5 kW during the simmer phase by controlling the amount of wood introduced into the cookstove. We use short tending intervals of 30 s to 60 s to maintain a constant firepower. As a result, there is minimal char buildup and the dominant model of heat release is flaming combustion. We use time averaged CO_2 concentration data during the simmer phase, where the measured CO_2 remains relatively constant, denoting constant firepower. The firepower is calculated by the mass rate of wood consumed multiplied by the heating value of the wood to give an energy produced per unit time.

Figure 2.4 (A) shows that the combustion gases are sampled from the top of the pot skirt in four representative locations (front, right side, left side, back) in an effort to obtain an average value. The gas is sampled using a four-pronged rake made from 4.76 mm OD stainless steel tubing. The stainless steel tubing is connected to 6.35 mm OD PVC tubing and converges into a single sample line. The flow is drawn by a bellows pump (MB-158, Senior Aerospace Metal Bellows, Sharon, MA), which feeds the sample flow to a CO_2 analyzer (PIR-2000, Horiba, Kyoto, Japan). The real-time mass of the cookstove is measured using a digital scale (ABK 70a, Adam Equipment, Danbury, CT).

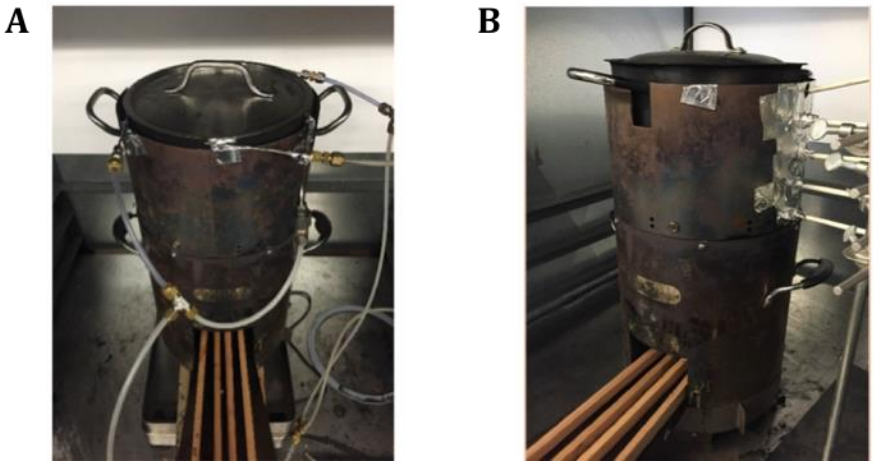

Figure 2.4: Experimental setup for measuring excess air through the cookstove and the temperature profile in the gap between the pot skirt and pot. (A) Four stainless steel probes sample the stove exhaust gases at the top of the pot skirt. These sample lines are combined into a single sample line that is routed to a CO_2 analyzer. (B) Five K type thermocouples are used to measure the gas temperature at distances of 1.5, 5.5, 10, 14 and 17 cm from the bottom of the pot skirt.

2.4.2 Temperature Measurements for Model Calibration

Gas temperatures are measured in the gap between the pot and the pot skirt for calibrating the model to account for the presence of soot. The gas is sampled at 1.5, 5.5, 10, 14, and 17 cm from the bottom of the pot skirt in a vertical line, as shown in Figure 2.4(B). Type-K thermocouples (3859K44, McMaster-Carr, Elmhurst, IL) are used and thermally isolated from the skirt using fiberglass insulation wrapped around the probes (while keeping the junctions exposed) to prevent contact with the pot skirt. Tests are performed with the thermocouples located at the front, sides, and back of the cookstove, with the location varied by rotating the pot skirt and thermocouples. The tests are run in a very similar manner to the excess air tests, but with the firepower maintained as close to 4 kW as possible. The measured temperatures are averaged over short time periods where the average firepower is close to 4 kW.

Since the soot volume fraction is not directly modeled, the radiation heat transfer due to soot is accounted for by employing an artificially high value of the gas absorption coefficient [93]. In this approach, the model is calibrated by adjusting the spatially uniform mean absorption coefficient (κ) in order to match experimentally measured temperature profiles in the cookstove as will be described in the results. The mean absorption coefficient for a luminous flame is given by $\kappa = 3.6\, cT_m/c_2$, where κ is the mean absorption coefficient in m^{-1}, T_m is the temperature in Kelvin, c_2 is the second constant of radiation, equal to $1.4388 \times 10^{-2}\ mK$ [107]. The constant c is defined as,

$$c = 36\pi f_v \frac{n^2 k}{[n^2 - (nk)^2 + 2]^2 + 4n^2k^2} \tag{2.5}$$

where n and k are the refractive and absorptive indices of refraction of the soot particles, respectively, and f_v is the soot volume fraction. Using values of n, k and f_v representative of hydrocarbon flames, Wohlgemuth et al. calculated the range of values the absorption coefficient can take to be between 0.03 m^{-1} and 11 m^{-1} [93]. The spatially averaged absorption coefficient should lie within this range of values. In real flames the absorption coefficient varies spatially and depends on the temperature and soot volume fraction.

2.5 Results and Discussion

This section contains results from experiments as well computational results from the models described in Sections 2.2 and 2.3. The measured temperature profiles are first compared with predicted temperature profiles generated by the axisymmetric model to calibrate the absorption coefficient, which is then used for subsequent calculations. All results presented are obtained from the axisymmetric model, except for the analyses of fluid

flow for specific geometries presented in Section 2.5.4, which are obtained from the three-dimensional model.

2.5.1 Calibration of Absorption Coefficient, κ

The spatially averaged absorption coefficient is first calibrated by using average measured temperature data. Figure 2.5 shows the gas temperature profile in the gap between the pot and the pot skirt as a function of height in the pot skirt (z = 0 is the bottom of the pot) (data shown are the average of the front, back, and side positions). The experimental data show that the temperature decreases with height in the riser as heat is transferred from the hot gases to the pot and the environment. The variation in measured temperatures around the circumference (shown by the error bars) is due to air from the inlet directing the flame towards the back of the riser, leading to a higher gas temperature in the back compared to the front; the CFD simulation is axisymmetric and does not capture this variation. The average measured temperature at each cross-section is used for the calibration procedure. The model is calibrated by varying the value of the gas absorption coefficient until the model temperature profile matches the experimental one, as shown in Figure 2.5. An absorption coefficient of 7.5 m^{-1} is found to best match the experimental data. If the absorption coefficient is calculated due to the presence of combustion gases only, the temperature profile shown in Figure 2.5 increases by approximately 200 K.

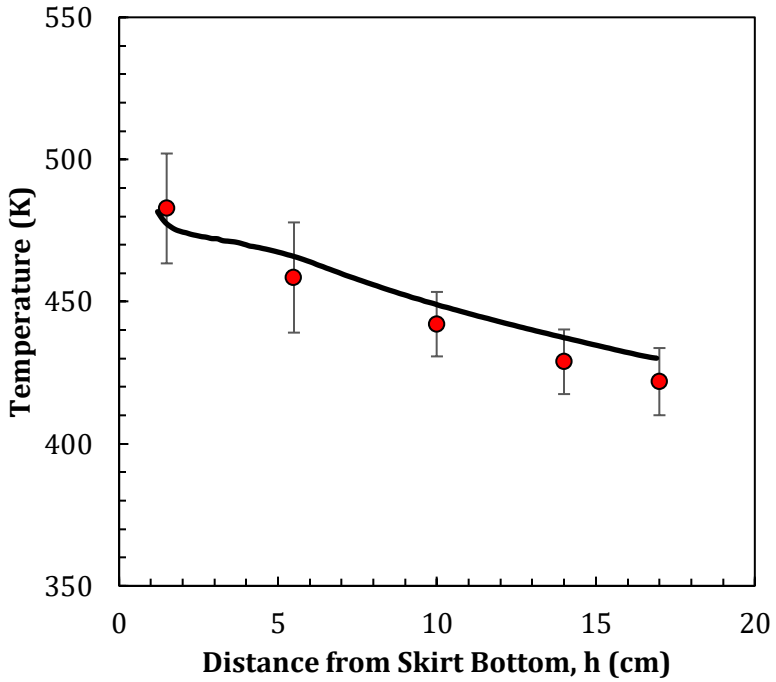

Figure 2.5: Comparison of measured temperature profile (symbols) with calibrated temperature profile (line) in the gap between the pot and pot skirt.

2.5.2 Relationship Between Firepower, Airflow Rate, and Excess Air

The axisymmetric model is used to examine the relationship between firepower and airflow rate. Figure 2.6(A) shows a plot of the computed total, primary, and secondary air mass flow rates, as well as the experimentally measured total mass flow rate as a function of firepower. The total mass flow rate remains nearly constant with firepower, as observed in both measurement and computation. This is due to the competing effects of decreasing density and increasing volumetric flow rates due to increased gas temperatures. Increased fuel consumption results in higher gas temperatures inside the combustion chamber, which results in a greater buoyant force. The increased buoyant force leads to a greater velocity of the gas, and hence, an increased volumetric flow rate. However, the increased temperature also results in lower density, which leads to a relatively constant mass flow rate despite the

increased volumetric flow rate over a wide range of firepowers. This effect of having a relatively constant mass flow rate over this range of firepowers is also observed in the predictions made by Agenbroad et al.[15], for which they provide a similar reasoning. Figure 2.6(A) also shows that the primary and secondary air flow rates stay fairly constant with increasing firepower. Figure 2.6(B) shows a plot of the excess air through the stove as a function of firepower for the CFD model and experiments. A constant air mass flow rate results in a lower excess air with increasing firepower, since more fuel is being injected with no change in airflow. At a low firepower of 2 kW, the amount of air present in the system is in excess of ten times what is required for complete combustion. At the highest fire power examined (5 kW), the excess air is still more than three times greater than what is required. Some excess air is recommended to enhance mixing and avoid rich combustion that could result in unwanted soot production [108]. Conversely, too much cool air flowing through the stove cools the combustion gases and can diminish heat transfer to the pot and degrade the thermal efficiency, as was also hypothesized by Baldwin [14].

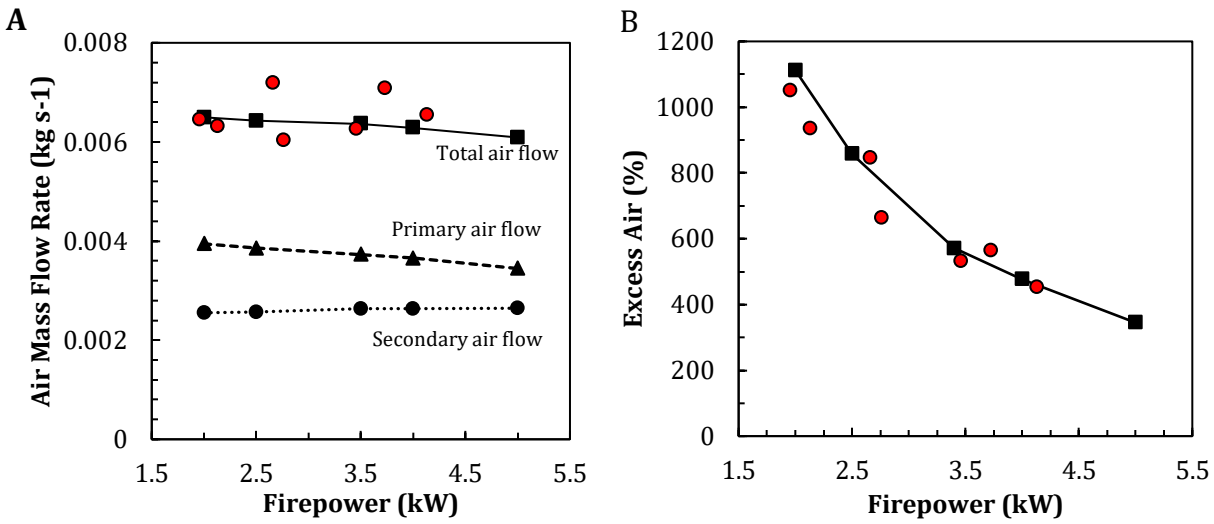

Figure 2.6: Plots of airflow rate (A) and excess air (B) as a function of firepower. (A) The circular red markers are experimental results. The square, triangular, and circular black markers are the total, primary and secondary air mass flow rates predicted by the CFD model, respectively. (B) The circular markers are experimental results and the square markers are results obtained from the CFD model.

2.5.3 Effect of Baffles and Secondary Air Entrainment

A method of reducing the excess air in a cookstove (and thus increasing thermal efficiency) is the placement of a central baffle in the riser. The baffle will (1) reduce air flow via introducing an additional pressure drop, and (2) potentially enhance mixing by creating a more complex flow field. The effect of baffle size on the airflow rate, thermal efficiency and mixing is examined in this section. The OH mass fraction, temperature distribution and the turbulent kinetic energy inside a cookstove with secondary air and with and without a central baffle are shown in Figure 2.7. Figures 2.7(A) and 2.7(B) show the computed OH mass fraction and temperature distribution inside the cookstove with secondary air injection. The OH radical is highly reactive and short-lived, and hence can be used to track the position of the flame front [96]. The flame is a diffusion flame and can be seen as a thin sheet of high OH concentration that sits at the stoichiometric air/fuel interface in Figure 2.7(A). Note that the flame front denoted by high OH concentration is also the hottest part of

the flame. Figure 2.7(B) shows the temperature distribution in the stove which varies from 1800 K in the flame front to 300 K at the air inlet. A zone of cold air is seen around the flame, which does not contribute to the combustion, but mixes with the burned gases further downstream and reduces the bulk gas temperature, which leads to a reduction in heat transfer to the pot. The cold air entering from the secondary air inlet does not penetrate the main flow and moves up along the riser wall. The turbulent kinetic energy distribution with secondary air, shown in Figure 2.7(C) shows very little turbulence in the region within the flame sheet. This is evidence that in this case the secondary air does not significantly contribute to mixing inside the stove.

Figures 2.7(D), (E) and (F) show the OH mass fraction, temperature distribution, and turbulent kinetic energy distribution inside the cookstove with secondary air and a central baffle blocking 45% of the riser area. When we add the baffle to the stove the temperature distribution is more uniform in the region above the riser and the turbulent kinetic energy is greater, suggesting enhanced mixing in the upper part of the riser. The presence of the baffle causes the flame to break up, as seen in the temperature distribution and OH mass fraction plots. The presence of the baffle also results in a reduction in the primary airflow rate, from 0.0034 kg g^{-1} to 0.0025 kg s^{-1} due to the flow obstruction caused by the baffle. The secondary airflow rate remains approximately the same when the baffle is present. Together, the baffle and secondary air flow results in better mixing downstream of the baffle, as is seen from the more uniform temperature distribution and greater turbulent energy. Higher temperatures and increased turbulent mixing have been linked to lower PM emissions in cookstoves [109].

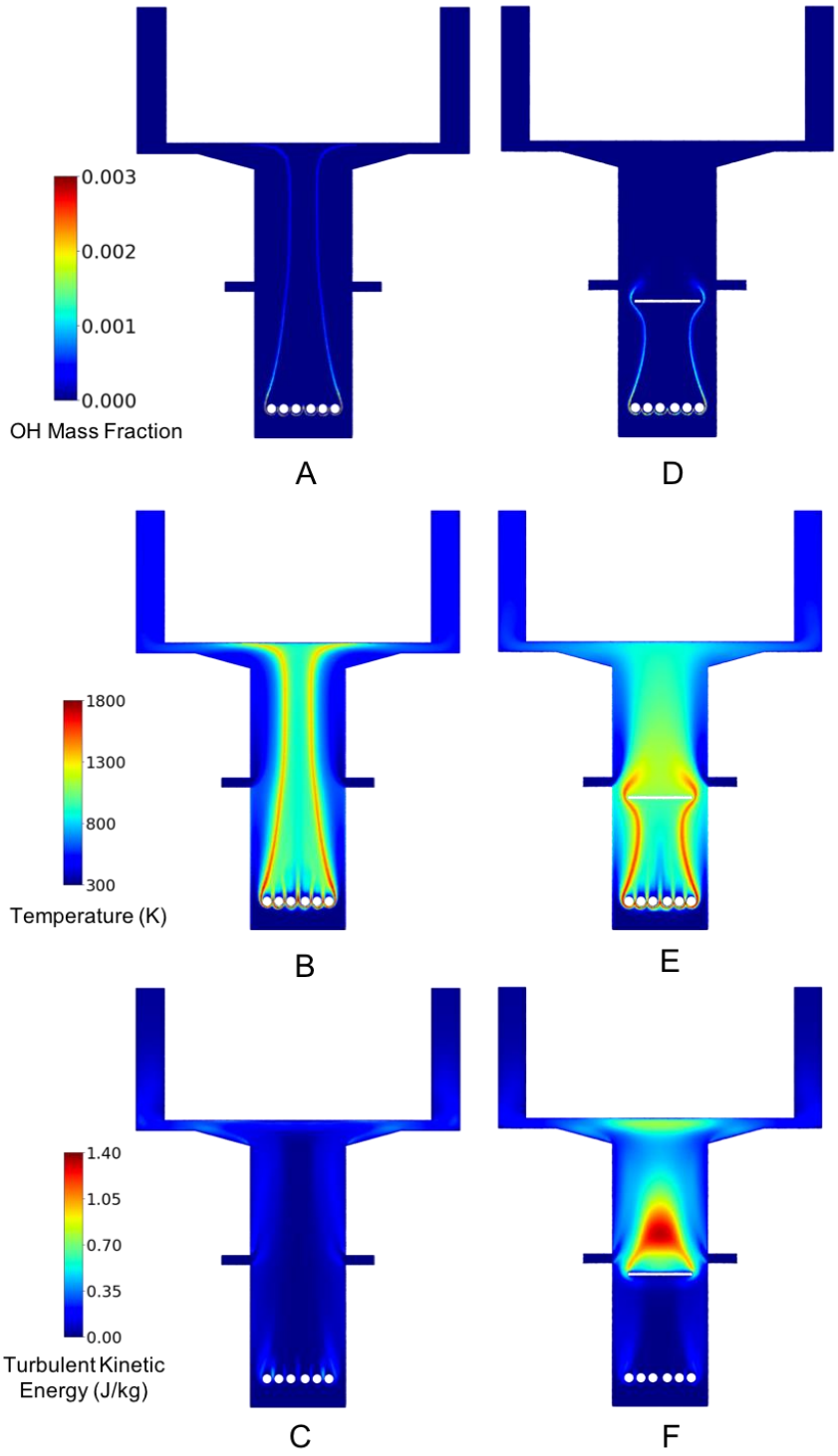

Figure 2.7: Effect of secondary air entrainment with and without baffle placement. (A) Computed OH mass fraction with secondary air. (B) Computed OH mass fraction with secondary air and central baffle blocking 45% of riser area. (C) Computed temperature distribution with secondary air. (D) Computed temperature distribution with secondary air and central baffle blocking 45% of riser area. (E) Computed turbulent kinetic energy with secondary air. (F) Computed turbulent kinetic energy with secondary air and central baffle blocking 45% of riser area.

Figure 2.8(A) shows plots of predicted primary, secondary and total air mass flow rates as a function of the percentage of riser area blocked by the central baffle, at a constant firepower of 4 kW. When no baffle is present, the airflow rate is nearly evenly divided between the primary and secondary air. The primary air flow rate decreases with increasing baffle size, since the baffle obstructs the primary air. At 75% riser area blockage, only 25% of the total airflow is contributed by the primary air. Figure 2.8(B) shows the effect of increasing baffle size on the stove efficiency as predicted by the axisymmetric model. The stove efficiency reduces slightly as the baffle size is increased. When flow is blocked by a central baffle, the reduced airflow rate leads to higher bulk temperatures, and more heat is absorbed by the riser walls and cone deck due to better mixing. Therefore, despite a reduction in the airflow rate, thermal efficiency is reduced.

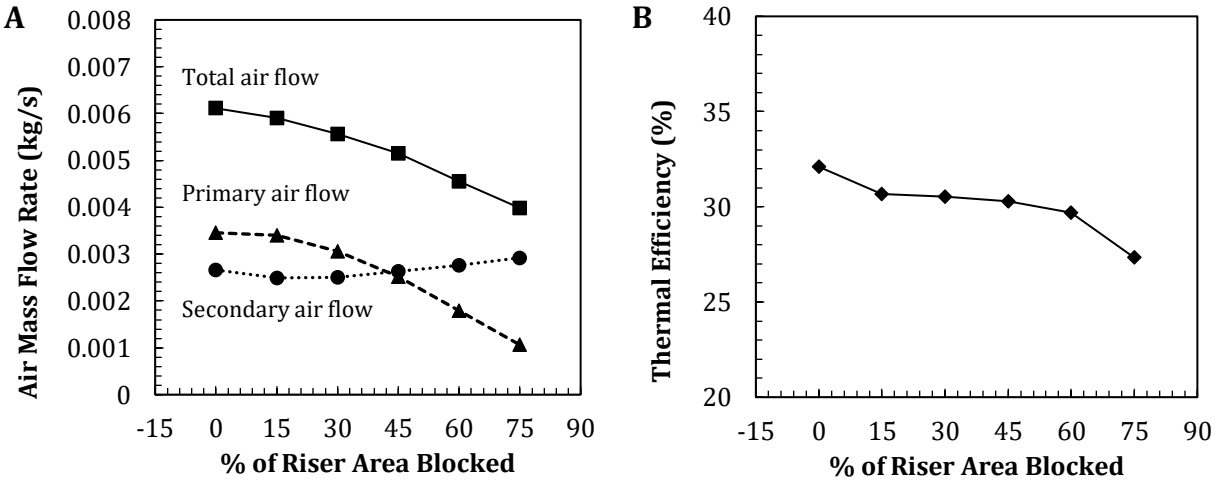

Figure 2.8: Predicted air mass flow rates and thermal efficiencies as a function of % riser area blocked by central baffle. (A) Primary (dashed line, triangular), secondary (dotted line, circular), and total (solid line, square) airflow rate as a function of riser area blocked by central baffle predicted by the model. The total airflow reduces as the size of the baffle is increased. The contribution of primary air reduces, and that of secondary air increases with increasing baffle size. (B) Stove efficiency predicted by the model as a function of riser area blocked by central baffle. The efficiency decreases slightly as baffle size increases.

2.5.4 Effect of Cone-Deck Shape and Pot Support Height

The cone-deck is the part of the cookstove placed on top of the riser. It serves as a gradual area expansion for the gas flow, which mitigates the effects of flow separation and directs flow under the bottom of the pot. A sample cone deck and its placement on a cookstove is shown in Figure 2.9(A) and (B).

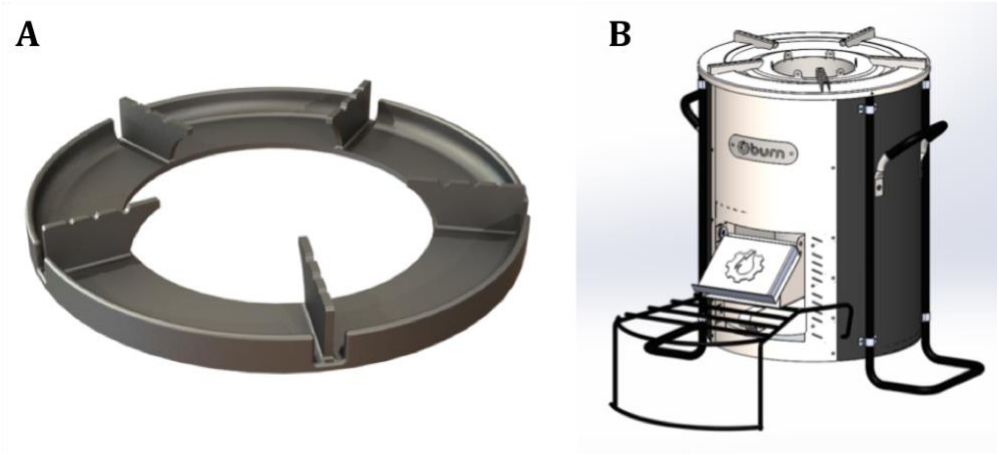

Figure 2.9: (A) Example of a cone-deck. (B) Position of the cone-deck on a cookstove (courtesy of Burn Design Lab).

An often quoted rule-of-thumb states that for optimal heat transfer to the pot, the cross-sectional area of the flow path throughout the cookstove should be constant, including the flow area over the cone deck [110,111]. To examine the robustness of this guideline, results are presented on how the shape of the cone deck influences performance parameters such as thermal efficiency and airflow rate. The shape of the cone deck is defined using three geometric parameters, shown in Figure 2.10: the horizontal distance from the centerline to the far end of the slanted region, *X*, the vertical distance between the top and bottom of the slanted region, *Y*, and the height of the pot supports. A total of 36 cone decks are modeled, with *X* values of 79 mm, 108 mm, 138 mm and 168 mm, *Y* values of 8 mm, 16 mm, and 24 mm

and pot support height values of 7 mm, 9 mm, and 11 mm. Each possible combination of *X*, *Y* and the pot support height is modeled for a constant firepower of 4 kW.

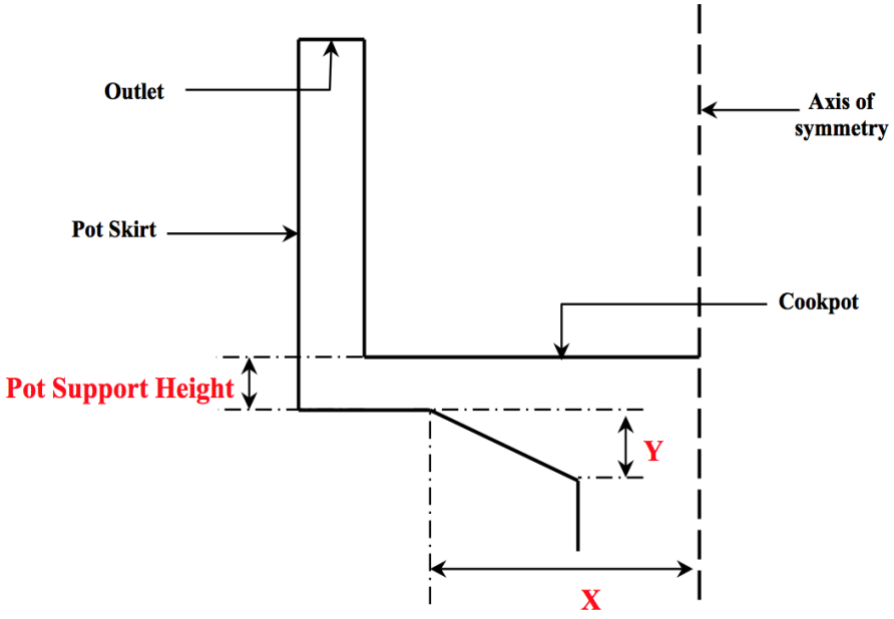

Figure 2.10: Geometric parameters defining cone deck shape.

Figure 2.11 shows a subset of the results of this study. Figure 2.11(A) shows the thermal efficiency as a function of X while Figure 2.11(B) shows the thermal efficiency as a function of pot support height. Each curve represents a constant Y. The thermal efficiency reduces as X increases, and for a constant X, reduces as Y increases. The difference in efficiency between a Y of 8 mm and 16 mm is much greater than the difference between a Y of 16 mm and 24 mm, provided that the firepower can be held relatively constant. Therefore, the plot suggests that a 'flatter' cone deck (low Y) is better than a 'steeper' design (high Y). Figure 2.11(B) shows that reducing the pot support height increases the thermal efficiency irrespective of Y. This corresponds to a reduction in airflow rate (shown in Appendix A).

Based on this analysis (complete results shown in Appendix A), three cone deck configurations are fabricated and tested. The configurations are as follows:

- Configuration 1: X = 108 mm, Y = 20 mm, Pot support height = 11 mm
- Configuration 2: X = 108 mm, Y = 10 mm, Pot support height = 11 mm
- Configuration 3: X = 108 mm, Y = 10 mm, Pot support height = 9 mm

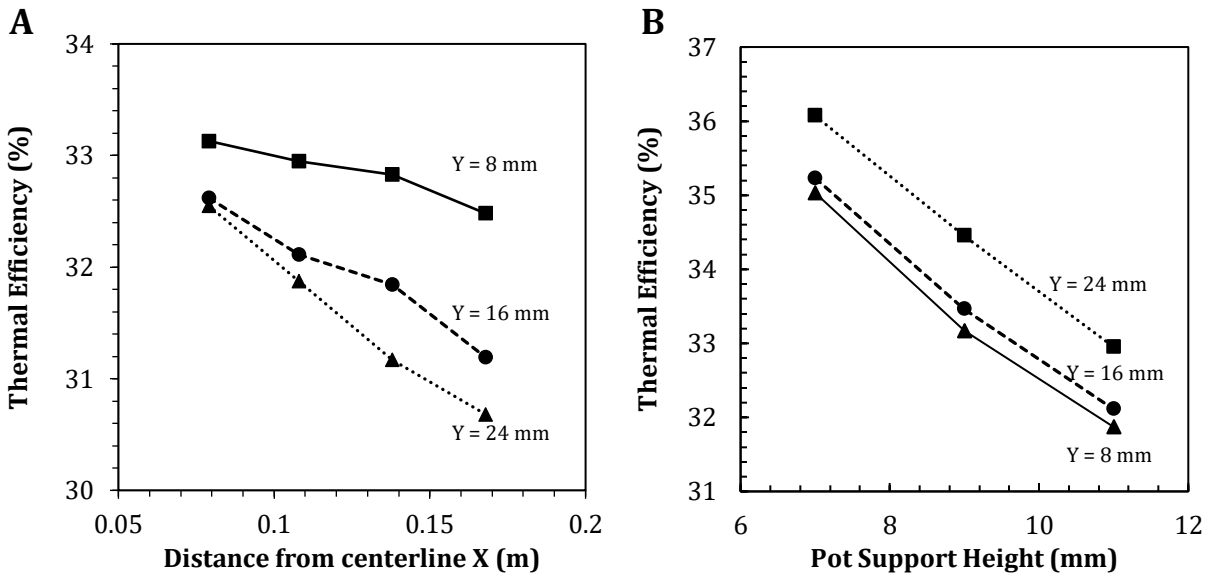

Figure 2.11: Thermal efficiency as a function of cone-deck shape geometry. (a) Thermal efficiency as a function of X for a pot support height of 11 mm. The solid curve is for a Y of 8 mm, the dashed curve is for a Y of 16 mm, and the dotted curve is for a Y of 24 mm. (b) Thermal efficiency as a function of pot support height for a constant X of 108 mm. Each curve represents the same Y as (a). All curves are for a constant firepower of 4 kW.

Configuration 1 is the baseline configuration before the study was conducted. The X value is not changed since it is fixed by the manufacturing process. For Configuration 2, the Y value is dropped, since an increase in thermal efficiency was expected. In Configuration 3, the pot support height is dropped to 9 mm in order to further increase thermal efficiency. The cone decks were tested at an average firepower of 3.5 kW. Figure 2.12 shows the comparison of the results of experiments and numerical simulations for each configuration. The model's predictions of thermal efficiency for each configuration is close to the

experimental results and shows the same trends. The model underpredicts the experimentally measured efficiency by 1.78% on average. This is possibly due to variation in experimental quantities that are held constant in the simulation, such as firepower. Configuration 3 gives the best performance, with an average thermal efficiency of 35.9%, an increase of 6.8% over Configuration 1 and 5.5% over Configuration 2.

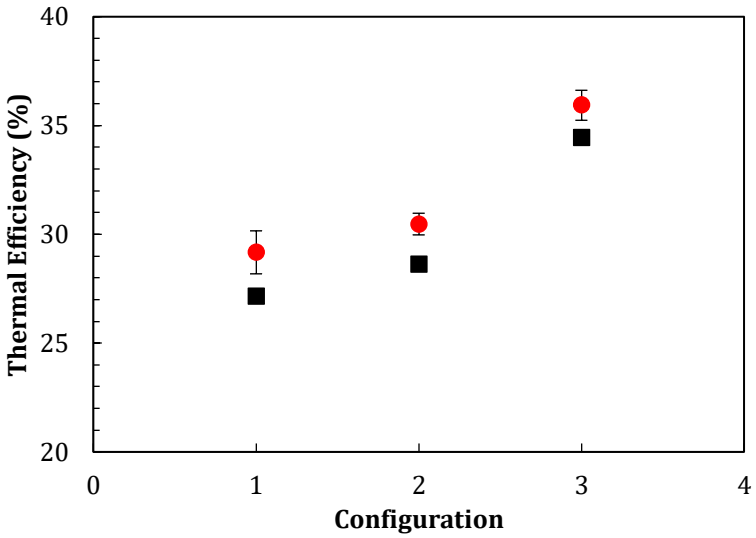

Figure 2.12: Thermal efficiency of three cone deck configurations. The red markers are experimental results with 90% confidence intervals and the black markers are numerical results. Configuration 1 is a cone deck with X = 108 mm, Y = 20 mm, and pot support height = 11 mm. Configuration 2 is a cone deck with X = 108 mm, Y = 10 mm and pot support height = 11 mm. Configuration 3 is a cone deck with X = 108 mm, Y = 10 mm and pot support height = 9 mm.

In order to understand the effect of the shape of the cone deck on the thermal efficiency, the thermal efficiency of the cookstove is plotted as a function of the airflow rate through the cookstove, shown in Figure 2.13(A). The efficiency of the cookstove, for differing cone deck configurations, is linearly dependent on the air flow rate through the cookstove. These data suggest the shape of the cone deck controls the flow of air through the cookstove via the different pressure drops associated with the designs. As with the pot support height analysis, the increased pressure drop due to more constricted designs leads to an increase

in the bulk temperature of the gas, which in turn increases heat transfer to the cookpot and efficiency. Figure 2.13(B) shows that the averaged gas temperature at the riser outlet increases with reduced air mass flow rate, which supports the hypothesis that pressure drop and total air flow rate impact efficiency through average gas temperature.

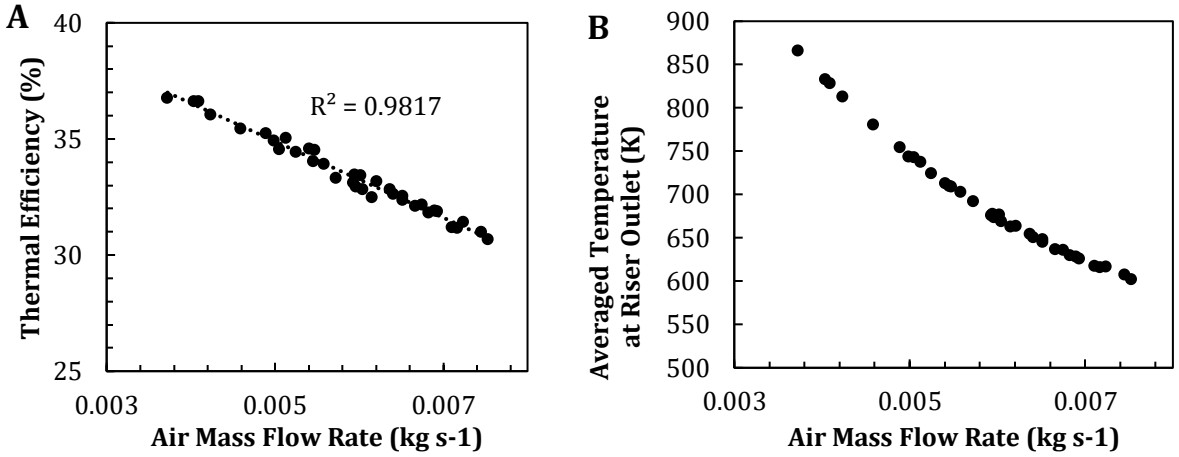

Figure 2.13: Predicted thermal efficiencies and bulk temperatures for various cone deck configurations (A) Thermal efficiency as a function of air mass flow rate. Each point represents a specific cone deck configuration. The dotted line is a linear trend line. (B) Mass-averaged temperature at the mouth of the riser as a function of air mass flow rate. Each point represents a specific cone deck configuration.

2.5.5 Relationship Between Airflow Rate and Thermal Efficiency

The relationship of airflow rate and thermal efficiency is examined by comparing the pressure drop across the cookstove for different baffle and cone deck configurations. Figure 2.14(A) shows the predicted mass flow rates through the cookstove as a function of the predicted pressure drop through the cookstove for various baffle and cone deck configurations. The mass flow rate through the stove is inversely related to the pressure drop, as expected. The thermal efficiency as a function of the pressure drop in Figure 2.14(B) shows two distinct behaviors. In the variations of cone deck configurations, the thermal

efficiency increases linearly with the pressure drop suggesting that the decrease in air flow results in higher efficiency due an increase in average bulk temperature. In the case of the baffles, the increasing pressure drop was associated with a decrease in thermal efficiency because the of the loss of heat to the walls due to enhanced mixing. This supports the hypothesis that only reducing excess air might not lead to an increase in thermal efficiency; the location where flow is obstructed is important and needs careful consideration.

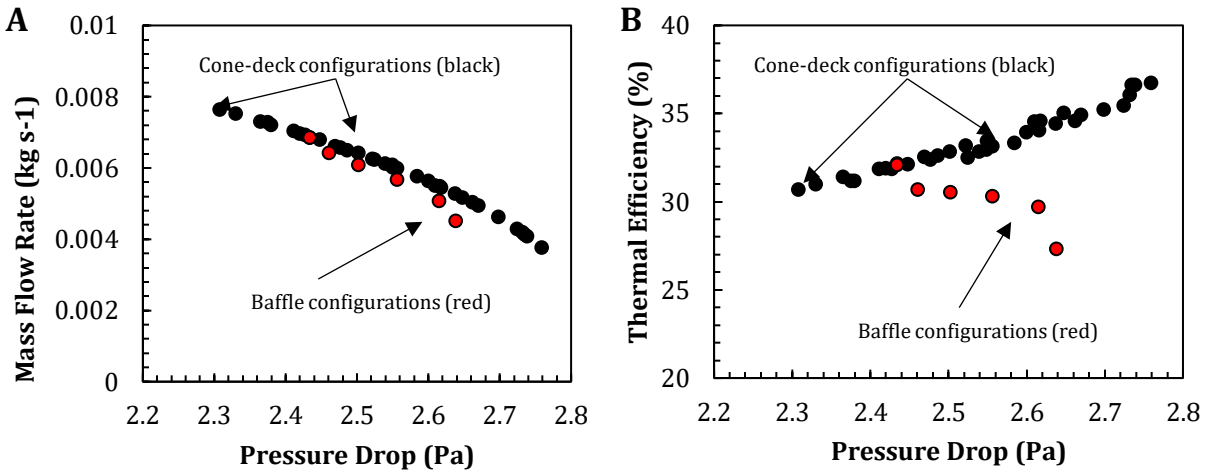

Figure 2.14: Predicted mass flow rates and thermal efficiencies for various cone deck configurations and baffle sizes. Each point represents a specific cone deck/baffle configuration. Black markers represent cone deck configurations and red markers represent baffle configurations. (a) Mass flow rate through the cookstove as a function of predicted pressure drop. (b) Thermal efficiency of cookstove as a function of predicted pressure drop.

2.5.6 Analysis of Fluid Flow

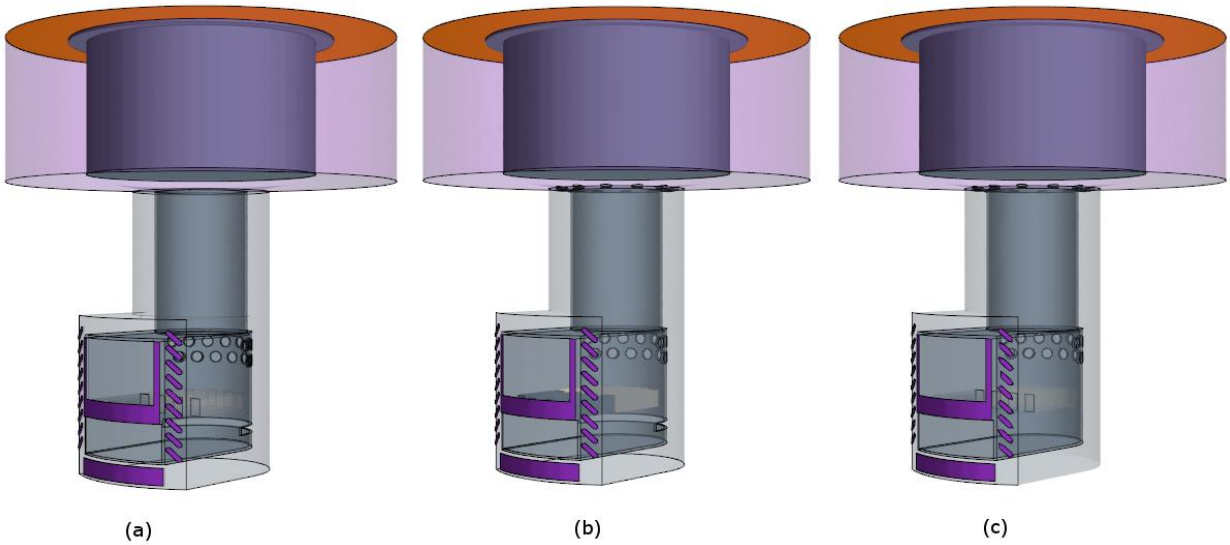

Figure 2.15: The three configurations of the cookstove studied. (A) Baseline configuration, (B) Baseline configuration with holes in the cone deck, (C) Baseline configuration with holes in the cone deck and rectangular hole at the back of the combustion chamber blocked. The air inlets are shown in pink and the outlet is shown in orange.

This section reports results from the investigation of fluid flow in three wood-burning cookstove configurations, shown in Figure 2.15. These configurations explore design features that cannot be modeled using a two-dimensional axisymmetric model, such as secondary air entrainment from a set of holes in the front of the cookstove. Results are obtained using the three-dimensional model described in Section 2.3. The model is applied to a baseline cookstove configuration along with two other configurations that modify the secondary flow path. The baseline configuration, shown in Figure 2.15(A) has three air inlets, designated Inlet 1 (primary air), Inlet 2 and Inlet 3 (secondary air). Air from Inlet 1 goes directly into the combustion chamber and mixes with the wood volatiles. Air from Inlet 2 goes around the sides of the combustion chamber, in the cavity between the radiation shield and the combustion chamber, while air from Inlet 3 travels under the combustion chamber in the same cavity. The back wall of the combustion chamber contains a set of circular orifices

at the top and a larger rectangular opening at the bottom. Secondary air is entrained into the main chamber from these holes. Figure 2.15(B) shows the second configuration, in which holes have been drilled into the cone deck. This gives an added pathway for secondary air injection into the main flow. The third configuration studied is shown in Figure 2.15(C), which is identical to the second configuration except for the blockage of the rectangular opening at the bottom of the combustion chamber. Each configuration has a 'choke ring' between the combustion chamber and riser, which reduces the cross-sectional area at that point in the flow path.

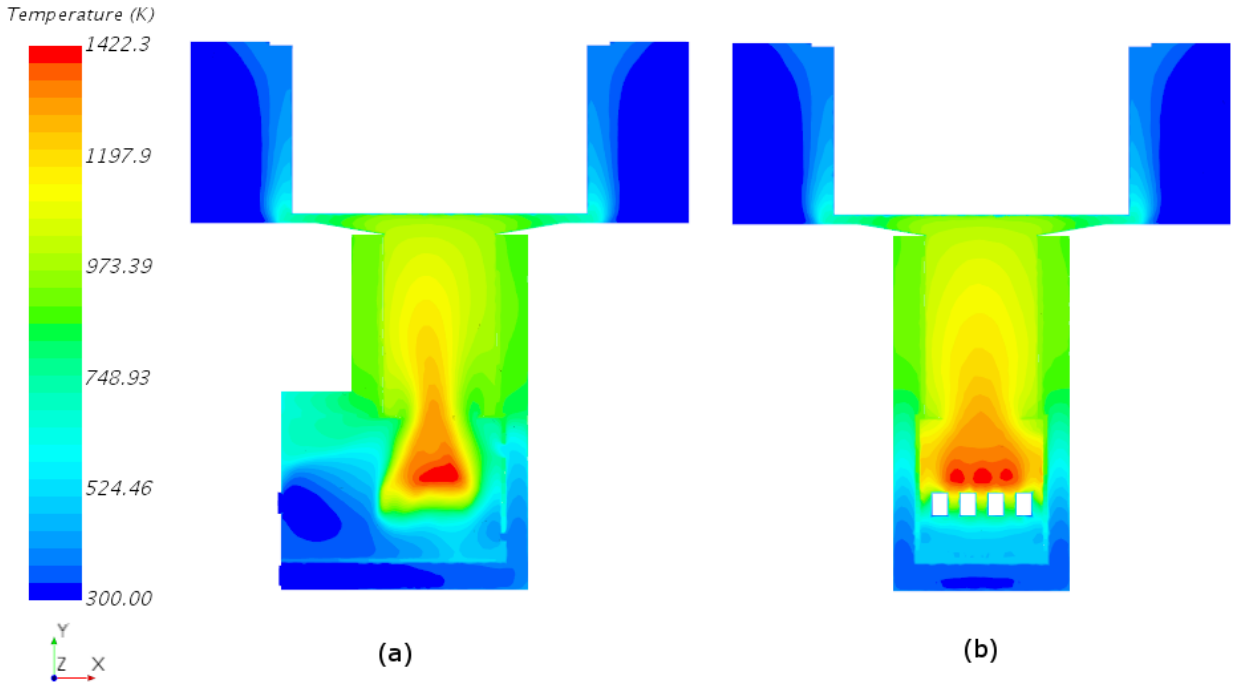

Figure 2.16: Temperature distribution on cross-sections passing through the centerline of cookstove with the first configuration. (A) Side view, (B) Front view

Figure 2.16 shows the temperature distributions on two cross-sections of the baseline configuration. Figure 2.16 (A) shows a plane passing through the center of the riser from the side and Figure 2.16 (B) shows a plane passing through the center of the riser from

the front. The choke ring mixes the volatiles and breaks up the flame, as evidenced by the uniform temperature distribution downstream of the choke ring. The flame is also seen to be pushed slightly towards the front of the cookstove. Axial conduction can be observed in the metal radiation shield, which is hotter than the surrounding gas in the bottom part of the combustion chamber due to heat conduction from the riser. The entire radiation shield is assumed to be contiguous, with no contact conduction resistance. The shield is also unconnected to the outer body; the underlying assumption is that the internal metal does not conduct heat to the outside. This is a simplification from actual stove models, where contact conduction between the inner and outer body is of importance. Similar characteristics, such as a centered flame and a relatively uniform temperature profile downstream of the choke ring, can be observed in Figure 2.16(B). This configuration has a heat transfer efficiency of 37.5%, as predicted by the CFD model. Table 2.5 shows the predicted airflow rate from each inlet and the predicted thermal efficiency of each configuration.

Configuration	Inlet 1 (SLPM)	Inlet 2 (SLPM)	Inlet 3 (SLPM)	Excess Air (%)	Efficiency (%)
Config 1	64	5	56	130	37.5
Config 2	72	14	49	153	38.7
Config 3	65	7	61	145	39.1

Table 2.5: Predicted airflow rate, excess air and thermal efficiency for each configuration studied.

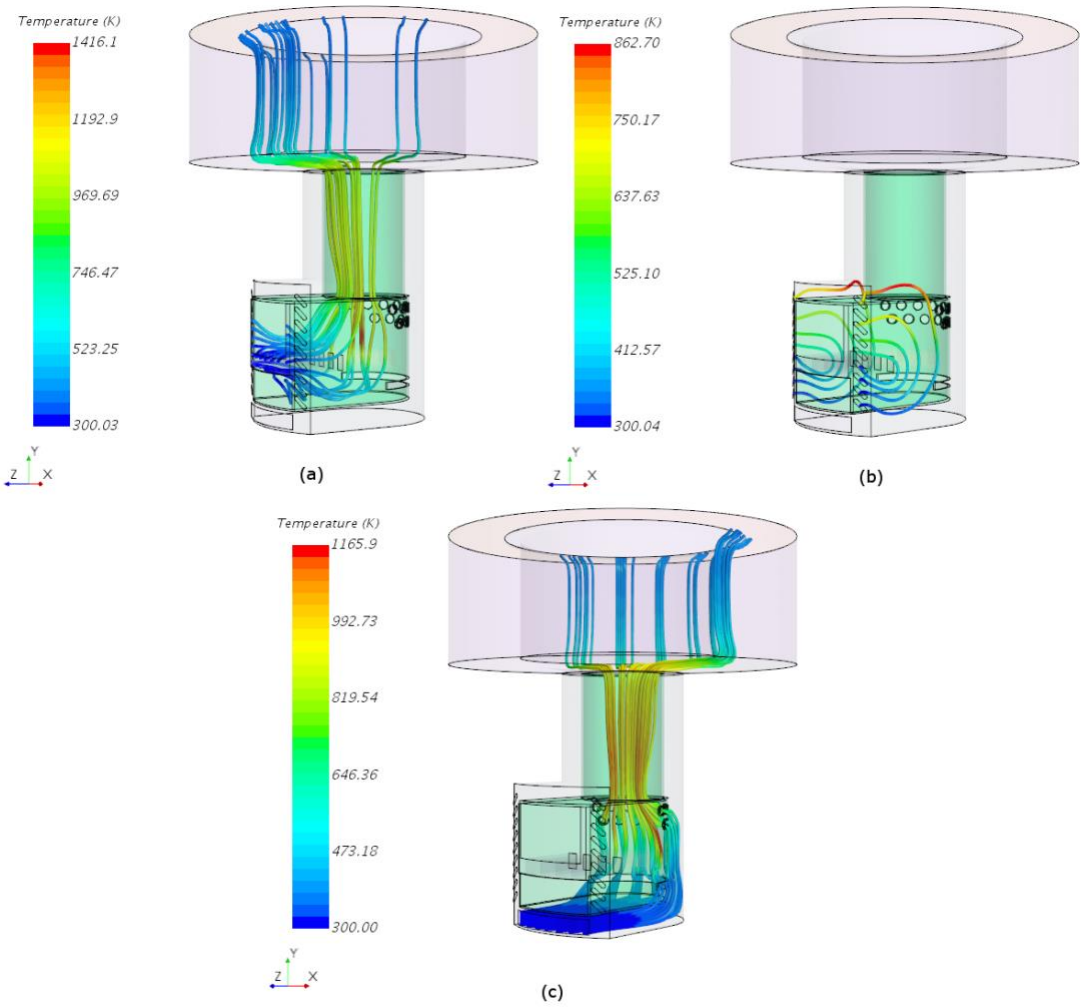

Figure 2.17: Streamlines of flow for Config 1 originating from (A) Inlet 1, (B) Inlet 2, (C) Inlet 3.

Figure 2.17 (A), (B) and (C) show the streamlines of flow emanating from Inlets 1, 2, and 3 of the cookstove with the first configuration, respectively. The temperature of the gas in the streamlines is indicated by the color. Most of the flow from Inlet 1 goes through the combustion chamber and the riser and spreads out over the front and side of the pot. Flow from Inlet 2, however, enters through the bottom holes and exits from the top holes. Therefore, airflow from Inlet 2 does not contribute to combustion in the cookstove. This is confirmed from the analysis of mass flow rates from each inlet; out of a total airflow rate of 125 SLPM (which corresponds to an excess air of 130%) through Inlets 1, 2 and 3, only 5

SLPM is contributed by Inlet 2, with about 64 SLPM contributed by Inlet 1 and the rest (56 SLPM) by Inlet 3. While the flow from Inlet 2 does not contribute to combustion, the hot flow exiting from the top holes takes away some of the heat, reducing the efficiency of the cookstove, but also cooling the front part of the combustion chamber, possibly increasing the durability of the metal. Flow from Inlet 3, shown in Figure 2.17(C), is injected into the combustion chamber from the holes at the back of the combustion chamber and spreads out over the back half of the pot. The flow entering the combustion chamber from the back is responsible for pushing the flame to the front of the cookstove, as seen in Figure 2.16(A). The streamline plots show that the flow from the three different inlets spreads out over different parts of the pot and is not well mixed.

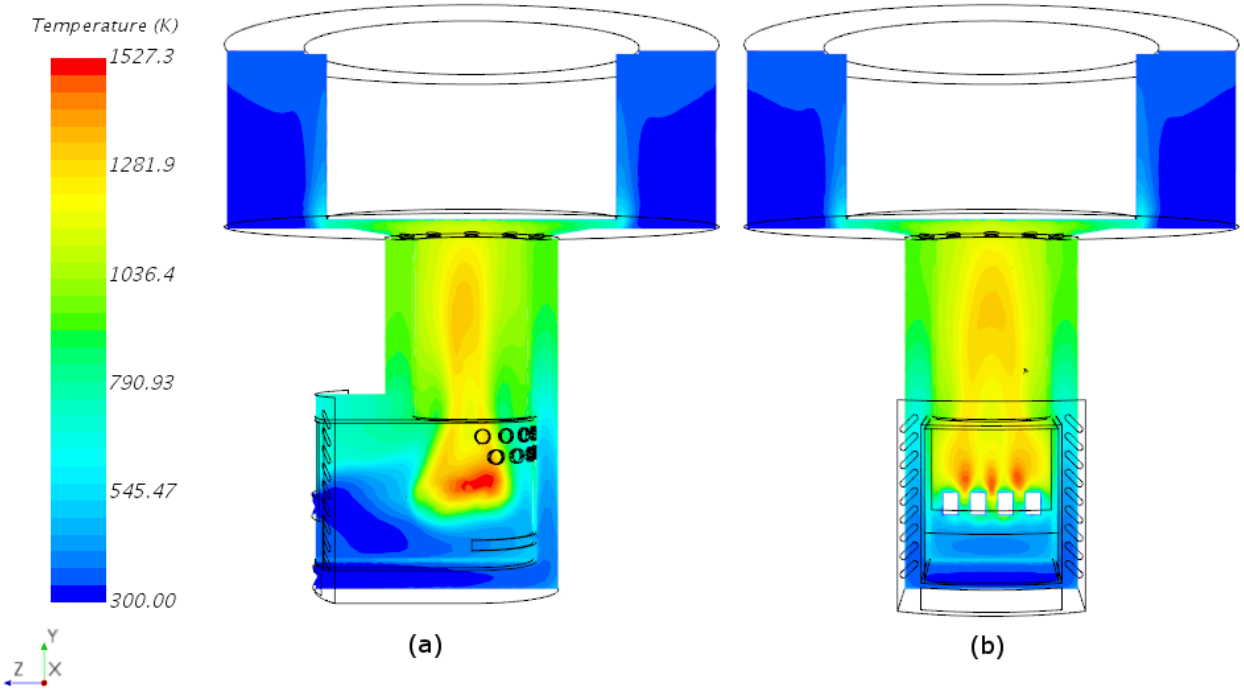

Figure 2.18: Temperature distribution on cross-sections passing through the centerline of cookstove with the second configuration. (a) Side view, (b) Front view.

The second configuration includes holes at the top of the cone deck, such that the top of the radiation shield is connected to the cone deck directly. Therefore, the secondary air

has one more possible pathway for injection into the main flow. Figure 2.18 shows the temperature distributions on two cross-sections of the baseline configuration. Figure 2.18(A) shows a plane passing through the center of the riser from the side and Figure 2.18(B) shows a plane passing through the center of the riser from the front. While the flame seems reasonably centered, it is not as well mixed as in the first configuration. This configuration has a predicted airflow rate of 138 SLPM, with the primary air inlet (Inlet 1) contributing 72 SLPM, Inlet 2 contributing 17 SLPM and Inlet 3 contributing 49 SLPM. The excess air in the cookstove is 153%. The heat transfer efficiency of this configuration is predicted to be 38.7%.

Figure 2.19(A), (B) and (C) show the streamlines originating from Inlets 1, 2 and 3 of the cookstove with the second configuration, respectively. Figure 2.19(A) shows that the flow from Inlet 1 travels through the combustion chamber and spreads uniformly all around the pot, unlike in the first configuration. Unlike in the first configuration(Figure 2.17(B)), very little of the flow from Inlet 2 loops back and exits from the top of secondary air inlets, shown in Figure 2.19(B). However, only a little of the flow is injected into the combustion chamber, with most the flow traveling up to the holes in the cone deck and being injected downstream of the riser. A similar situation is observed in Figure 2.19(C). Therefore, the combustion chamber runs richer stoichiometry-wise in this configuration as compared to the first configuration. The higher efficiency of this configuration can also be explained by the lower excess air in the combustion chamber and riser; the gas that contacts the pot first is hotter and hence transfers more heat to it. The top sets of holes in the back of the combustion chamber again do not seem to contribute to secondary air injection into the combustion chamber.

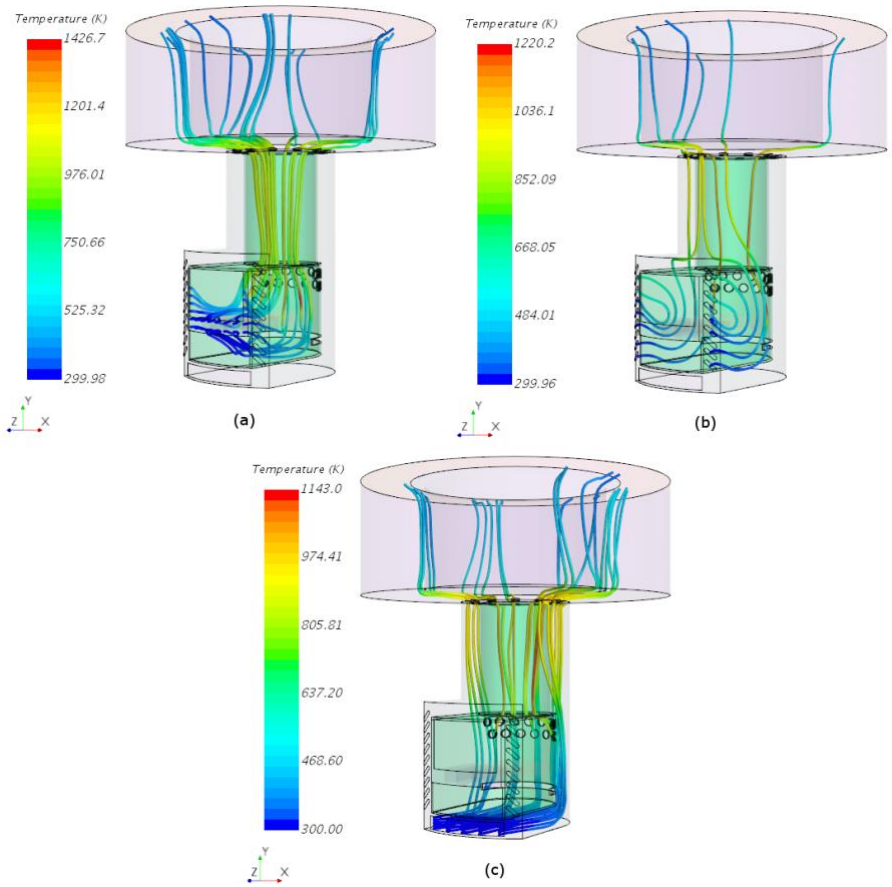

Figure 2.19: Streamlines of flow for Config 2 originating from (a) Inlet 1, (b) Inlet 2, (c) Inlet 3.

The third configuration is identical to the second configuration except that the rectangular hole at the bottom-back of the combustion chamber has been blocked off. Figure 2.20(A) and (B) show the temperature distribution in the cookstove on planes passing through the centerline of the stove from the front and the side. Like the second configuration, the flame appears to be reasonably centered. Mixing in the riser seems to be the poorest in this case of all configurations. A pocket of relatively cold air can be observed surrounding the flame in Figure 2.20(A). The total air flow rate for this configuration is 133 SLPM, which corresponds to 145% excess air. Inlet 1 supplies about 65 SLPM, while Inlet 2 and 3 supply 7 SLPM and 61 SLPM, respectively. Like in Configuration 1, Inlet 2 supplies negligible airflow

in this configuration. The heat transfer efficiency of this configuration is predicted to be 39.1%.

Figure 2.21 (A), (B) and (C) show streamlines of flow originating from the three inlets, respectively. Streamlines from Inlet 1are very similar to the second configuration, with flow going through the combustion chamber and riser, and spreading out evenly over the pot. Flow from Inlet 2, however, seems to be pushed forwards due to the presence of the blockage at the back of the combustion chamber. Some of the flow from Inlet 2 loops back and exits out of the inlet, as shown in Figure 2.21(B). Virtually none of the flow makes it into the combustion chamber, instead going up the front of the stove and being injected into the main flow downstream of the riser, thereby not contributing to the combustion. As seen in Figure 2.21(C), flow from Inlet 3 also does not contribute significantly to combustion and is injected into the main flow from the holes in the cone deck.

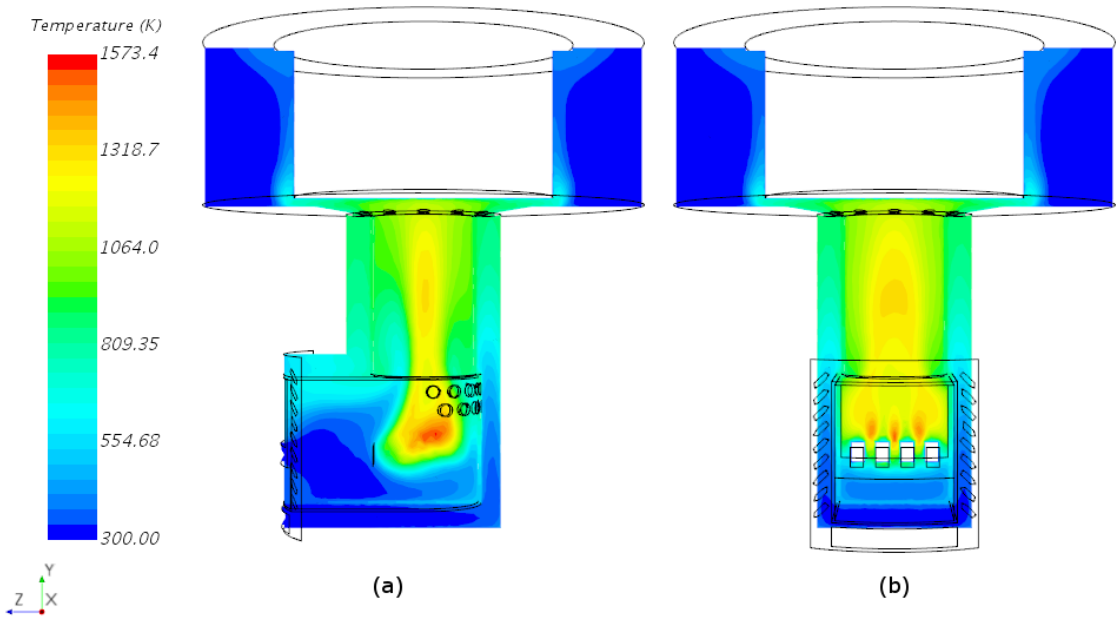

Figure 2.20: Temperature distribution on cross-sections passing through the centerline of cookstove with the third configuration. (A) Side view, (B) Front view.

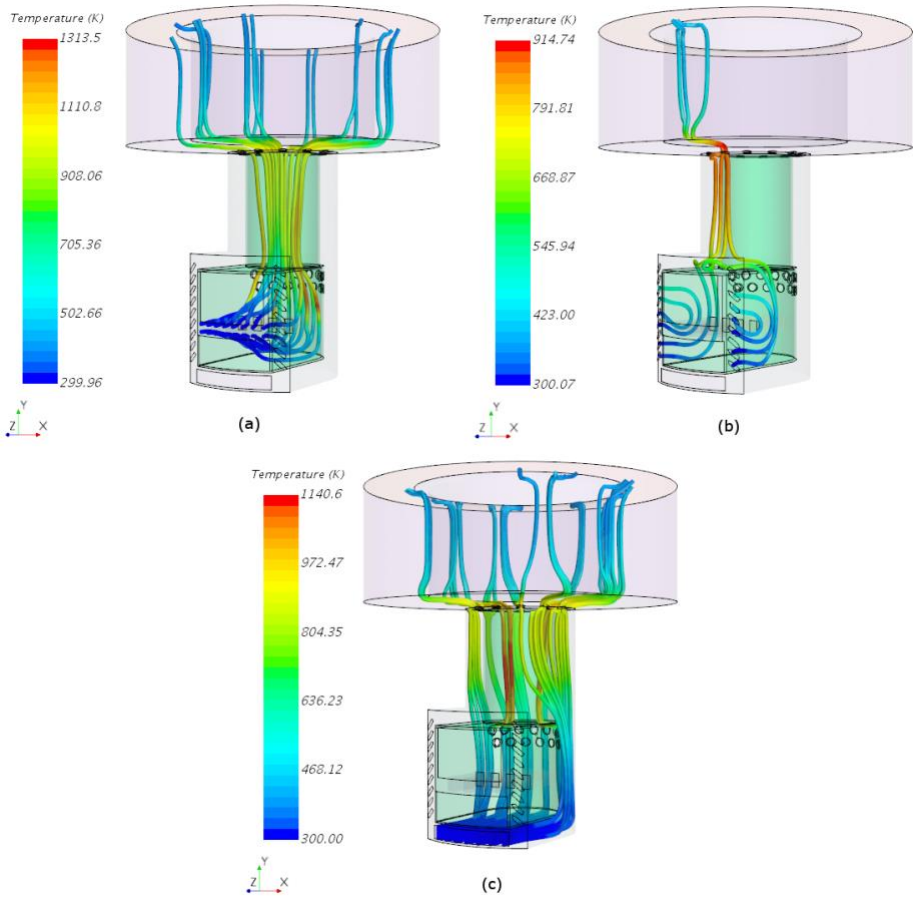

Figure 2.21: Streamlines of flow for Config 3 originating from (A) Inlet 1, (B) Inlet 2, (C) Inlet 3.

2.6 Summary

The development of and results from two CFD models for studying combustion, fluid flow, and heat transfer in natural draft cookstoves was presented in this chapter. The axisymmetric model is calibrated and validated against experimental data and is found to accurately predict the excess air through the cookstove and the temperature distribution between the pot and pot skirt. The excess air in the cookstove is found to be several times stoichiometric air for almost every configuration, except those where the flow is severely constricted due to a narrow passage. A general design goal is to reduce the excess air which acts as a diluent while maintaining sufficient mixing to ensure the reduced air flow still

provides complete fuel burnout. This allows the design to achieve the highest possible bulk temperature inside the cookstove, which promotes heat transfer and high efficiency.

Various geometric parameters such as the height of the pot supports, cone deck shape, secondary air entrainment, and central baffles of various sizes placed within the riser are analyzed. The pot support height is found to have a strong effect on the excess air ratio as well as the stove efficiency, consistent with previously published literature. Secondary air entrainment by itself is found to be ineffective in increasing the mixing or heat transfer efficiency in the cookstove. In order to increase the mixing and cut down on the excess air, central baffles blocking between 0 and 75% of the area of the riser were introduced into the flow via simulation. We found that secondary air entrainment, when used in conjunction with a central baffle, led to a decrease in the total airflow rate and an increase in turbulent mixing downstream of the baffle, which led to better mixing that may reduce $PM_{2.5}$ emissions. The central baffle may, however, reduce stove efficiency by increasing heat losses to the cone deck and riser walls via enhanced gas mixing.

The effect of the shape of the cone-deck on the thermal efficiency is investigated by modeling 36 different cone deck configurations. The results suggest that the shape of the cone-deck primarily impacts the total airflow rate through the cookstove. A reduction in airflow causes the bulk temperature to increase, which leads to an increase in thermal efficiency. Based on these findings, three cone deck configurations were experimentally tested and shown to agree well with the predicted efficiencies.

The cone-deck and baffle are all shown to reduce the amount of air flowing through the cookstove, but their effects on thermal efficiency are different, such that a similar air mass flow rate for various configurations resulted in different stove efficiencies. This

suggests that care should be taken when reducing excess air flow in the stove to avoid increasing heat transfer to the stove body or the environment.

Fluid flow and mixing in three different configurations of a cookstove are analyzed using the three-dimensional model. The presence of a choke ring just upstream of the riser leads to relatively well-mixed flow in the riser. Secondary air from cut-outs in the front of the stove of all three configurations is found to be ineffective for airflow into the combustion chamber but is effective for cooling the front of the combustion chamber, possibly increasing the durability of the cookstove.

Chapter 3 : Experimental Study of Soot Emissions from Turbulent Ethylene Flames Impinging on a Cold Surface

3.1 Overview

In this chapter, soot formation is experimentally investigated in a vertically oriented turbulent ethylene non-premixed flame impinging on a cold surface. The cold surface is a stainless-steel cylindrical receptacle maintained at 373 K. The jet velocity, nozzle diameter and distance of the surface from the nozzle are varied in the experiments. Soot mass emissions are measured using a Tapered Element Oscillating Microbalance, and the particle size distributions of emitted soot are measured using a Scanning Mobility Particle Sizer. Soot emissions are measured for free flames as well as flames impinging on the pot. Soot yield data is analyzed in terms of parameters such as the Richardson's Ratio, which quantifies to what degree the flame is buoyancy or momentum driven, and jet exit strain rate, which serves as a characteristic strain rate for the entire flame.

3.2 Experimental Methods

This section describes the experimental methods used to measure soot mass emissions and size distributions from the flame configurations studied. The experimental setup is described, followed by the details of the flames investigated.

3.2.1 Experimental Setup

Figure 3.1(A) shows a schematic of the experimental system used to measure emissions. The nozzle is placed in an exhaust hood closed on three sides, which is connected to stainless steel ducting. The fuel gas, 99.95% ethylene (C_2H_4), issues out of the cylindrical nozzle in vertical orientation into still air at standard laboratory conditions. The fuel gas flow rate is set by a bubble flowmeter (Gilibrator-2, Sensidyne, St. Petersburg, FL, USA). Ethylene is chosen as the fuel due to its propensity for high soot emission and its extensive use in free flame soot studies [52,61,65,66]. The flow rate through the hood is monitored by a pitot type flow sensor (3100 Diamond Flow Sensor, Nailor, Houston, TX, USA). An inline duct fan (S-600, Vortex Powerfans, Terrebonne, Canada) set at 180 cfm maintains constant flow in the emissions system ducting, which results in a hood face velocity of 0.08 m/s. The hood and ducting flow rates were confirmed by releasing 99.99% CO_2 gas at a known volumetric flow rate into the hood and measuring the CO_2 concentration downstream at a sample port. Multiple CO_2 samplings performed along the duct radius suggested that the gas was well mixed at the first sampling location.

CO (VIA-510, Horiba, Kyoto, Japan) and CO_2 (PIR-2000, Horiba, Kyoto, Japan) concentrations, soot mass emissions (TEOM 1405, ThermoFischer Scientific, Waltham, MA, USA), and soot particle size distributions (TSI SMPS 3910, Shoreview, MN, USA) are measured in real-time. The TEOM (Tapered Element Oscillating Microbalance) system is a

real-time, direct mass measurement system for particulate matter, which works on the principle that the frequency of natural oscillation of a tapered oscillating element changes as particulate matter accumulates on it. The change in mass, m can be calculated by the equation,

$$m = K_o \left(\frac{1}{f_1^2} - \frac{1}{f_0^2} \right) \tag{3.1}$$

where K_o is the factory-set calibration constant, and f_o and f_1 are the measured frequencies of oscillation of the filter at an initial time and a later time, respectively. TEOM systems have been previously used for measuring particulate matter emissions from diffusion flames and diesel engines, as well as ambient particulate matter measurements [112–115]. TEOM systems were designed for particle loading consistent with ambient air monitoring, hence a dilution system (shown in Figure 3.1(B)) has been added to account for the greater PM loading. The dilution system is based on widely used commercial systems that dilute the flow using capillary tubes in the sample stream, with a separate stream open to the environment making up the balance of the flow with filtered air, both drawn by a backside pump. This particular TEOM system has been calibrated to provide results consistent with the standard gravimetric method [116]. A detailed description of the calibration procedure and system can be found in the given reference. SMPS (Scanning Mobility Particle Sizer) systems have been used to measure soot particle size distributions from a variety of flames [36,117–119].

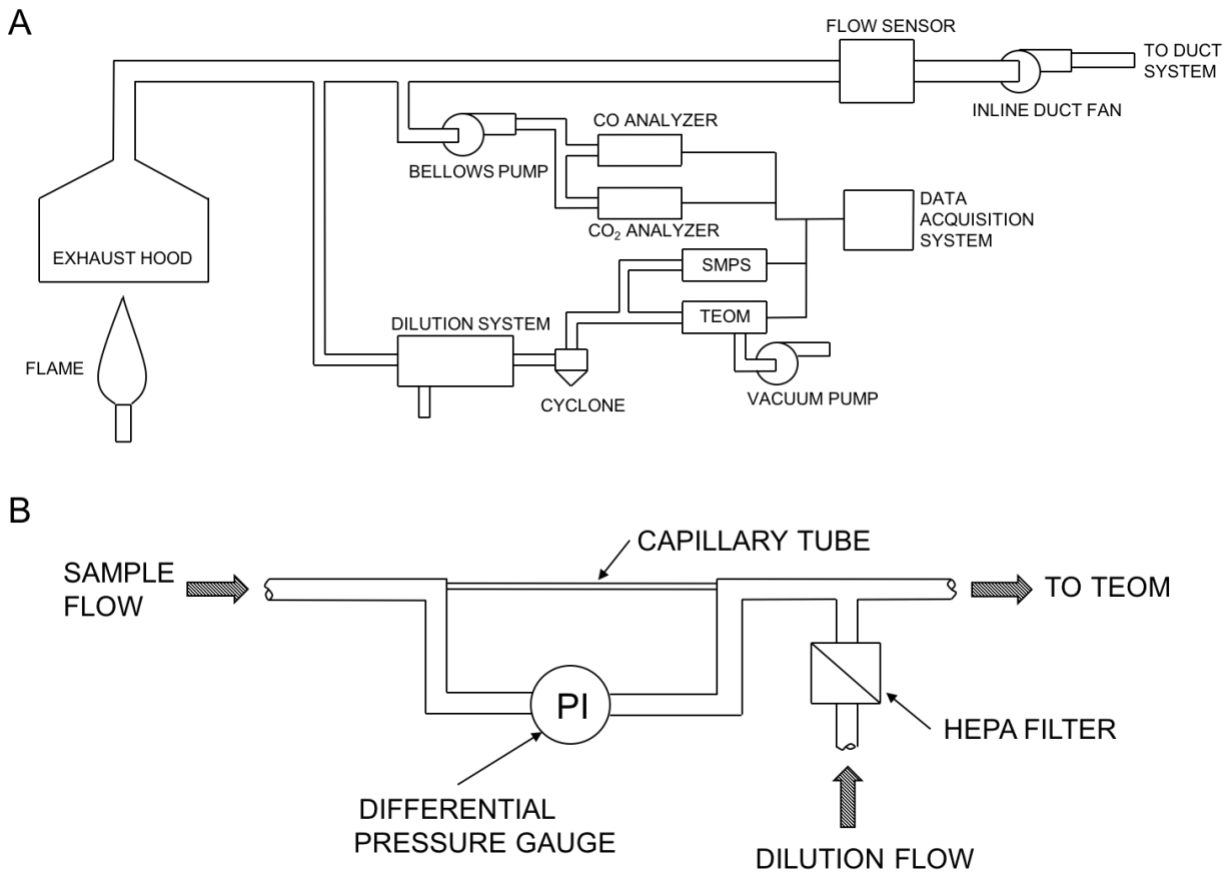

Figure 3.1: (A) Emissions capture and monitoring system. Emissions are captured by the hood and transported through the ducting. (B) Schematic of dilution system for the TEOM/SMPS system. For details, see reference [116].

3.2.2 Flame Conditions

Table 3.1 shows the details of the seventeen flames studied in this work. Four jet nozzles, with inner diameters of 1.5 mm, 2.18 mm, 3 mm and 4.5 mm are used in this study. The average jet velocity varies from 6 m/s to 80 m/s, and the heat release from 4.76 kW to 19.78 kW. These parameters are chosen so as to capture the differences in soot emission in the regimes of fully turbulent to transitional flow, as well as in buoyancy regimes ranging from forced convection to nearly natural convection. The exit Reynolds numbers vary between 3000 and 17000. All but four flames are lifted, with the flame liftoff data also provided in Table 3.1. The flame length and lift off distance are measured by time-averaging

photographs of the flame. In addition to free flames, we also study flames that impinge on a cold surface. For each flame listed in Table 3.1, a cold surface is placed at seven points between $0.15L_f$ and $0.95L_f$ from the nozzle, where L_f is the flame length [120]. The cold surface is a stainless-steel cylindrical receptacle filled with water at 373 K.

Flame	Nozzle diameter (mm)	Mean Exit Velocity (m/s)	Heat Output (kW)	Exit Reynolds Number	Flame Length (m)	Lift off (mm)	Richardson's Ratio	Exit Strain Rate (/s)
A	1.5	50	5	8300	0.410	12	120	33320
B	1.5	60	6	10000	0.430	19	90	39990
C	1.5	70	7	11500	0.440	26	70	46650
D	1.5	80	8	13200	0.450	32	60	53320
E	2.18	30	6	7200	0.480	8	240	13760
F	2.18	40	8	9600	0.520	10	180	18330
G	2.18	47	9	11300	0.570	16	160	21550
H	2.18	60	12	14400	0.600	31	120	27530
I	3	25	10	8300	0.570	4	330	8330
J	3	30	11	10000	0.630	9	280	10010
K	3	35	13	11500	0.640	12	250	11660
L	3	40	15	13200	0.700	15	220	13330
M	3	52	20	17200	0.760	26	170	17330
N	4.5	6	5	3000	0.470	0	1280	1330
O	4.5	8	7	4200	0.550	0	960	1890
P	4.5	15	13	7400	0.648	0	610	3330
Q	4.5	20	17	10000	0.741	0	480	4440

Table 3.1: Conditions for flames studied.

3.3 Results and Discussion

Figure 3.2 shows the comparison between the soot mass emission rate measured by the TEOM and that calculated from the SMPS data. The data include all experiments done as part of this study, including free flames and flames impinging on a cold surface. The SMPS measures the particle size distribution of emitted soot. The mass emission rate of soot from the SMPS data is calculated with the assumption that the soot particles are perfectly

spherical, with a density of 1800 $\mathrm{kg \cdot m^{-1}}$. The plot shows reasonably good agreement between the two quantities, with an R^2 value of 0.89. The best-fit line is found to be $y = 0.999x$, with larger measurements resulting in greater spread in the data.

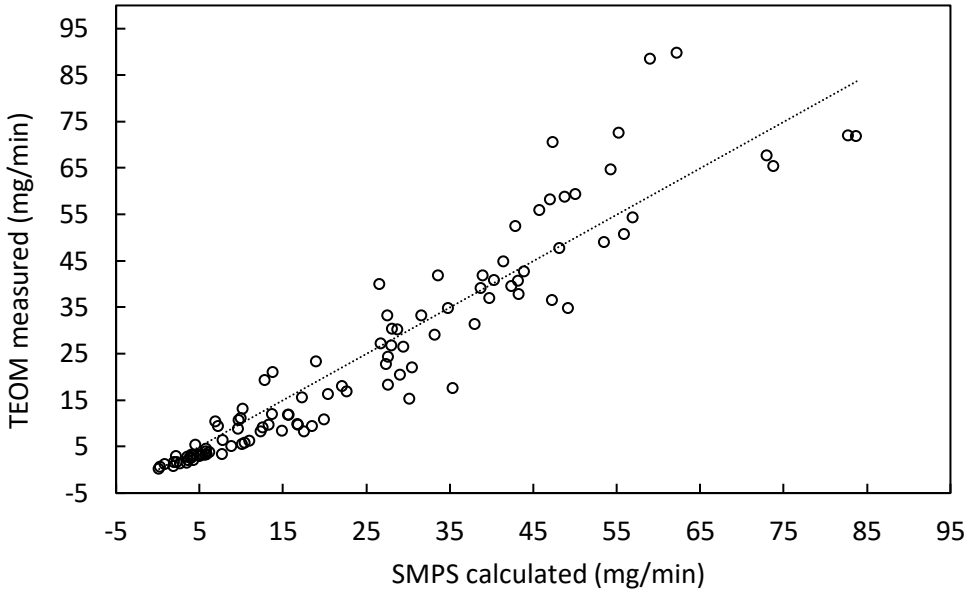

Figure 3.2: Plot of mass of particulate matter measured by TEOM and calculated from particle size distributions measured by SMPS. Each particle is assumed to be perfectly spherical in shape for the SMPS calculation. The best-fit line is found to be y=0.999x.

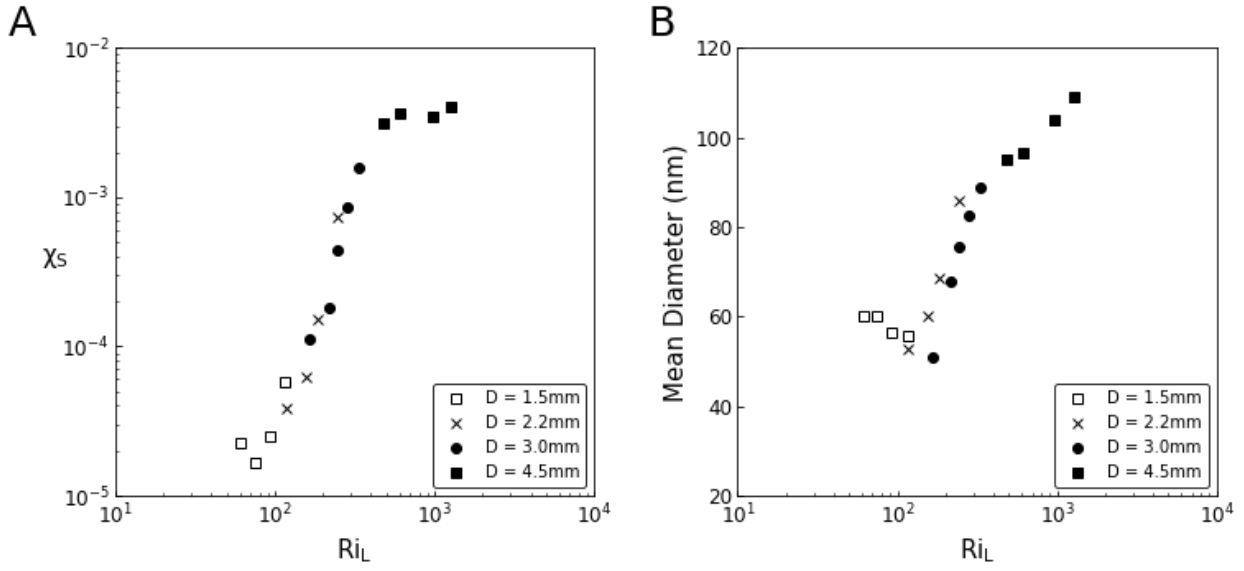

Figure 3.3: A) Plot of measured soot emission divided by carbon input as a function of buoyancy Richardson's ratio for free flames. B) Mean diameter of measured soot as a function of buoyancy Richardson's ratio for free flames. Different types markers represent diameters of jets.

3.3.1 Free Flames

Data from the free flames are first examined in terms of the buoyancy Richardson's Ratio, $\mathrm{Ri_L}$, defined as the buoyancy of the flame divided by the jet momentum flux. Formulated for free-jet flames with flame length much greater than the source diameter, the Richardson ratio is defined as $Ri_L = \pi g \rho_\infty L_f^3 / 4\dot{G}_o$, where g is the acceleration due to gravity, ρ_∞ is the ambient density, L_f is the flame length, and $\dot{G}_o$ is the momentum flux at the jet exit, defined as $\dot{m}_o \mathrm{v}_{exit}$. $Ri_L \to \infty$ corresponds to a purely buoyant flame, while $Ri_L \to 0$ corresponds to a purely momentum driven flame, with buoyancy being unimportant. Soot emission is represented by the non-dimensional quantity χ_s, defined as the soot yield divided by the carbon input $\dot{m}_s/\dot{m}_C$. Figure 3.3(A) shows soot emission as a function of Ri_L. Three distinct regions are readily apparent in the plot, with the transitions occurring at $Ri_L \approx 100$ and $Ri_L \approx 500$. For $Ri_L < 100$, soot emission stabilizes at a value of $\chi_s \approx 0.0001$. The soot yield factor rises with increasing Ri_L and appears to stabilize when buoyancy becomes dominant, with an asymptotic value of $\chi_s \approx 0.004$. Similar observations were made by Becker and Liang [61] in turbulent non-premixed flames. Figure 3.3(B) shows the mean soot diameter as a function of Ri_L. Similar to Figure 3.3(A), a transition is observed at $Ri_L \approx 100$. For $Ri_L < 100$, the mean diameter stabilizes at ~ 60 nm. The mean diameter increases with increasing Ri_L and appears to asymptote towards 120 nm. Since the Richardson ratio controls the transition from momentum driven flames to buoyancy driven flames, a likely cause of this behavior in soot emission is the structural changes in the turbulence and mean flow as the flow regime changes from momentum-driven to buoyancy-driven. For the same diameter jet, residence times are longer in buoyancy-driven regime, which leads to greater

heat loss from soot particles, and hence, lower temperatures in the oxidation region [63]. This leads to less soot burnout, and increased soot emission.

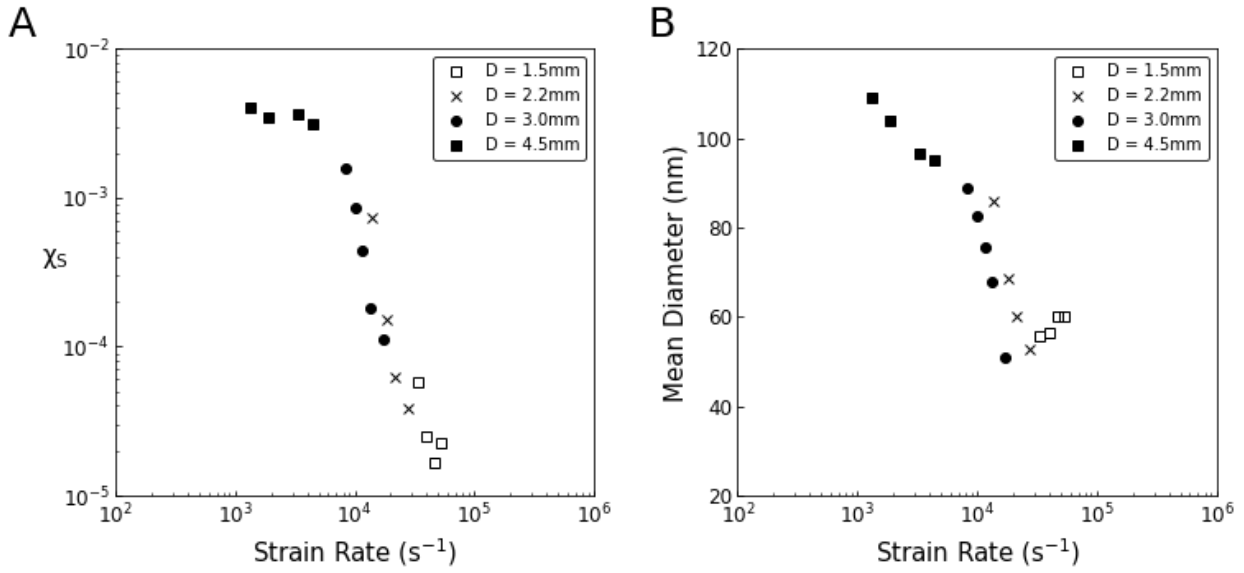

Figure 3.4: A) Plot of measured soot emission divided by carbon input as a function of jet exit strain rate for free flames. B) Mean diameter of measured soot as a function of jet exit strain rate for free flames. Different types markers represent diameters of jets.

The effect of changing the jet exit strain rate on soot emissions is presented in Figure 3.4. The characteristic strain rates in a flame can be represented by the jet exit strain rate, defined as U/D, where U is the mean exit velocity of the jet and D is the jet diameter. Figure 3.4(A) shows the soot yield factor as a function of jet exit stain rate. Two distinct regions are visible; the soot yield stays relatively constant until a strain rate of $\approx$ 6000, and reduces for greater strain rates. Figure 3.4(B) shows the variation of the mean particle diameter with strain rate. The mean diameter reduces with strain rate until a strain rate of $\approx$ 30000, and stabilizes at $\sim$ 60 nm for larger strain rates. A possible explanation for this behavior is that for strain rates below 30000, the soot formation and oxidation processes are controlled by the mixing rate, resulting in a linear dependence of the soot yield factor on the strain rate.

The mixing rate has been shown to vary linearly with the jet exit strain rate in non-premixed turbulent flames [121]. At a value of 30000, the chemical rate becomes the controlling factor, and further increases in the strain rate only marginally affect the soot formation and destruction processes. Another possible explanation is that soot inception and growth by PAHs is inhibited at high scalar dissipation rates, resulting in reduced soot yields at higher mixing rates [122].

Figure 3.5 shows the effect of the jet exit strain rate on the particle size distribution of emitted soot from free flames. For a strain rate of 1330 s^{-1}, a bi-modal distribution is observed, with the smaller mode at ~30 nm, and the larger mode at ~115 nm. As the jet exit strain rate is increased, the size distribution changes from a bi-modal distribution to a unimodal distribution, with a decrease in the size of the larger mode.

3.3.2 Flames Impinging on a Cold Surface

Data from flames impinging on the cold surface is presented and analyzed in this section. Figure 3.6 shows a plot of the soot yield factor for Flames E, F, G and H as a function of the non-dimensional surface height, h^*, defined as the height of the surface from the jet exit divided by the measured flame length. Each flame has a jet diameter of 2.2 mm, with the heat release varying from 6 kW to 12 kW, the exit Reynolds number from 7200 to 14400, and Richardson's ratio from 244 to 117. The presence of the cold surface causes a significant increase in soot yield compared to the free flame emission. The soot yield factor for each flame increases with h* for values less than ~0.5 and is seen to decrease with further increase in h*. Figure 3.6 also shows that less soot is emitted from flames with increasing exit velocity (and by definition, the strain rate), with the curves become flatter as the exit

strain rate of the jet increases. Similar trends are observed for all other flames in this study (The full experimental dataset can be found in Appendix C).

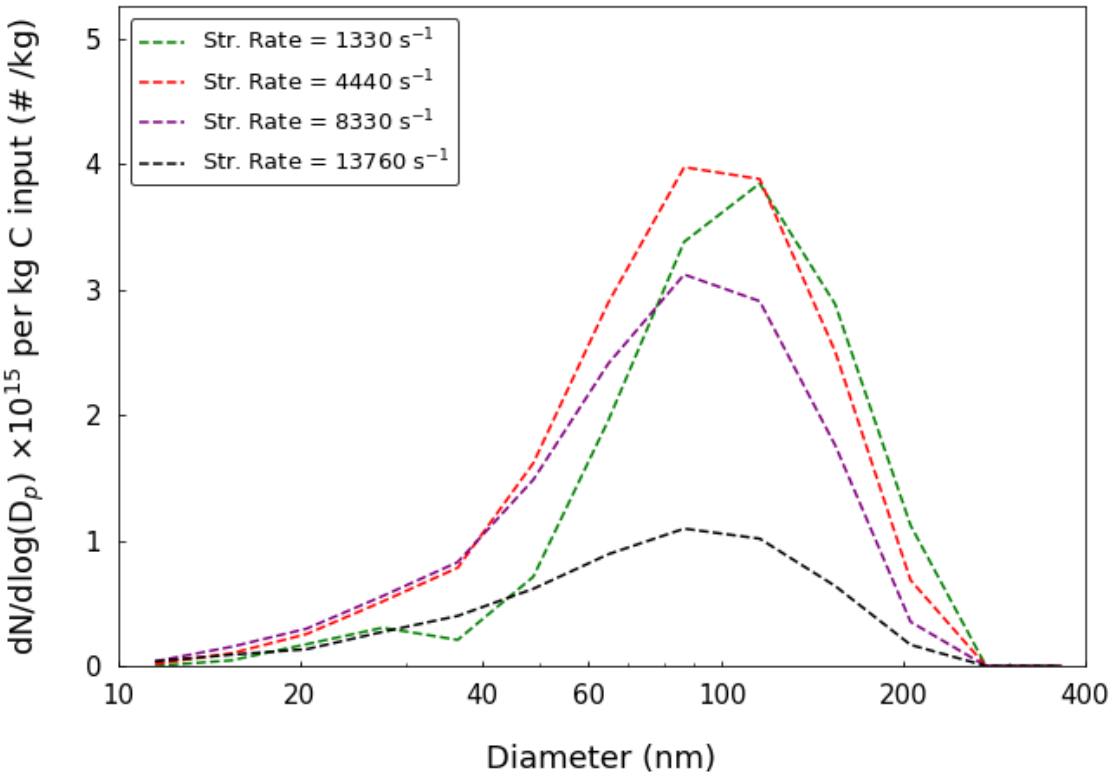

Figure 3.5: Measured particle size distributions of emitted soot as a function of jet exit strain rate for free flames.

A possible cause of the trend in χ_S with h* is that the presence of the cold surface results in reduced nucleation of new soot particles at low h*, or due to reduced surface growth. The presence of a cold surface in the nucleation zone could inhibit soot nucleation because of reduced PAH formation due to disruptions in the flame structure and heat loss to the cold surface. This would result in fewer sites for surface growth, and hence, reduced soot emission. The cold surface might also inhibit the production of C_2H_2, which is required for surface growth. As h* increases, the surface would move out of the nucleation zone, resulting

in more nucleation. The cold surface quenches the soot oxidation process, freezing the soot concentration at a higher value and leading to a higher soot yield factor than observed from a free flame. As h* increases further, the cold surface moves out of the oxidation zone, and the soot oxidation process is no longer quenched. This causes a reduction in the soot emission, as greater amounts of soot are oxidized with further increases in h*. A possible cause of the flattening of the curves with increasing strain rate is that the total amount of soot present at any radial slice in a turbulent non-premixed flame decreases with increasing jet exit strain rate [121].

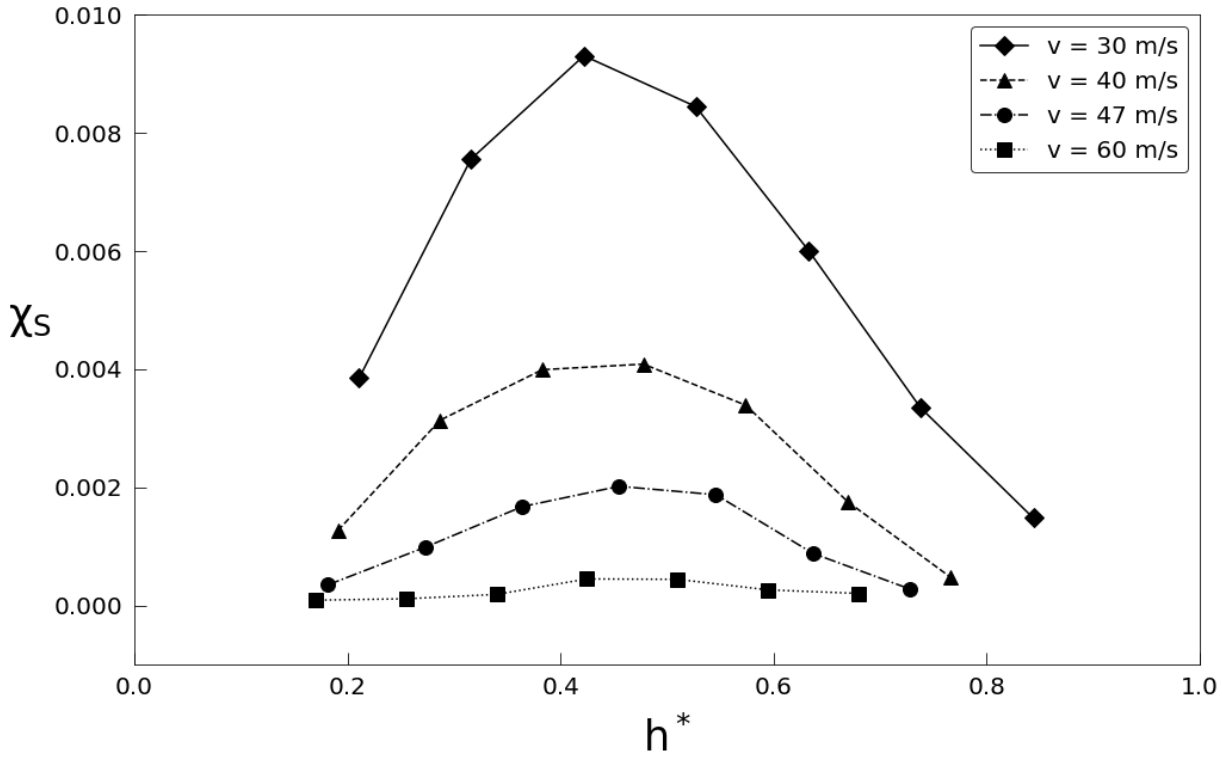

Figure 3.6: Plot of soot yield factor for Flames E, F, G and H impinging on a cold surface as a function of non-dimensional surface height h*, defined as the height of the surface from the jet exit divided by the flame length.

Figure 3.6 furthers shows that the largest soot yield factor is obtained at approximately the same h* for each flame. The mean h* for maximum soot yield across the

entire experimental dataset is found to be 0.46 with a standard deviation of 0.09. This is close to the point of maximum soot volume fraction in the turbulent non-premixed ethylene flames studied by Kent and Honnery [52], which are very similar to the flames studied in this work. However, these numbers should be treated with some caution due to uncertainties in the measurement of the flame length.

Figure 3.7 shows the evolution of the particle size distribution of emitted soot for Flame E with increasing h*. The size distribution for each case appears to be bimodal, with the smaller mode at approximately 27 nm and the larger mode around 115 nm, with the diameters of both modes staying relatively constant over the range of h*. The number of particles in the smaller mode do not appear to change with h*, while those in the larger mode follow the same trend as the soot yield factor, i.e., initially increase with h*, then decrease with further increases in h*. Bimodal particle size distributions have previously been observed and predicted in premixed flames and laminar non-premixed flames [109,123], whereas data for non-premixed turbulent flames are somewhat lacking. In laminar diffusion flames, the smaller mode has been attributed to particles formed due to nucleation from PAHs, while the larger mode has been attributed to particles grown due to coagulation and surface growth [87].

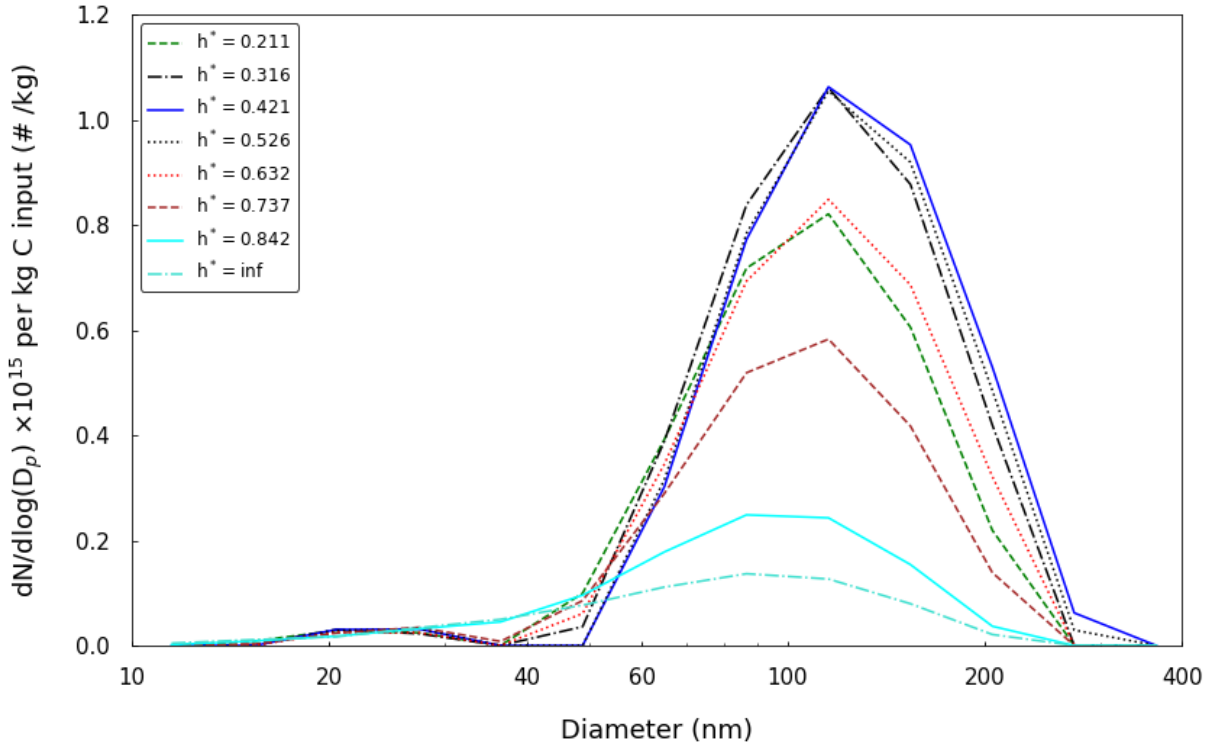

Figure 3.7: Measured particle size distribution for Flame E for a cold surface placed at an h* of 0.211, 0.316, 0.421, 0.526, 0.632, 0.737, 0.842 and infinity (free flame).

3.4 Summary

Soot emission data from vertically oriented turbulent non-premixed ethylene flames has been obtained and analyzed, including free flames and flames impinging on a cold surface placed within the flame. The data include soot mass emission rates measured by a Tapered Element Oscillating Microbalance and soot particle size distributions measured by a Scanning Mobility Particle Sizer.

Soot yield factors and mean particle diameters from free flames are found to be strongly correlated with the Richardson's ratio, as well as the jet exit strain rate. A possible explanation for the dependence on strain rate is that soot inception and growth by PAHs is inhibited at high scalar dissipation rates, resulting in reduced soot yields at higher mixing

rates. The mean diameter and soot yield factor also stabilize for flames with $Ri_L < 100$, i.e., when the flames are momentum driven.

Soot yields for a flame impinging on a cold surface at any height are found to be greater than soot yields of that flame without an obstruction in it. The soot yield factor increases, then decreases as the cold surface is moved away from the nozzle, i.e., with increasing non-dimensional surface height h*. The point of maximum soot is found to be h* = 0.46, averaged across all experimental data. A possible explanation for the increase in soot emission is that the presence of the cold surface quenches soot oxidation, resulting in increased soot emission. However, if the surface is placed closer to the jet, nucleation of new soot particles could be inhibited due to reduced PAH formation, resulting in an increase of the soot yield factor with h*. Further increase in h* would take the cold surface out of the oxidation zone, leading to greater oxidation and hence, less emitted soot. The particle size distribution of emitted soot is found to be bimodal for nearly all flames impinging on the cold surface, with the smaller mode between 20 – 30 nm and the larger mode at ~115 nm.

Chapter 4 : Predicting Soot Emissions from Turbulent Ethylene Flames

4.1 Overview

This chapter presents the development of a numerical model for predicting in-flame soot volume fractions and the total mass of soot emitted by turbulent non-premixed ethylene flames. The model is validated using in-flame soot volume fraction data from literature. Flames G and M from the previous chapter are modeled. The model is then applied to predict the total soot emissions from a turbulent non-premixed ethylene flame impinging on a cookpot kept at varying distances from the nozzle. We compare the total soot emissions predicted by the model with experimental data, and use results obtained from the model to explain the trends observed in the experimental data from Chapter 3.

4.2 Model Development

4.2.1 Model Geometry

Figure 4.1 shows a schematic of the computational model. Ethylene enters from the fuel inlet at the bottom of the domain at the given velocity. Air at 300 K is entrained from the

bottom and the sides of the domain. The flame runs into the cookpot (when present), which is maintained at a temperature of 373 K. The cookpot used has a diameter of 240 mm and a height of 140 mm. Burnt gases escape from the outlet, which is located at the top of the domain.

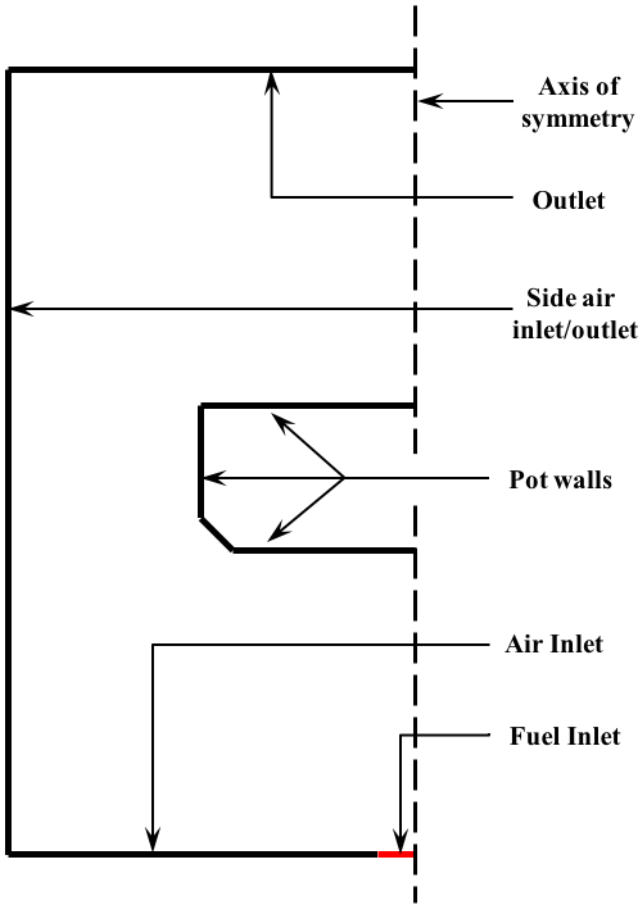

Figure 4.1: Schematic of axisymmetric computational domain.

4.2.2 Mathematical Model

The discretized Favre-averaged conservation equations for mass, momentum and energy transport are solved on the domain. Turbulence is modeled using the SST k-ω turbulence model, which is a modified form of the standard k-ω model [124]. The model solves transport equations for turbulent kinetic energy (k) and the specific turbulent

dissipation rate (ω). The equations are not reproduced for brevity and can be found in the given references. Combustion is modeled by the non-premixed flamelet method, in which transport equations for mean mixture fraction, mixture fraction variance and mean enthalpy are solved. The energy equation is closed assuming a turbulent Prandtl number of 0.85. The specific heat at constant pressure of each species is assumed to vary as a polynomial function of temperature, while the specific heat of the mixture is treated as a mass-weighted average of the specific heats of the individual species. The thermal conductivity of the mixture is also assumed to vary as a polynomial function of temperature [125]. The dynamic viscosity is computed using Sutherland's Law [97]. The turbulent Schmidt number is assumed to be constant at 0.9 [95].

Combustion Model

Species are modeled using the non-premixed non-adiabatic flamelet method. Flamelets are generated using the CaltechMech kinetic mechanism, initially developed by Blanquart and coworkers, with later modifications made to improve its predictive capabilities [126–128]. The chemical kinetic mechanism contains 192 species and 1896 reactions and takes into account all major pathways of PAH formation. The mechanism has been validated for several configurations, such as premixed flames, diffusion flames, shock tubes and plug flow reactors. 30 flamelets are generated by solving the one-dimensional flamelet equations for species mass fractions and temperatures between a stoichiometric scalar dissipation rate of 10^{-3} s^{-1} and 192 s^{-1}. In order to include the effect of fluctuations due to turbulence on the temperature and species concentrations, joint PDF's of mixture fraction and scalar dissipation rate are created. The mixture fraction and scalar dissipation rate are

assumed to be statistically independent; therefore, the joint PDF is the product of the PDF's of mixture fraction and scalar dissipation rate. The mixture fraction PDF is assumed to be a β function. The variance of the scalar dissipation rate is assumed to be negligible (i.e. fluctuations in scalar dissipation rate due to turbulence are ignored). Hence, its PDF is assumed to be a delta function. The mixture fraction PDF's are a function of the mean mixture fraction and the mixture fraction variance. The PDF's are convolved with the instantaneous temperature and species concentration functions to obtain mean temperatures and mean species concentrations. These are tabulated as a function of the mean mixture fraction, mixture fraction variance and the scalar dissipation rate. The CFD solver obtains values for mean species distributions by looking up those values from this table.

Soot Model

Soot behavior is modeled by the Method of Moments with Interpolative Closure (MOMIC)[27,33,129]. The method of moments solves for various moments of the soot particle size distribution function. While the PSDF itself cannot be reproduced by this method, quantities such as average soot volume fraction, average particle size and total mass of soot produced can be predicted, since they can be derived from the moments of the PSDF. For example, the zeroth moment represents the number density of soot particles, while the first moment represents the volume of soot particles per unit volume of gas. Transport equations of the form

$$\frac{\partial}{\partial t}(\rho M_r) + \nabla \cdot (\rho \boldsymbol{V} M_r) = \nabla \cdot \left(\mu_{eff} \nabla M_r\right) + S_r \tag{4.1}$$

are solved for the first three moments, where M_r is the r_{th} moment, r takes the values 0, 1 or 2, ρ is the gas density, $\boldsymbol{V}$ is the velocity, μ_{eff} is the effective diffusivity, and S_r is the source term. The source term for the zeroth moment transport equation consists of the sum of the nucleation and coagulation terms. The source term for the first moment equation consists of the sum of nucleation, surface growth and oxidation terms, and the source term for the second moment equation consists of the sum of the nucleation, surface growth, coagulation and oxidation terms. Since the flow is turbulent, we assume that the effective diffusivity μ_{eff} is equal to the turbulent diffusivity. Nucleation is modeled as the collision of two pyrene molecules. Coagulation is modeled by the method proposed by Frenklach, which includes coagulation models for the continuum, free-molecular, and transitional regime [129]. Surface growth is modeled by the HACA mechanism, and oxidation by both O_2 molecules and OH radicals is considered. All rates are taken from Appel et al. [34]. The soot surface growth and oxidation rates are presented in Table 4.1. Change in speciation due to the soot model is not considered in this work. This assumption is made because gas species concentrations are much higher than soot concentrations, and hence, largely not influenced by these reactions.

No.	Reaction	$k = AT^n e^{-E_a/RT}$		
		A (cm^3 mol^{-1} s^{-1})	n	E_a (kJ mol^{-1})
S1	$C_{soot} - H + H \Leftrightarrow C_{soot^*} + H_2$	4.2×10^{13}		13.0
S2	$C_{soot} - H + OH \Leftrightarrow C_{soot^*} + H_2O$	1.0×10^{11}	0.734	1.43
S3	$C_{soot^*} + H \Leftrightarrow C_{soot} - H$	2.0×10^{13}		
S4	$C_{soot^*} + C_2H_2 \Leftrightarrow C_{soot} - H + H$	8.0×10^{7}	1.56	3.8
S5	$C_{soot^*} + O_2 \Leftrightarrow 2CO +$ products	2.2×10^{12}		7.5
S6	$C_{soot} - H + OH \Leftrightarrow OH +$ products	Reaction probability = 0.13		

Table 4.1: Reaction mechanism for soot surface growth and oxidation [34].

Soot Oxidation Model

Soot oxidation is one of the most complex and least understood aspects of soot behavior. Soot oxidation occurs mainly by the reaction of O_2 and OH with soot particles [42,43], both of which are considered in this model. Khosousi et al. [47] show that for a laminar ethylene flame, with all other model parameters being equal, the peak soot volume fraction is controlled by the OH oxidation rate, and the soot emitted is controlled by the O_2 oxidation rate. This is due to a higher OH concentration in the flame sheet which drops quickly in the post-flame region, which has higher O_2 concentrations.

The rate of soot oxidation by O_2 for the first moment is of the form,

$$R_{ox} = -C_{ox} k_{ox} [O_2] \alpha_{ox} A_s N \tag{4.2}$$

where C_{ox} is a constant, k_{ox} is the per-site rate coefficient for O_2 oxidation, $[O_2]$ is the oxygen concentration, α_{ox} is the fraction of surface sites available for oxidation, A_s is the surface site density of soot, and N is the number density of soot. It has been shown in the literature that the rates used in the ABF model tend to overpredict the effect of O_2 oxidation [130], and hence underpredict soot emissions. Since most models focus solely on predicting the in-flame temperature and soot volume fractions of non-smoking flames, this generally does not affect quantitative agreement with in-flame experimental data. However, predicting both in-flame soot volume fractions as well as emissions from a smoking flame is a very challenging test for a model, and has been achieved only a few times in literature [47,48]. Khosousi et al. [47] propose an O_2 oxidation model based on the thermal age of soot particles, which is a function of the time-temperature history of soot particles traveling thorough the flame. They show evidence for their claim that no constant value of the parameter α_{ox} can

predict soot in both smoking and non-smoking flames. In addition, a sensitivity analysis performed on laminar diffusion flames in the same study by Khosousi, et al. revealed that changing the rate of oxidation by O_2 molecules changes the mass of soot emission while only marginally affecting the peak in-flame soot volume fraction, while changing the oxidation rate by OH radicals only significantly affects the peak in-flame volume fraction. As soot particles go through the flame front and are exposed to higher temperatures, they age thermally, which reduces the number of active sites available for soot oxidation [34]. Khosousi et al. define the thermal age of a particle, given by the integral of the temperature the particle experiences over its residence time in the flame

$$T_a = \int T dt \tag{4.3}$$

where T_a is the thermal age, T is the temperature, and t is the time. This approach assumes the thermal age is linear in temperature, which is physically non-intuitive as most such processes proceed through an activation energy barrier. The literature approach represented by Equation 4.3 is adopted for this study. The present approach is similar to the procedure used by Veshkini, et al. [46]. Khosousi et al. calculate α_{ox} using the expression,

$$\alpha_{ox} = \left(\frac{T_{a,max}}{T_a}\right)^2 \exp\left(2\left(1 - \frac{T_{a,max}}{T_a}\right)\right) \tag{4.4}$$

where $T_{a,max}$ is the thermal age at the point of maximum soot of the flame, and T_a is the thermal age. The expression for α_{ox} is then used to calculate the in-flame soot volume fractions and soot emissions of several smoking and non-smoking laminar non-premixed

flames from literature. Their model captures both smoking and non-smoking behavior accurately in the flames studied.

A similar approach is used for calculating α_{ox} for each modeled flame. The soot field is first calculated using the expression for α_{ox} given by Appel et al.[34]. The injection of 5000 spherical carbon particles of diameter 60 nm into the domain through the fuel inlet is then modeled. The Lagrangian discrete phase model (DPM) is used to model the interaction of the particle phase with the gas phase. A one-way coupling between the gas phase and particle phase is assumed, i.e., the particles do not affect the flow in any way, but the flow affects the particles. The effect of turbulent dispersion on the particles is considered and a discrete random walk model is used to calculate the position of each particle in time. Using this model, the thermal age of every particle at each instant in time is calculated. From these data, a field function of mean thermal age and thermal age variance is calculated for each cell in the domain. An α_{ox} field function over the entire domain is calculated using the mean thermal age field and Equation 4.4. This α_{ox} is then used in the equations for O_2 oxidation in the method of moments soot model. The updated equations are solved to get the soot field. In order to gauge the sensitivity of the model to the parameter $T_{a,max}$, values of $T_{a,max}$ one standard deviation above and below the mean value for $T_{a,max}$ in addition to its mean value are also considered.

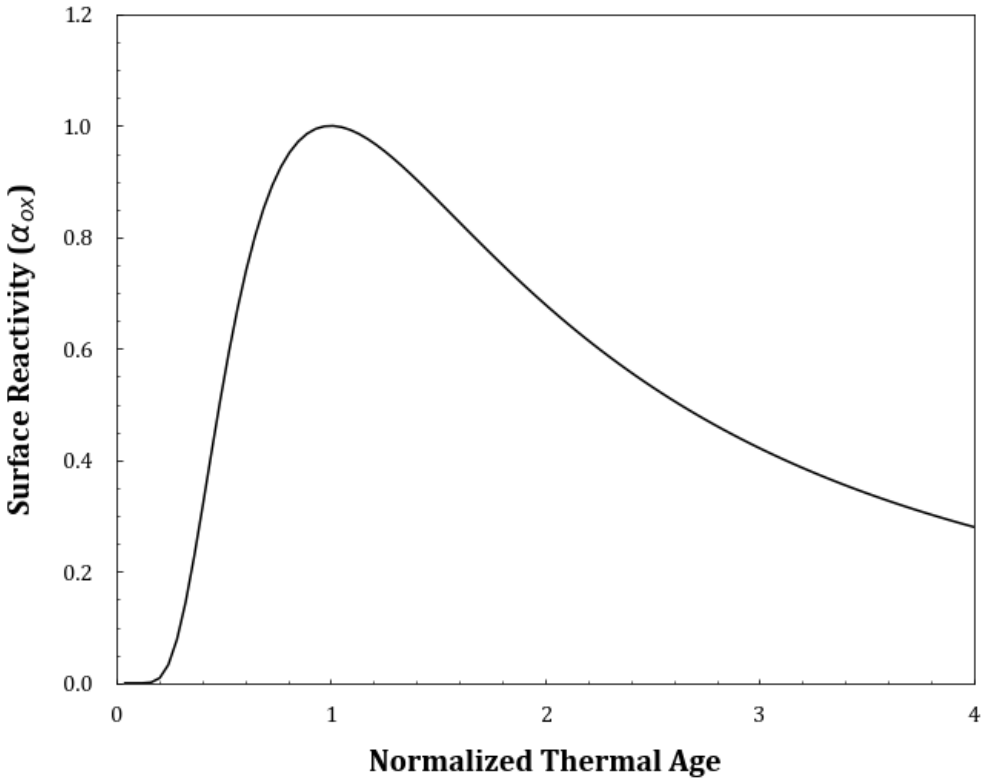

Figure 4.2: α_{ox} as a functional of normalized thermal age

Figure 4.2 shows a plot of α_{ox} as a function of thermal age normalized by $T_{a,max}$, given by Equation 4.4. An increasing, then decreasing trend in α_{ox} is observed as the thermal age increases. This effect has been attributed to competing factors in literature. The increase in α_{ox} is hypothesized to be due to the increase in active sites during the growth phase of the soot particle [131], while the subsequent decrease is thought to be due to carbonization of the soot particle as it is exposed to high temperature [132,133].

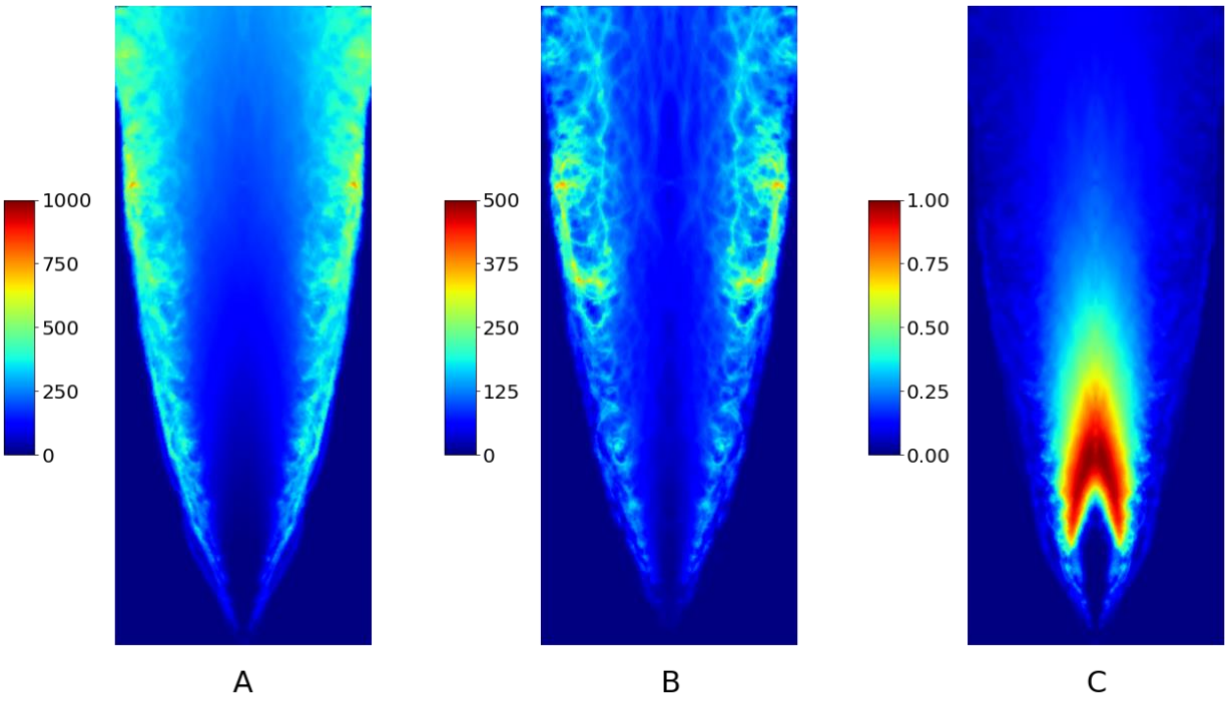

Figure 4.3: (A) Mean thermal age (Ks), (B) standard deviation of thermal age (Ks), and (C) mean alpha for the Flame M.

Figure 4.3(A), 4.3(B), and 4.3(C) show the calculated mean thermal age field, the thermal age variance and the α_{ox} for Flame M. As expected, the mean thermal age increases as we travel through the flame. The thermal age variance also increases as we go through the flame. The α_{ox} initially increases as we go through the flame, reaches a maximum at approximately 0.3 m above the nozzle, and then decreases as we go further downstream.

Radiation Model

We model radiation by solving the Radiative Transfer Equation (RTE) using the Discrete Ordinates Method, using the S_4 approximation [98]. We assume that the medium is gray, and that scattering is negligible. We calculate the absorption coefficient by an empirical relation given by Widmann [134],

$$\kappa_m = 2370 f_V T \tag{4.5}$$

where κ_m is the mean absorption coefficient, f_V is the soot volume fraction, and T is the temperature. The soot volume fraction is calculated from the first moment,

$$f_V = M_1 m_C \frac{\rho}{\rho_{soot}} \tag{4.6}$$

where M_1 is the first moment, m_C is the mass of one carbon atom, ρ is the overall density, and ρ_{soot} is the soot density, assumed to be 1800 kg/m3. The soot emission rate from the flame is calculated by integrating the soot volume fraction multiplied by the axial component of velocity over the outlet surface,

$$PM = \int_A \rho_{soot} f_V (\bar{u} \cdot \hat{n}) dA \tag{4.7}$$

where PM is the soot emission rate in kg/s, ρ_{soot} is the soot density, taken to be 1800 kg/m3, f_V is the soot volume fraction, $\bar{u}$ is the velocity in m/s, $\hat{n}$ is the unit vector in the axial direction, and A is the outlet surface.

4.2.3 Grid and Solver

All equations are solved by the finite volume method using the ANSYS Fluent commercial solver on structured grids, selected after carrying out grid independence studies. The grid is refined near the walls to accurately predict the boundary layer. The

SIMPLE numerical procedure for the pressure-velocity coupling, and all equations are solved using a second order upwind scheme.

4.3 Results and Discussion

4.3.1 In-flame Temperature and Soot Volume Fraction

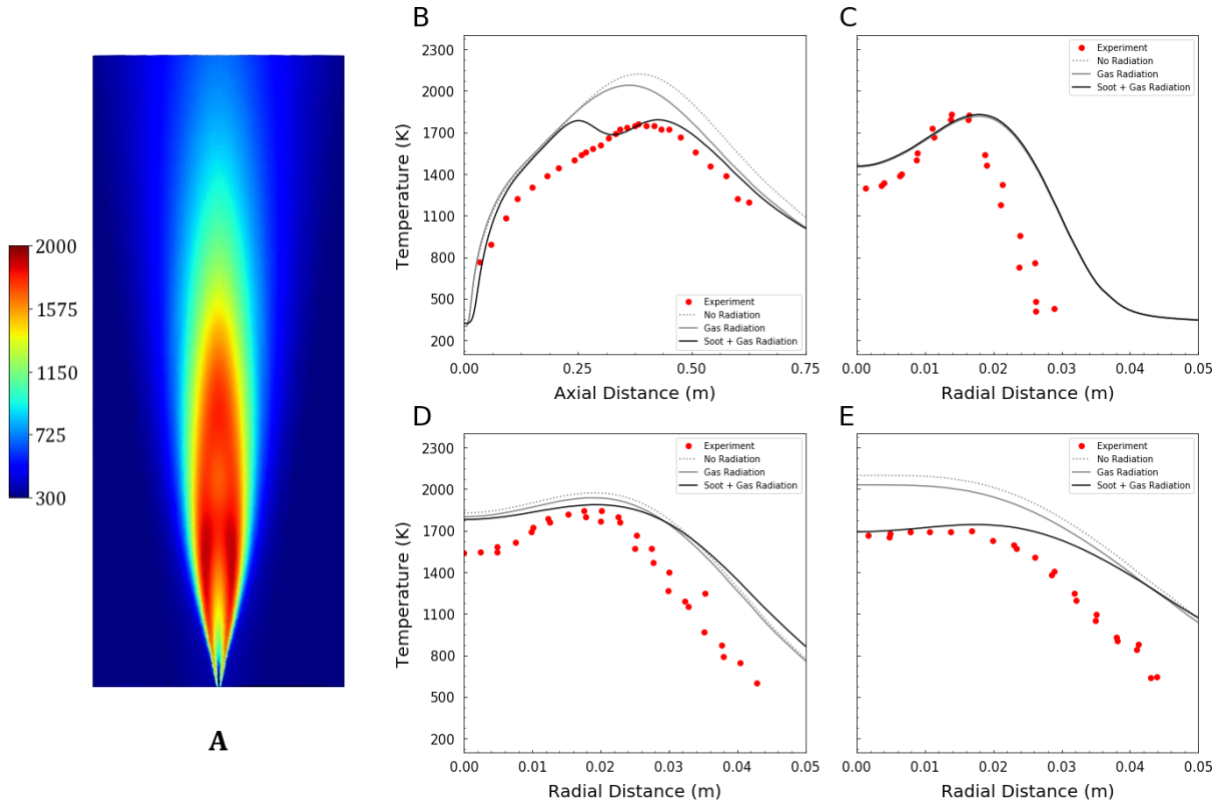

Figure 4.4: Measured temperature data for Flame A from ref [52] (Flame M in this work). (A) Predicted temperature distribution in Kelvin. Measured (red markers), predicted with no radiation (gray dotted line), predicted with gas radiation (gray line), and predicted with gas and soot radiation (black line) (B) axial temperature profile, (C) radial temperature profile at a distance of 138 mm from nozzle, (D) radial temperature profile at a distance of 241 mm from nozzle, (E) radial temperature profile at a distance of 345 mm from nozzle.

Figure 4.4(A) shows the calculated mean temperature distribution of Flame M. The highest temperature seen is 1908 K, at an off-axial position. Figure 4.4(A) to 4.4(E) show the comparison of measured temperatures taken from Kent and Honnery [52] for their Flame A and temperatures predicted by the CFD model without considering radiation (dotted gray

line), considering only gas radiation (solid gray line), and considering soot and gas radiation (black line). Figure 4.4(B) shows the measured and predicted axial temperature along the centerline of the flame. The graph shows that including the effect of gas and soot radiation causes the predicted temperatures to drop. We observe that the model predictions including gas and soot radiation closely match the experimental data for an axial distance greater than 0.28 m, but overpredict the temperature for axial distances below 0.28 m. We attribute this overprediction to underprediction of the soot volume fraction (Figure 4.5(B)), which leads to a reduction in radiated energy and hence, increased temperatures. Figure 4.4(C), 4.4(D), and 4.4(E) show the measured and predicted radial temperature distributions at a distance of 138 mm, 241.5 mm, and 345 mm from the nozzle. The temperature profile at a distance of 138 mm from the nozzle, shown in Figure 4.4(C), is not greatly affected by the inclusion of soot and gas radiation. This is because not much soot is formed at that distance, and hence the temperature profile is not affected to a large extent. All predicted temperature profiles match the trends of measured temperature profiles.

Figure 4.5(A) to 4.5(D) show the comparison of the measured and predicted soot profiles taken from Kent and Honnery [52] for their Flame A, with black lines representing the predictions and red dots representing experimental data. The axial soot profile seen in Figure 4.5(A) matches experimental data at axial distances of 241.5 mm and 345 mm, but underpredicts the soot volume fraction at axial distances of 138 mm and 483 mm. From Figure 4.5 (B), 3.5(C) and 3.5(D), we observe that the model underpredicts the radial soot volume fraction at an axial distance of 138 mm, but matches the experimental trend for axial distances of 241.5 mm and 345 mm.

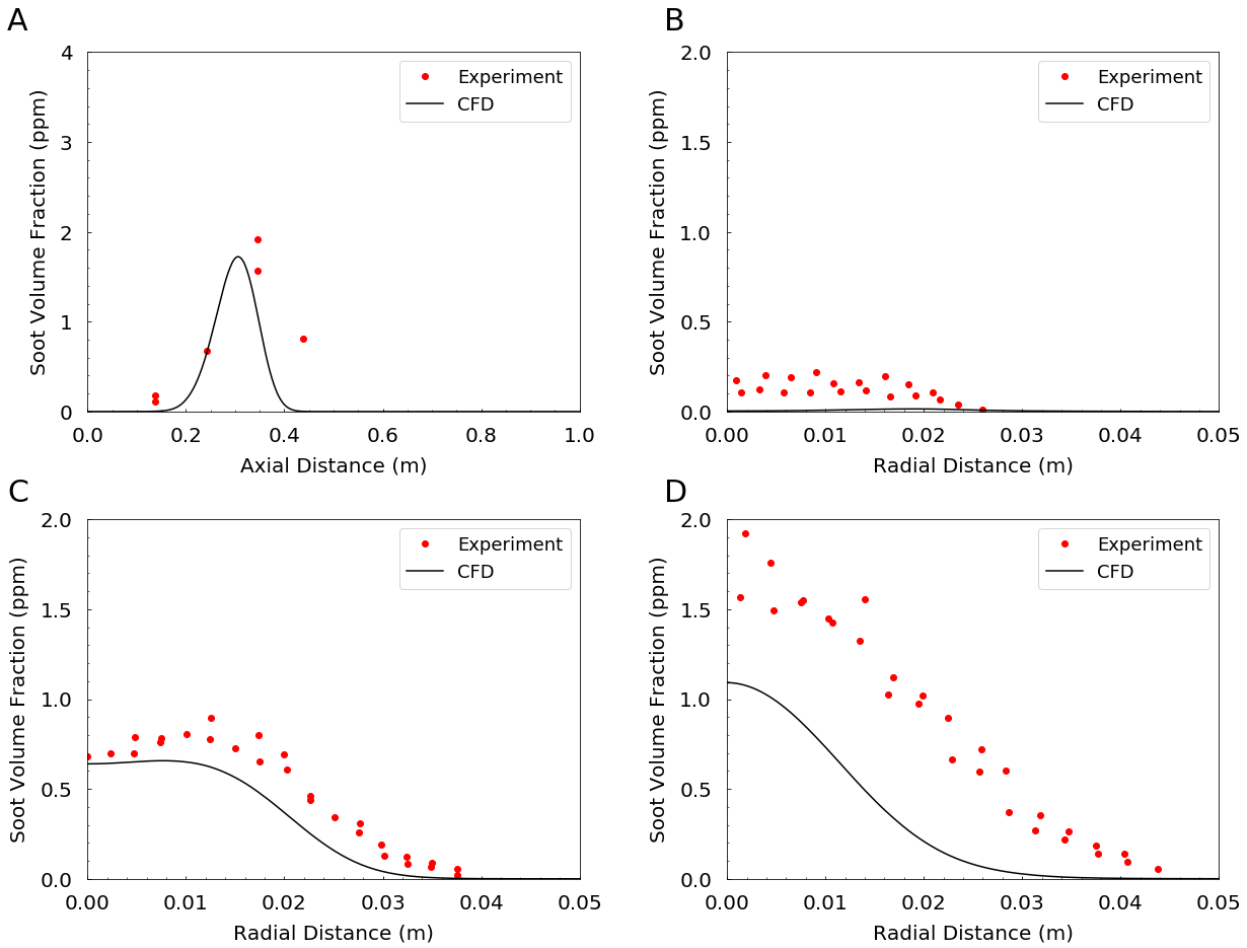

Figure 4.5: Predicted (black line) and measured (red markers) in-flame soot volume fractions for Flame A in ref [52] (Flame M in this work). (A) Axial soot volume fraction, (B) Radial soot volume fraction at a distance of 138 mm from the nozzle, (C) Radial soot volume fraction at a distance of 241 mm from the nozzle, (D) Radial soot volume fraction at a distance of 345 mm from the nozzle.

Figure 4.6(A) shows the predicted mean temperature distribution of a representative non-premixed turbulent ethylene flame, Flame G. The highest temperature in the flame without the pot is 1979 K and is seen on the axis at a distance of 285 mm from the nozzle. Figure 4.6(B) shows the predicted temperature distribution of Flame G with the flame obstructed by a pot maintained at a temperature of 373 K placed at 245 mm from the nozzle. The presence of the pot disrupts the flame. The maximum temperature observed is 1925 K, seen at an off-axial location at approximately 163 mm above the jet nozzle.

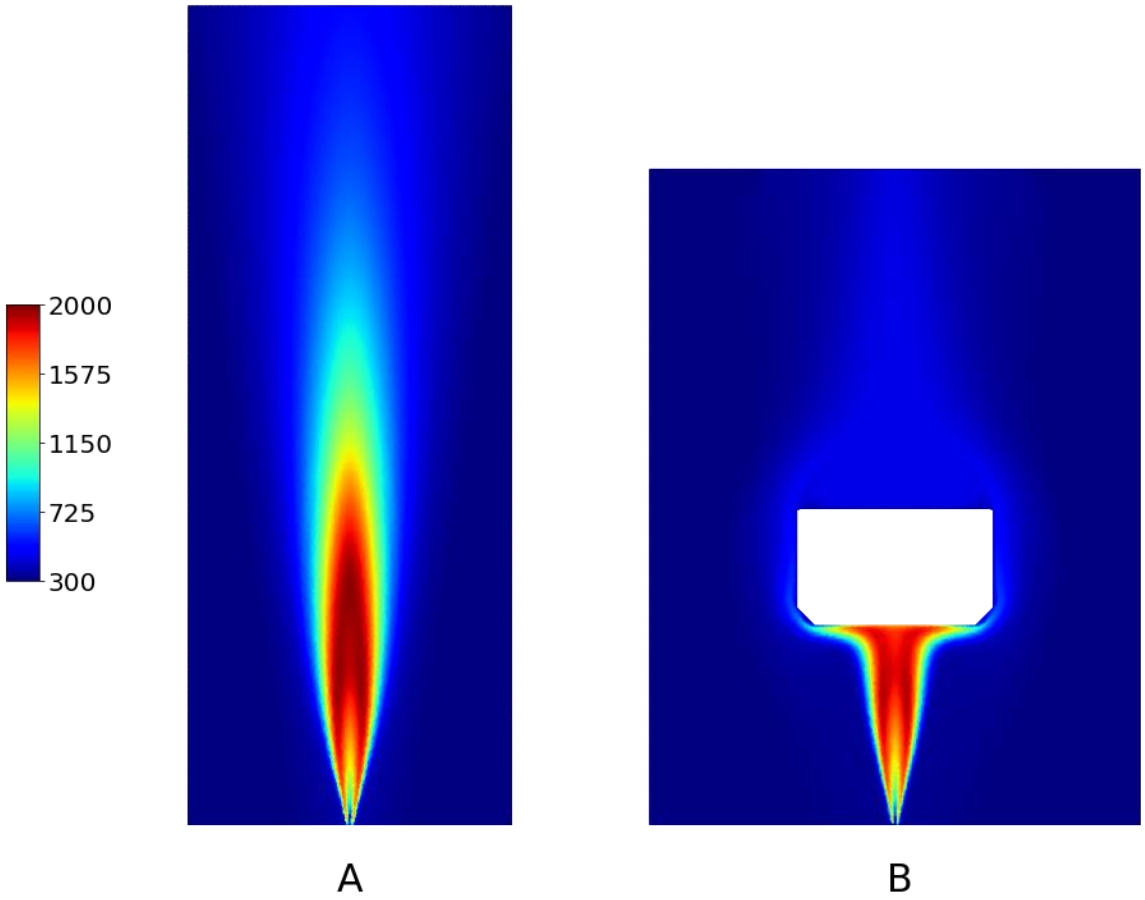

Figure 4.6: (A) Mean predicted temperature distribution in Kelvin for Flame G, (B) mean predicted temperature distribution in Kelvin for Flame G with a pot placed 245 mm from the nozzle.

4.3.2 Soot Mass Emissions from Flames Impinging on a Cold Surface

The model is now used to predict the soot emissions when the position of the pot with respect to the jet nozzle changes. Figure 4.7 shows a plot of the measured and predicted soot emissions from Flame G as a function of pot height. The pot height is varied from 150 mm to 400 mm in the experiment. Three predicted curves are shown in Figure 4.7, each with a different value of the parameter $T_{a,max}$ in the updated soot model; the solid black line shows the results with the mean value, the dotted black line shows results with the value one standard deviation above the mean, and the dashed black line shows results with the value

one standard deviation below the mean. $T_{a,max}$ is the calculated thermal age at the point of maximum soot in the model. Since the flow is turbulent, the value of this parameter is not a constant, but varies with time and has a variance associated with it. Hence, the sensitivity of the model to this parameter is also analyzed. All three models correctly predict the trend of increasing, then decreasing soot emissions, with the maximum soot emission observed at 245 mm, which agrees with experimental data. However, while the trend is predicted correctly, soot emission is underpredicted for pot heights lower than 150 mm and higher than 350 mm. The likely reasons for the underprediction are explored later in this section. In addition, the results are observed to be very sensitive to the value of $T_{a,max}$. with the soot mass emission being inversely related to the value of $T_{a,max}$, i.e., an increase in $T_{a,max}$ results in decreased soot emission. This indicates that the effect of turbulence on the model needs to be captured, possibly by methods similar to those used for predicting NOx chemistry, such as presumed PDF methods.

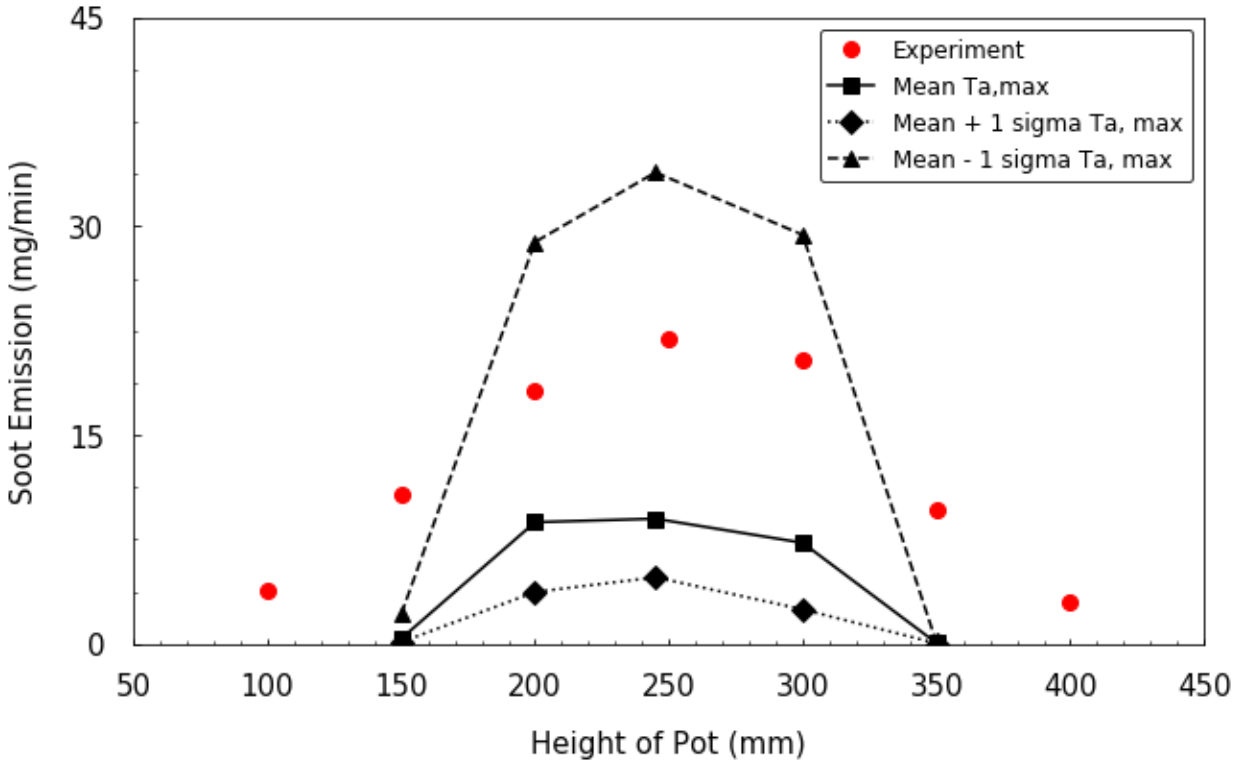

Figure 4.7: Plot of the measured and predicted soot emissions as a function of the pot height for Flame G. The red circular markers represent experimental data. The black line with square markers represents predictions made using the mean value of $T_{a,max}$, while the lines with the triangular and diamond markers represent predictions made with values one standard deviation below and above mean $T_{a,max}$, respectively.

In order to understand why soot mass emission increases when a pot is placed in the flame, the environment experienced by soot particles in Flame M without a pot, and with a pot placed 245 mm above the nozzle is considered. The source terms for oxidation and surface growth for the first moment along pathlines exhibiting maximum soot for each configuration is shown in Figure 4.8(A) and 4.8(B), respectively. For both particles in each configuration, the source terms become negligible beyond a residence time of about 30 ms. The source terms for both particles for each configuration are observed to be similar until a residence time of approximately 7 ms. Figure 4.8(A) shows that the surface growth reaches a maximum for both configurations at about the same residence time but falls much quicker when there is no pot. Figure 4.8(B) shows that the oxidation term attains a higher peak value

when no pot is present, i.e., the absence of the pot results in more oxidation. Speculatively, this decrease in oxidation could be due to effect of thermal quenching because of the presence of the cold surface, or due to the re-laminarization of flow in the boundary layer near the cold surface. This increase in the surface growth and reduction in the oxidation due to the presence of the pot causes the increased soot emissions seen in Figure 4.7.

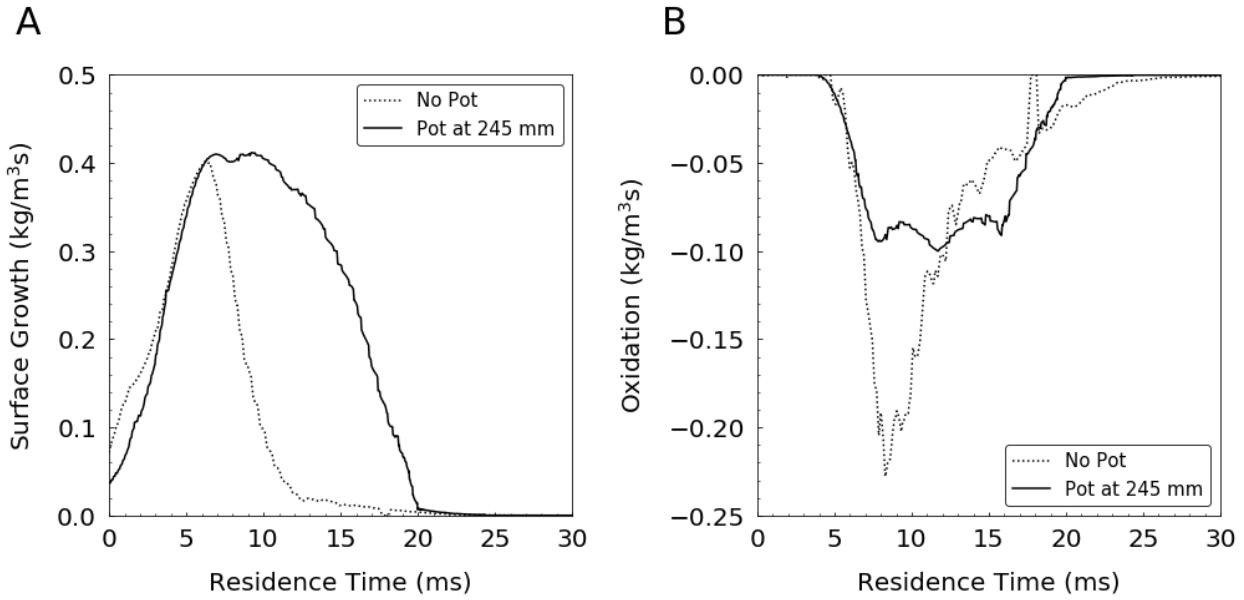

Figure 4.8: (A) Source term for surface growth along the pathline exhibiting maximum soot as a function of residence time for Flame G. The solid line represents the source term for the flame with a pot placed at a height of 245 mm and the dotted line represents the source term for the free flame. (B) Source term for oxidation along the pathline exhibiting maximum soot as a function of residence time. The solid line represents the source term for the flame with a pot placed at a height of 245 mm and the dotted line represents the source term for the free flame.

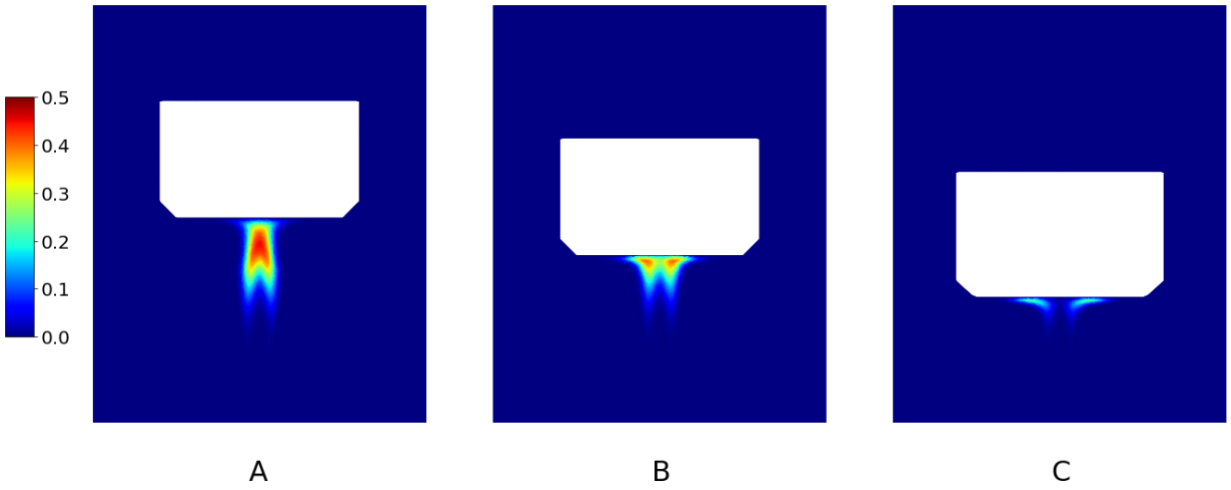

Figure 4.9: Predicted surface growth term in kg/(m^{3}s) for Flame G with (A) pot placed at 245 mm, (B) pot placed at 200 mm, (C) pot placed at 150 mm.

The trend of increasing, then decreasing soot emission is explored by analyzing soot surface growth terms for Flame G. Figure 4.9(A), 4.9(B) and 4.9(C) show the surface growth term for the first moment in kg/(m^{3}s) with the pot placed at a distance of 245 mm, 200 mm, and 150 mm, respectively. The measured soot emission for each of these configurations is 22 mg/min, 18 mg/min and 11 mg/min, respectively. The figures show that moving the surface closer to the nozzle brings it into the surface growth zone of the flame, hence inhibiting the process to different degrees. Surface growth remains relatively unaffected for a pot height of 245 mm, shown in Figure 4.9(A), but is reduced as the pot moves down, shown in Figure 4.9(B) and 4.9(C). Volume integrals of the surface growth term across the entire domain also reveal reduced surface growth with reducing surface height. The cause for this appears to be reduced acetylene formation due to the presence of the cold surface. This is possibly because of the reduced temperature which occurs due to heat loss to the cold surface.

4.4 Summary

The development of and results from an axisymmetric CFD model for the prediction of in-flame soot volume fractions and soot mass emissions were presented in this chapter. Combustion was modeled using the non-premixed non-adiabatic flamelet method and soot using the Method of Moments with Interpolative Closure (MOMIC). The oxidation model developed by Khousousi et al.[47] based on thermal age of soot particles was used. Flames G and M (details in Chapter 3) were modeled, along with the impingement of Flame G on a pot maintained at 373 K placed at several distances from the jet nozzle.

The model's predictions were compared with in-flame soot and temperature data from literature. In-flame temperature measurements were predicted well by the model, but it was found that the model underpredicted soot volume fractions close to the nozzle, possibly due to the nucleation model not capturing nucleation behavior accurately. The model was then used to simulate Flame G with a pot maintained at 373 K placed at distances of 150 mm, 200 mm, 245 mm, 300 mm and 350 mm. The model correctly predicted the increasing, then decreasing trends of soot emission, but underpredicted overall soot emission, especially so at pot heights of 150 mm and 350 mm. The model was also found to be sensitive to the parameter $T_{a,max}$, the value of the thermal age at the point of maximum soot volume fraction.

Source terms for oxidation and surface growth for the first moment along the pathline exhibiting maximum soot were analyzed for Flame G with a pot present at 245 mm from the jet nozzle, and with the pot absent. The source terms for both configurations were negligible beyond a residence time of 30 ms. The surface growth term for both configurations reaches a maximum at approximately the same residence time but falls much quicker for the free

flame. The oxidation term for the free flame reaches a higher peak value, and the absence of the pot results in greater oxidation. These effects of greater soot surface growth and reduced soot oxidation lead to increased soot emission when a pot is present as opposed to a free flame. The increasing, then decreasing trend of soot emission with increasing pot height is investigated by analyzing the soot surface growth term for Flame G. Lowering the surface causes surface growth to be disrupted. The surface growth term increases as the surface height increases, leading to greater soot production and emission.

Chapter 5 : Summary and Conclusions

This work examines combustion, heat transfer and fluid mechanics in natural-draft, biomass-burning rocket cookstoves, and soot formation in a closely related configuration, a turbulent non-premixed ethylene flame impinging on a cold surface. Experimental data on cookstove temperatures, airflow rates and efficiencies are collected, and computational models are developed to investigate the effect of geometric and operating parameters on these quantities. Experimental data is also collected on soot emission from turbulent non-premixed ethylene flames, and models are developed to understand and predict soot emissions from a configuration closely related to cookstoves, a turbulent non-premixed flame impinging on a pot. By studying this more generic configuration, the goal is to develop generalizable results and methodologies for understanding and predicting soot emissions from biomass-burning cookstoves.

5.1 Combustion, Heat Transfer and Fluid Mechanics in Biomass-Burning Rocket Cookstoves

In order to gain insight on enhancing heat transfer to the cookpot and promoting mixing within the cookstove, CFD models are developed and simulations carried out for various configurations and operational parameters. Two CFD models are developed; a two-dimensional axisymmetric model with detailed combustion chemistry and a three-dimensional model with global chemistry. In addition, experimental data in the form of temperature measurements and airflows rates as a function of firepower calculated through the measurement of CO_2 are also collected. While soot is not modeled, the measured temperature profiles are used to calibrate a spatially averaged absorption coefficient to account for the heat transfer due to the presence of soot. The axisymmetric model is found to accurately predict the excess air through the cookstove, which is shown to be many times stoichiometric for every configuration except the ones where flow is severely constricted. A general design goal is to reduce the excess air which acts as a diluent. This allows the design to achieve the highest possible bulk temperature inside the cookstove, which promotes heat transfer and high efficiency.

The axisymmetric model is then used to investigate the effect of various geometric parameters, such as the height of the pot supports, cone deck shape, secondary air entrainment, and central baffles of various sizes placed within the riser on the thermal efficiency, excess air and mixing in the cookstove. The pot support height is found to have a strong effect on the excess air ratio as well as the stove efficiency. Secondary air entrainment by itself is found to be ineffective in increasing the mixing or heat transfer efficiency in the cookstove. However, secondary air entrainment used in conjunction with a central baffle,

leads to a decrease in the total airflow rate and an increase in turbulent mixing downstream of the baffle, and hence, better mixing which may reduce $PM_{2.5}$ emissions. The central baffle, however, is found to adversely affect the thermal efficiency due to increased heat loss to the metal surrounding the flow path. The shape of the cone deck is shown to affect the thermal efficiency primarily by impacting the airflow rate through the cookstove, which is investigated by modeling 36 different cone-deck configurations. A reduction in airflow causes the bulk temperature to increase, which leads to an increase in thermal efficiency. Three cone-decks were manufactured based on these findings. These were tested and the thermal efficiency measurements agreed well with the thermal efficiencies predicted by the model. While a constrictive cone-deck and a centrally placed baffle both lead to decreased airflow through the cookstove due to similar pressure reductions, the effects on the thermal efficiency are found to be different. The baffle leads to better mixing and hence, greater heat transfer to the walls, resulting in reduced thermal efficiency with increasing pressure drop, whereas constricting the air flow by changing the cone-deck shape leads to increased thermal efficiency with increased pressure drop. Therefore, a similar air mass flow rate for various configurations can result in different stove thermal efficiencies. This suggests that care should be taken when reducing excess air flow in the stove to avoid increasing heat transfer to the stove body or the environment.

The effect of various geometric and operational parameters on cookstove performance was thus explored. In addition to developing an understanding of the underlying physics of stove performance, these results also show that CFD is a valuable tool that can be used to guide the design of energy efficient natural draft, biomass-burning cookstoves.

5.2 Experimental Analysis of Soot Emissions from Turbulent Non-Premixed Ethylene Flames

Soot emissions from seventeen vertically oriented turbulent flames are investigated experimentally. The data obtained include soot mass emission measured by a Tapered Element Oscillating Microbalance and particle size distributions measured using a Scanning Mobility Particle Sizer.

Soot yield factors and mean particle diameters from free flames are found to be strongly correlated with the Richardson's ratio, as well as the jet exit strain rate. A possible explanation for the dependence on strain rate is that soot inception and growth by PAHs is inhibited at high scalar dissipation rates, resulting in reduced soot yields at higher mixing rates. The mean diameter and soot yield factor also stabilize for flames with $Ri_L < 100$, i.e., when the flames are momentum driven.

The soot yield factor for a flame impinging on the cold surface at any height is found to be greater than the soot yield factor of that flame without an obstruction in it. The χ_S for a particular flame increases and then decreases with the non-dimensional flame height h*. The point of inflection is found to be h* = 0.46, averaged across all experimental data. A likely explanation is that the presence of the cold surface quenches soot oxidation, resulting in increased soot emission. However, if the surface is placed closer to the jet, nucleation of new soot particles could be inhibited, resulting in the trend of χ_S with h*. Another possible explanation is that C_2H_2 production is inhibited by the cold surface, leading to reduced surface growth. The particle size distribution of emitted soot is found to be bimodal for nearly all flames impinging on the cold surface, with the smaller mode between 20 – 30 nm

and the larger mode at ~115 nm. The number of particles per kg fuel carbon in the smaller mode does not appear to change for any configuration studied.

5.3 CFD Modeling of Soot Emissions from Turbulent Non-Premixed Flames

A CFD model for predicting in-flame soot volume fractions and soot mass emissions is developed. Combustion is modeled using the non-premixed non-adiabatic flamelet method, and soot using the Method of Moments with Interpolative Closure (MOMIC). The chemical kinetic mechanism developed by Blanquart et al., is chosen to model combustion and PAH chemistry. Soot nucleation is modeled by assuming that the collision of two pyrene molecules results in a nucleated soot particle. Soot surface growth is modeled by the HACA mechanism, and soot growth by PAH condensation is neglected. Coagulation in three different regimes, (continuum, free-molecular, and transitional) is modeled. Oxidation by both OH radicals and O_2 molecules is modeled. Oxidation by OH is modeled assuming a reaction probability suggested by Neoh et al, and the model developed by Khousousi et al. based on thermal age of soot particles is used for predicting soot oxidation by O_2 molecules. Two flames are modeled, along with the impingement of one of the flames on a pot maintained at 373 K placed at several axial locations from the jet nozzle.

The model's predictions are compared with in-flame soot and temperature data from literature, and the model is used to explain phenomena obtained from experiment. The model predicts in-flame temperatures well but underpredicts soot volume fractions near the nozzle. This is thought to be due to fewer particles predicted to be formed from PAHs by the nucleation model. The model correctly predicts the trend of increasing, then decreasing soot mass emissions from Flame G impinging on a pot, but consistently underpredicts soot mass

emissions, especially so when the pot is in the nucleation zone, as well as when the pot is placed in the overfire region. The model is also found to be sensitive to the parameter $T_{a,max}$, the value of the thermal age at the point of maximum soot volume fraction.

Source terms for oxidation and surface growth for the first moment along the pathline exhibiting maximum soot are analyzed for Flame G with a pot present at 245 mm from the jet nozzle, and with the pot absent. The source terms for both configurations are negligible beyond a residence time of 30 ms. The surface growth term for both configurations reaches a maximum at approximately the same residence time but falls much quicker for the free flame. The oxidation term for the free flame reaches a higher peak value, and the absence of the pot results in greater oxidation. These effects of greater soot surface growth and reduced soot oxidation lead to increased soot emission when a pot is present as opposed to a free flame. The increasing, then decreasing trend of soot emission with increasing pot height is investigated by analyzing the soot surface growth term for Flame G. Lowering the surface causes surface growth to be disrupted. The surface growth term increases as the surface height increases, leading to greater soot production and emission.

5.4 Future Work

In this work, the Method of Moments with Interpolative Closure (MOMIC) was used to model soot. Since the model deals only with moments of the size distribution, it cannot be used to predict particle size distributions of emitted soot. Therefore, a possible direction for future work is using models that capture a more complete picture of the particle size distribution, such as mono- or bi-variate sectional methods, to investigate the particle size distribution data presented in Chapter 3.

Predicting soot oxidation accurately remains a challenging and open problem and is one of the most complex and uncertain processes in the numerical modeling of soot. The oxidation model used in this work assumes a linear dependence of thermal age on temperature. This is quite counter-intuitive, since chemical reactions and processes are, generally speaking, exponentially dependent on temperature. In addition, the model has been developed with some unjustified assumptions, such as the relationship between α_{ox} and thermal age. Another possible future research direction is the development of an oxidation model from first principles.

Finally, the goal of this work is to understand the process of soot formation and emission in biomass-burning cookstoves, such that soot mass emissions and the size distribution of emitted soot can be predicted and controlled. A third possible research direction is the development of a soot model for biomass-burning cookstoves, which could be used to investigate the processes of soot formation and destruction in cookstoves, supplementing the analysis done in Chapter 2 of this work.

Bibliography

[1] Bonjour, S., Adair-Rohani, H., Wolf, J., Bruce, N. G., Mehta, S., Prüss-Ustün, A., Lahiff, M., Rehfuess, E. A., Mishra, V., and Smith, K. R., 2013, "Solid Fuel Use for Household Cooking: Country and Regional Estimates for 1980–2010," Environ. Health Perspect., **121**(7), pp. 784–790.

[2] Saldiva, P. H. N., and Miraglia, S. G. E. K., 2004, "Health Effects of Cookstove Emissions," Energy Sustain. Dev., **8**(3), pp. 13–19.

[3] Bruce, N., Pope, D., Rehfuess, E., Balakrishnan, K., Adair-Rohani, H., and Dora, C., 2015, "WHO Indoor Air Quality Guidelines on Household Fuel Combustion: Strategy Implications of New Evidence on Interventions and Exposure–Risk Functions," Atmos. Environ., **106**, pp. 451–457.

[4] Bond, T. C., Doherty, S. J., Fahey, D. W., Forster, P. M., Berntsen, T., DeAngelo, B. J., Flanner, M. G., Ghan, S., Kärcher, B., Koch, D., Kinne, S., Kondo, Y., Quinn, P. K., Sarofim, M. C., Schultz, M. G., Schulz, M., Venkataraman, C., Zhang, H., Zhang, S., Bellouin, N., Guttikunda, S. K., Hopke, P. K., Jacobson, M. Z., Kaiser, J. W., Klimont, Z., Lohmann, U., Schwarz, J. P., Shindell, D., Storelvmo, T., Warren, S. G., and Zender, C. S., 2013, "Bounding the Role of Black Carbon in the Climate System: A Scientific Assessment," J. Geophys. Res. Atmospheres, **118**(11), pp. 5380–5552.

[5] Ramanathan, V., and Carmichael, G., 2008, "Global and Regional Climate Changes Due to Black Carbon," Nat. Geosci., **1**(4), pp. 221–227.

[6] Tucker, M., 1999, "Can Solar Cooking Save the Forests?," Ecol. Econ., **31**(1), pp. 77–89.

[7] "Water Boiling Test Protocol, Version 4.2.3" [Online]. Available: http://cleancookstoves.org/technology-and-fuels/testing/protocols.html.

[8] Jetter, J., Zhao, Y., Smith, K. R., Khan, B., Yelverton, T., DeCarlo, P., and Hays, M. D., 2012, "Pollutant Emissions and Energy Efficiency under Controlled Conditions for Household Biomass Cookstoves and Implications for Metrics Useful in Setting International Test Standards," Environ. Sci. Technol., **46**(19), pp. 10827–10834.

[9] Roden, C. A., Bond, T. C., Conway, S., Osorto Pinel, A. B., MacCarty, N., and Still, D., 2009, "Laboratory and Field Investigations of Particulate and Carbon Monoxide Emissions from Traditional and Improved Cookstoves," Atmos. Environ., **43**(6), pp. 1170–1181.

[10] Smith, K. R., Dutta, K., Chengappa, C., Gusain, P. P. S., Masera, O., Berrueta, V., Edwards, R., Bailis, R., and Shields, K. N., 2007, "Monitoring and Evaluation of Improved Biomass Cookstove Programs for Indoor Air Quality and Stove Performance: Conclusions from the Household Energy and Health Project," Energy Sustain. Dev., **11**(2), pp. 5–18.

[11] Kshirsagar, M. P., and Kalamkar, V. R., 2014, "A Comprehensive Review on Biomass Cookstoves and a Systematic Approach for Modern Cookstove Design," Renew. Sustain. Energy Rev., **30**, pp. 580–603.

[12] Udesen, D. J., 2019, "The Optimization, Evaluation, and Design of a Side-Feed Wood-Burning Cookstove with Fan-Driven Secondary Air Injection.," University of Washington.

[13] MacCarty, N. a., and Bryden, K. M., 2015, "Modeling of Household Biomass Cookstoves: A Review," Energy Sustain. Dev., **26**, pp. 1–13.

[14] Baldwin, S. F., 1987, *Biomass Stoves: Engineering Design, Development, and Dissemination*, Volunteers in Technical Assistance ; Center for Energy and Environmental Studies, Princeton University, Arlington, Va., USA : Princeton, N.J., USA.

[15] Agenbroad, J., DeFoort, M., Kirkpatrick, A., and Kreutzer, C., 2011, "A Simplified Model for Understanding Natural Convection Driven Biomass Cooking Stoves-Part 1: Setup and Baseline Validation," Energy Sustain. Dev., **15**(2), pp. 160–168.

[16] Agenbroad, J., DeFoort, M., Kirkpatrick, A., and Kreutzer, C., 2011, "A Simplified Model for Understanding Natural Convection Driven Biomass Cooking Stoves—Part 2: With Cook Piece Operation and the Dimensionless Form," Energy Sustain. Dev., **15**(2), pp. 169–175.

[17] Burnham-Slipper, H., 2009, "Breeding a Better Stove: The Use of Computational Fluid Dynamics and Genetic Algorithms to Optimise a Wood Burning Stove for Eritrea," University of Nottingham.

[18] Wohlgemuth, A., Mazumder, S., and Andreatta, D., 2009, "Computational Heat Transfer Analysis of the Effect of Skirts on the Performance of Third-World Cookstoves," J. Therm. Sci. Eng. Appl., **1**(4), p. 041001.

[19] Bryden, K. M., Ashlock, D. a., McCorkle, D. S., and Urban, G. L., 2003, "Optimization of Heat Transfer Utilizing Graph Based Evolutionary Algorithms," Int. J. Heat Fluid Flow, **24**(2), pp. 267–277.

[20] Miller-Lionberg, D. D., 2011, "A Fine Resolution CFD Simulation Approach for Biomass Cook Stove Development," Colorado State University.

[21] Frenklach, M., 2002, "Reaction Mechanism of Soot Formation in Flames," Phys. Chem. Chem. Phys., **4**(11), pp. 2028–2037.

[22] Frenklach, M., Clary, D. W., Gardiner, W. C., and Stein, S. E., 1985, "Detailed Kinetic Modeling of Soot Formation in Shock-Tube Pyrolysis of Acetylene," Symp. Int. Combust., **20**(1), pp. 887–901.

[23] Miller, J. A., and Melius, C. F., 1992, "Kinetic and Thermodynamic Issues in the Formation of Aromatic Compounds in Flames of Aliphatic Fuels," Combust. Flame, **91**(1), pp. 21–39.

[24] Kern, R. D., and Xie, K., 1991, "Shock Tube Studies of Gas Phase Reactions Preceding the Soot Formation Process," Prog. Energy Combust. Sci., **17**(3), pp. 191–210.

[25] Melius, C. F., Colvin, M. E., Marinov, N. M., Pit, W. J., and Senkan, S. M., 1996, "Reaction Mechanisms in Aromatic Hydrocarbon Formation Involving the C5H5 Cyclopentadienyl Moiety," Symp. Int. Combust., **26**(1), pp. 685–692.

[26] Griesheimer, J., and Homann, K.-H., 1998, "Large Molecules, Radicals Ions, and Small Soot Particles in Fuel-Rich Hydrocarbon Flames," Symp. Int. Combust., **27**(2), pp. 1753–1759.

[27] Frenklach, M., and Wang, H., 1991, "Detailed Modeling of Soot Particle Nucleation and Growth," Symp. Int. Combust., **23**(1), pp. 1559–1566.

[28] Böhm, H., and Jander, H., 1999, "PAH Formation in Acetylene – Benzene Pyrolysis," Phys. Chem. Chem. Phys., **1**, pp. 3775–3781.

[29] Castaldi, M. J., Marinov, N. M., Melius, C. F., Huang, J., Senkan, S. M., Pit, W. J., and Westbrook, C. K., 1996, "Experimental and Modeling Investigation of Aromatic and Polycyclic Aromatic Hydrocarbon Formation in a Premixed Ethylene Flame," Symp. Int. Combust., **26**(1), pp. 693–702.

[30] Richter, H., and Howard, J. B., 2000, *Formation of Polycyclic Aromatic Hydrocarbons and Their Growth to Soot - a Review of Chemical Reaction Pathways*.

[31] Slavinskaya, N. A., Riedel, U., Dworkin, S. B., and Thomson, M. J., 2012, "Detailed Numerical Modeling of PAH Formation and Growth in Non-Premixed Ethylene and Ethane Flames," Combust. Flame, **159**(3), pp. 979–995.

[32] D'Anna, A., and Violi, A., 1998, "A Kinetic Model for the Formation of Aromatic Hydrocarbons in Premixed Laminar Flames," *Symposium (International) on Combustion*, Elsevier, pp. 425–433.

[33] Frenklach, M., and Wang, H., 1994, "Detailed Mechanism and Modeling of Soot Particle Formation," *Soot Formation in Combustion*, Springer Verlag.

[34] Appel, J., Bockhorn, H., and Frenklach, M., 2000, "Kinetic Modeling of Soot Formation with Detailed Chemistry and Physics: Laminar Premixed Flames of C2 Hydrocarbons," Combust. Flame, **121**(1–2), pp. 122–136.

[35] Wen, J. Z., Thomson, M. J., Park, S. H., Rogak, S. N., and Lightstone, M. F., 2005, "Study of Soot Growth in a Plug Flow Reactor Using a Moving Sectional Model," Proc. Combust. Inst., **30**(1), pp. 1477–1484.

[36] Zhao, B., Yang, Z., Johnston, M. V., Wang, H., Wexler, A. S., Balthasar, M., and Kraft, M., 2003, "Measurement and Numerical Simulation of Soot Particle Size Distribution Functions in a Laminar Premixed Ethylene-Oxygen-Argon Flame," Combust. Flame, **133**(1–2), pp. 173–188.

[37] Happold, J., Grotheer, H.-H., and Aigner, M., 2007, "Distinction of Gaseous Soot Precursor Molecules and Soot Precursor Particles through Photoionization Mass Spectrometry," Rapid Commun. Mass Spectrom., **21**(7), pp. 1247–1254.

[38] Sabbah, H., Biennier, L., Klippenstein, S. J., Sims, I. R., and Rowe, B. R., 2010, "Exploring the Role of PAHs in the Formation of Soot: Pyrene Dimerization," J. Phys. Chem. Lett., **1**(19), pp. 2962–2967.

[39] Puri, R., Richardson, T. F., Santoro, R. J., and Dobbins, R. A., 1993, "Aerosol Dynamic Processes of Soot Aggregates in a Laminar Ethene Diffusion Flame," Combust. Flame, **92**(3), pp. 320–333.

[40] Harris, S. J., and Weiner, A. M., 1985, "Chemical Kinetics of Soot Particle Growth," Annu. Rev. Phys. Chem., **36**(1), pp. 31–52.

[41] Sunderland, P. B., and Faeth, G. M., 1996, "Soot Formation in Hydrocarbon/Air Laminar Jet Diffusion Flames," Combust. Flame, **105**(1–2), pp. 132–146.

[42] Kennedy, I. M., 1997, "Models of Soot Formation and Oxidation," Prog. Energy Combust. Sci., **23**(2), pp. 95–132.

[43] Stanmore, B. R., Brilhac, J.-F., and Gilot, P., 2001, "The Oxidation of Soot: A Review of Experiments, Mechanisms and Models," Carbon, **39**(15), pp. 2247–2268.

[44] Nagle, J. R., and Strickland-Constable, R. F., 1964, "Oxidation of Carbon between 1000–2400 C," Carbon, **1**(3), pp. 333–338.

[45] Neoh, K. G., Howard, J. B., and Sarofim, A. F., 1985, "Effect of Oxidation on the Physical Structure of Soot," *Symposium (International) on Combustion*, Elsevier, pp. 951–957.

[46] Veshkini, A., Dworkin, S. B., and Thomson, M. J., 2014, "A Soot Particle Surface Reactivity Model Applied to a Wide Range of Laminar Ethylene/Air Flames," Combust. Flame, **161**(12), pp. 3191–3200.

[47] Khosousi, A., and Dworkin, S. B., 2015, "Detailed Modelling of Soot Oxidation by O 2 and OH in Laminar Diffusion Flames," Proc. Combust. Inst., **35**(2), pp. 1903–1910.

[48] Liu, F., Guo, H., Smallwood, G. J., and Gülder, ömer L., 2003, "Numerical Modelling of Soot Formation and Oxidation in Laminar Coflow Non-Smoking and Smoking Ethylene Diffusion Flames," Combust. Theory Model., **7**(2), pp. 301–315.

[49] Eaves, N. A., Veshkini, A., Riese, C., Zhang, Q., Dworkin, S. B., and Thomson, M. J., 2012, "A Numerical Study of High Pressure, Laminar, Sooting, Ethane–Air Coflow Diffusion Flames," Combust. Flame, **159**(10), pp. 3179–3190.

[50] Kazakov, A., Wang, H., and Frenklach, M., 1995, "Detailed Modeling of Soot Formation in Laminar Premixed Ethylene Flames at a Pressure of 10 Bar," Combust. Flame, **100**(1–2), pp. 111–120.

[51] Dobbins, R. A., Fletcher, R. A., and Chang, H.-C., 1998, "The Evolution of Soot Precursor Particles in a Diffusion Flame," Combust. Flame, **115**(3), pp. 285–298.

[52] Kent, J. H., and Honnery, D., 1987, "Soot and Mixture Fraction in Turbulent Diffusion Flames," Combust. Sci. Technol., **54**(1–6), pp. 383–398.

[53] Ni, T., Pinson, J. A., Gupta, S., and Santoro, R. J., 1995, "Two-Dimensional Imaging of Soot Volume Fraction by the Use of Laser-Induced Incandescence," Appl. Opt., **34**(30), p. 7083.

[54] Brookes, S., and Moss, J., 1999, "Predictions of Soot and Thermal Radiation Properties in Confined Turbulent Jet Diffusion Flames," Combust. Flame, **116**(4), pp. 486–503.

[55] Hu, B., Yang, B., and Koylu, U. O., 2003, "Soot Measurements at the Axis of an Ethylene/Air Non-Premixed Turbulent Jet Flame," Combust. Flame, **134**(1–2), pp. 93–106.

[56] Yang, B., and Koylu, U. O., 2005, "Detailed Soot Field in a Turbulent Non-Premixed Ethylene/Air Flame from Laser Scattering and Extinction Experiments," Combust. Flame, **141**(1–2), pp. 55–65.

[57] Qamar, N. H., Alwahabi, Z. T., Chan, Q. N., Nathan, G. J., Roekaerts, D., and King, K. D., 2009, "Soot Volume Fraction in a Piloted Turbulent Jet Non-Premixed Flame of Natural Gas," Combust. Flame, **156**(7), pp. 1339–1347.

[58] Lee, S.-Y., Turns, S. R., and Santoro, R. J., 2009, "Measurements of Soot, OH, and PAH Concentrations in Turbulent Ethylene/Air Jet Flames," Combust. Flame, **156**(12), pp. 2264–2275.

[59] Köhler, M., Geigle, K. P., Meier, W., Crosland, B. M., Thomson, K. A., and Smallwood, G. J., 2011, "Sooting Turbulent Jet Flame: Characterization and Quantitative Soot Measurements," Appl. Phys. B, **104**(2), pp. 409–425.

[60] Mahmoud, S. M., Nathan, G. J., Alwahabi, Z. T., Sun, Z. W., Medwell, P. R., and Dally, B. B., 2018, "The Effect of Exit Reynolds Number on Soot Volume Fraction in Turbulent Non-Premixed Jet Flames," Combust. Flame, **187**, pp. 42–51.

[61] Becker, H. A., and Liang, D., 1982, "Total Emission of Soot and Thermal Radiation by Free Turbulent Diffusion Flames," Combust. Flame, **44**(1–3), pp. 305–318.

[62] Becker, H. A., and Liang, D., 1983, "Soot Emission, Thermal Radiation, and Laminar Instability of Acetylene Diffusion Flames," Combust. Flame, **52**, pp. 247–256.

[63] Kent, J. H., and Bastin, S. J., 1984, "Parametric Effects on Sooting in Turbulent Acetylene Diffusion Flames," Combust. Flame, **56**(1), pp. 29–42.

[64] Delichatsios, M. A., 1993, "Smoke Yields from Turbulent Buoyant Jet Flames," Fire Saf. J., **20**(4), pp. 299–311.

[65] Santoro, R. J., Yeh, T. T., Horvath, J. J., and Semerjian, H. G., 1987, "The Transport and Growth of Soot Particles in Laminar Diffusion Flames," Combust. Sci. Technol., **53**(2–3), pp. 89–115.

[66] Wright, F. J., 1974, "Effect of Oxygen on the Carbon-Forming Tendencies of Diffusion Flames," Fuel, **53**(4).

[67] L Ellzey, J., Berbe, J. G., Tay, E. Z. F., and Foster, D. E., 1990, "Total Soot Yield from a Propane Diffusion Flame in Cross-Flow," Combust. Sci. Technol., **71**(1–3), pp. 41–52.

[68] Moss, J. B., Stewart, C. D., and Young, K. J., "Modeling Soot Formation and Burnout in a High Temperature Laminar Diffusion Flame Burning under Oxygen-Enriched Conditions," p. 10.

[69] Smooke, M., Long, M., Connelly, B., Colket, M., and Hall, R., 2005, "Soot Formation in Laminar Diffusion Flames," Combust. Flame, **143**(4), pp. 613–628.

[70] Flower, W. L., and Bowman, C. T., 1988, "Soot Production in Axisymmetric Laminar Diffusion Flames at Pressures from One to Ten Atmospheres," Symp. Int. Combust., **21**(1), pp. 1115–1124.

[71] Trouve, A., Cuenot, B., and Riber, E., 2012, "Numerical Modeling of the Deposition of Combustion-Generated Soot Particles on Cold Wall Surfaces," Cent. Turbul. Res. Proc. Summer Program.

[72] Makel, D. B., and Kennedy, I. M., 1991, "Experimental and Numerical Investigation of Soot Deposition in Laminar Stagnation Point Boundary Layers," Symp. Int. Combust., **23**(1), pp. 1551–1557.

[73] Smedley, J. M., Williams, A., and Hainsworth, D., 1995, "Soot and Carbon Deposition Mechanisms in Ethene/Air Flames," Fuel, **74**(12), pp. 1753–1761.

[74] Luo, M., Ying, Y., and Liu, D., 2018, "Soot in Flame-Wall Interactions: Views from Nanostructure and Reactivity," Fuel, **212**, pp. 117–131.

[75] Dong, L. L., Cheung, C. S., and Leung, C. W., 2013, "Characterization of Impingement Region from an Impinging Inverse Diffusion Flame Jet," Int. J. Heat Mass Transf., **56**(1–2), pp. 360–369.

[76] Saji, C. B., Balaji, C., and Sundararajan, T., 2008, "Investigation of Soot Transport and Radiative Heat Transfer in an Ethylene Jet Diffusion Flame," Int. J. Heat Mass Transf., **51**(17–18), pp. 4287–4299.

[77] Milson, A., and Chigier, N. A., 1973, "Studies of Methane and Methane-Air Flames Impinging on a Cold Plate," Combust. Flame, **21**(3), pp. 295–305.

[78] Li, H. B., Zhen, H. S., Leung, C. W., and Cheung, C. S., 2010, "Effects of Plate Temperature on Heat Transfer and Emissions of Impinging Flames," Int. J. Heat Mass Transf., **53**(19–20), pp. 4176–4184.

[79] Zhen, H. S., Cheung, C. S., and Leung, C. W., 2011, "Emission of Impinging Swirling and Non-Swirling Inverse Diffusion Flames," Appl. Energy, **88**(5), pp. 1629–1634.

[80] Mohr, J. W., Seyed-Yagoobi, J., and Page, R. H., "Combustion Measurements from an Impinging Radial Jet Reattachment Flame," Combust. Flame, **106**(1–2), pp. 69–80.

[81] Friedlander, S. K., 2000, *Smoke, Dust, and Haze*, Oxford University Press.

[82] Balthasar, M., and Kraft, M., 2003, "A Stochastic Approach to Calculate the Particle Size Distribution Function of Soot Particles in Laminar Premixed Flames," Combust. Flame, **133**(3), pp. 289–298.

[83] Celnik, M. S., Raj, A., Mosbach, S., West, R. H., and Kraft, M., 2009, "Multivariate Soot Particle Models," *Combustion Generated Fine Carbonaceous Particles*, KIT Scientific Publishing.

[84] Violi, A., Sarofim, A. F., and Voth, G. A., 2004, "Kinetic Monte Carlo–Molecular Dynamics Approach to Model Soot Inception," Combust. Sci. Technol., **176**(5–6), pp. 991–1005.

[85] Violi, A., Kubota, A., Truong, T. N., Pitz, W. J., Westbrook, C. K., and Sarofim, A. F., 2002, "A Fully Integrated Kinetic Monte Carlo/Molecular Dynamics Approach for the Simulation of Soot Precursor Growth," Proc. Combust. Inst., **29**(2), pp. 2343–2349.

[86] Mueller, M. E., Blanquart, G., and Pitsch, H., 2009, "A Joint Volume-Surface Model of Soot Aggregation with the Method of Moments," Proc. Combust. Inst., **32**(1), pp. 785–792.

[87] Mueller, M. E., Blanquart, G., and Pitsch, H., 2009, "Hybrid Method of Moments for Modeling Soot Formation and Growth," Combust. Flame, **156**(6), pp. 1143–1155.

[88] Smooke, M. D., McEnally, C. S., Pfefferle, L. D., Hall, R. J., and Colket, M. B., 1999, "Computational and Experimental Study of Soot Formation in a Coflow, Laminar Diffusion Flame," Combust. Flame, **117**(1–2), pp. 117–139.

[89] Richter, H., Granata, S., Green, W. H., and Howard, J. B., 2005, "Detailed Modeling of PAH and Soot Formation in a Laminar Premixed Benzene/Oxygen/Argon Low-Pressure Flame," Proc. Combust. Inst., **30**(1), pp. 1397–1405.

[90] Xiong, Y., and Pratsinis, S. E., 1993, "Formation of Agglomerate Particles by Coagulation and Sintering—Part I. A Two-Dimensional Solution of the Population Balance Equation," J. Aerosol Sci., **24**(3), pp. 283–300.

[91] McGraw, R., 1997, "Description of Aerosol Dynamics by the Quadrature Method of Moments," Aerosol Sci. Technol., **27**(2), pp. 255–265.

[92] Marchisio, D. L., and Fox, R. O., 2005, "Solution of Population Balance Equations Using the Direct Quadrature Method of Moments," J. Aerosol Sci., **36**(1), pp. 43–73.

[93] Wohlgemuth, A., Mazumder, S., and Andreatta, D., 2009, "Computational Heat Transfer Analysis of the Effect of Skirts on the Performance of Third-World Cookstoves," J. Therm. Sci. Eng. Appl., **1**(4), p. 041001.

[94] Shih, T.-H., Liou, W. W., Shabbir, A., Yang, Z., and Zhu, J., 1995, "A New K-ϵ Eddy Viscosity Model for High Reynolds Number Turbulent Flows," Comput. Fluids, **24**(3), pp. 227–238.

[95] Pope, S., 2001, *Turbulent Flows*, Cambridge University Press, New York.

[96] Glassman, I., and Yetter, R. A., 2008, *Combustion*, Academic Press.

[97] White, F. M., 2011, *Fluid Mechanics*, McGraw-Hill.

[98] Modest, M., 2003, *Radiative Heat Transfer*, Academic Press.

[99] Tominaga, Y., and Stathopoulos, T., 2007, "Turbulent Schmidt Numbers for CFD Analysis with Various Types of Flowfield," Atmos. Environ., **41**(37), pp. 8091–8099.

[100] Hawkes, E. R., Sankaran, R., Sutherland, J. C., and Chen, J. H., 2007, "Scalar Mixing in Direct Numerical Simulations of Temporally Evolving Plane Jet Flames with Skeletal CO/H2 Kinetics," Proc. Combust. Inst., **31**(1), pp. 1633–1640.

[101] Li, J., Zhao, Z., Kazakov, A., Chaos, M., Dryer, F. L., and Scire, J. J., 2007, "A Comprehensive Kinetic Mechanism for CO, CH2O, and CH3OH Combustion," Int. J. Chem. Kinet., **39**(3), pp. 109–136.

[102] Galgano, A., and di Blasi, C., 2006, "Coupling a CFD Code with a Solid-Phase Combustion Model," Prog. Comput. Fluid Dyn., **6**(4–5), pp. 287–302.

[103] Incropera, F. P., and DeWitt, D. P., 2002, *Fundamentals and Heat and Mass Transfer*, John Wiley and Sons.

[104] "STAR CCM+ User Manual," CD-Adapco [Online]. Available: https://thesteveportal.plm.automation.siemens.com.

[105] Spalding, D. B., 1977, "Development of the Eddy Breakup Model of Turbulent Combustion," **16**(1), p. 7.

[106] Galgano, A., Di Blasi, C., Horvat, A., and Sinai, Y., 2006, "Experimental Validation of a Coupled Solid- and Gas-Phase Model for Combustion and Gasification of Wood Logs," Energy Fuels, **20**(5), pp. 2223–2232.

[107] Yuen, W. W., and Tien, C. L., 1977, "A Simple Calculation Scheme for the Luminous-Flame Emissivity," *Symposium (International) on Combustion*, Elsevier, pp. 1481–1487.

[108] Sutar, K. B., Kohli, S., Ravi, M. R., and Ray, A., 2015, "Biomass Cookstoves: A Review of Technical Aspects," Renew. Sustain. Energy Rev., **41**, pp. 1128–1166.

[109] Rapp, V. H., Caubel, J. J., Wilson, D. L., and Gadgil, A. J., 2016, "Reducing Ultrafine Particle Emissions Using Air Injection in Wood-Burning Cookstoves," Environ. Sci. Technol., **50**(15), pp. 8368–8374.

[110] Still, Dean., Kness, Jim., and Aprovecho Research Center., 1996, *Capturing Heat : Five Earth-Friendly Cooking Technologies and How to Build Them*, Aprovecho Research Center, Cottage Grove, OR (80574 Hazelton Rd., Cottage Grove, OR 97424).

[111] Bryden, K. M., Still, D., Scott, P., Hoffa, G., Ogle, D., Balis, R., and Goyer, K., *Design Principles for Wood Burning Cookstoves*, Aprovecho Research Center.

[112] Newman, J. S., and Steciak, J., 1987, "Characterization of Particulates from Diffusion Flames," Combust. Flame, **67**(1), pp. 55–64.

[113] Chan, S. H., and He, Y. S., 1999, "Measurements of Particulate Mass Concentration Using a Tapered-Element Oscillating Microbalance and a Flame Ionization Detector," Meas. Sci. Technol., **10**(4), pp. 323–332.

[114] Burtscher, H., 2005, "Physical Characterization of Particulate Emissions from Diesel Engines: A Review," J. Aerosol Sci., **36**(7), pp. 896–932.

[115] Hauck, H., Berner, A., Gomiscek, B., Stopper, S., Puxbaum, H., Kundi, M., and Preining, O., 2004, "On the Equivalence of Gravimetric PM Data with TEOM and Beta-Attenuation Measurements," J. Aerosol Sci., **35**(9), pp. 1135–1149.

[116] Sullivan, B., Allawatt, G., Emery, A., Means, P., Kramlich, J., and Posner, J., 2017, "Time-Resolved Particulate Emissions Monitoring of Cookstove Biomass Combustion Using a Tapered Element Oscillating Microbalance," Combust. Sci. Technol., **189**(6), pp. 923–936.

[117] Zhao, B., Yang, Z., Li, Z., Johnston, M. V., and Wang, H., 2005, "Particle Size Distribution Function of Incipient Soot in Laminar Premixed Ethylene Flames: Effect of Flame Temperature," Proc. Combust. Inst., **30**(1), pp. 1441–1448.

[118] Maricq, M. M., Harris, S. J., and Szente, J. J., 2003, "Soot Size Distributions in Rich Premixed Ethylene Flames," Combust. Flame, **132**(3), pp. 328–342.

[119] Ouf, F.-X., Vendel, J., Coppalle, A., Weill, M., and Yon, J., 2008, "Characterization of Soot Particles in the Plumes of Over-Ventilated Diffusion Flames," Combust. Sci. Technol., **180**(4), pp. 674–698.

[120] Turns, S. R., 2000, *An Introduction to Combustion*, McGraw-Hill.

[121] Mahmoud, S. M., Nathan, G. J., Alwahabi, Z. T., Sun, Z. W., Medwell, P. R., and Dally, B. B., 2017, "The Effect of Exit Strain Rate on Soot Volume Fraction in Turbulent Non-Premixed Jet Flames," Proc. Combust. Inst., **36**(1), pp. 889–897.

[122] Bisetti, F., Blanquart, G., Mueller, M. E., and Pitsch, H., 2012, "On the Formation and Early Evolution of Soot in Turbulent Nonpremixed Flames," Combust. Flame, **159**(1), pp. 317–335.

[123] Lee, B. W., Jeong, J. I., Hwang, J. Y., Choi, M., and Chung, S. H., 2001, "Analysis of Growth of Non-Spherical Silica Particles in a Counterflow Diffusion Flame Considering Chemical Reactions, Coagulation and Coalescence," J. Aerosol Sci., **32**(2), pp. 165–185.

[124] Menter, F. R., Kuntz, M., and Langtry, R., 2003, "Ten Years of Industrial Experience with the SST Turbulence Model," Turbul. Heat Mass Transf., **4**(1), pp. 625–632.

[125] Stephan, K., and Laesecke, A., 1985, "The Thermal Conductivity of Fluid Air," J. Phys. Chem. Ref. Data, **14**(1), pp. 227–234.

[126] Blanquart, G., Pepiot-Desjardins, P., and Pitsch, H., 2009, "Chemical Mechanism for High Temperature Combustion of Engine Relevant Fuels with Emphasis on Soot Precursors," Combust. Flame, **156**(3), pp. 588–607.

[127] Narayanaswamy, K., Blanquart, G., and Pitsch, H., 2010, "A Consistent Chemical Mechanism for Oxidation of Substituted Aromatic Species," Combust. Flame, **157**(10), pp. 1879–1898.

[128] Blanquart Guillaume, 2015, "Effects of Spin Contamination on Estimating Bond Dissociation Energies of Polycyclic Aromatic Hydrocarbons," Int. J. Quantum Chem., **115**(12), pp. 796–801.

[129] Frenklach, M., 2002, "Method of Moments with Interpolative Closure," Chemical Engineering Science, **57**(12), pp. 2229–2239.

[130] Celnik, M. S., Sander, M., Raj, A., West, R. H., and Kraft, M., 2009, "Modelling Soot Formation in a Premixed Flame Using an Aromatic-Site Soot Model and an Improved Oxidation Rate," Proc. Combust. Inst., **32**(1), pp. 639–646.

[131] Blanquart, G., and Pitsch, H., 2009, "Analyzing the Effects of Temperature on Soot Formation with a Joint Volume-Surface-Hydrogen Model," Combust. Flame, **156**(8), pp. 1614–1626.

[132] Faccinetto, A., Desgroux, P., Ziskind, M., Therssen, E., and Focsa, C., 2011, "High-Sensitivity Detection of Polycyclic Aromatic Hydrocarbons Adsorbed onto Soot Particles Using Laser Desorption/Laser Ionization/Time-of-Flight Mass Spectrometry: An Approach to Studying the Soot Inception Process in Low-Pressure Flames," Combust. Flame, **158**(2), pp. 227–239.

[133] Whitesides, R., and Frenklach, M., 2010, "Detailed Kinetic Monte Carlo Simulations of Graphene-Edge Growth," J. Phys. Chem. A, **114**(2), pp. 689–703.

[134] Widmann, J. F., 2003, "Evaluation of the Planck Mean Absorption Coefficients for Radiation Transport through Smoke," Combust. Sci. Technol., **175**(12), pp. 2299–2308.

Appendix A: Cookstove Files

1. Cookstove Dimensions

The SFR 9, a natural draft rocket cookstove manufactured by BURN Design Labs, is used for gathering all data presented in Chapter 2. The dimensions of the cookstove are shown in Figure A.1.

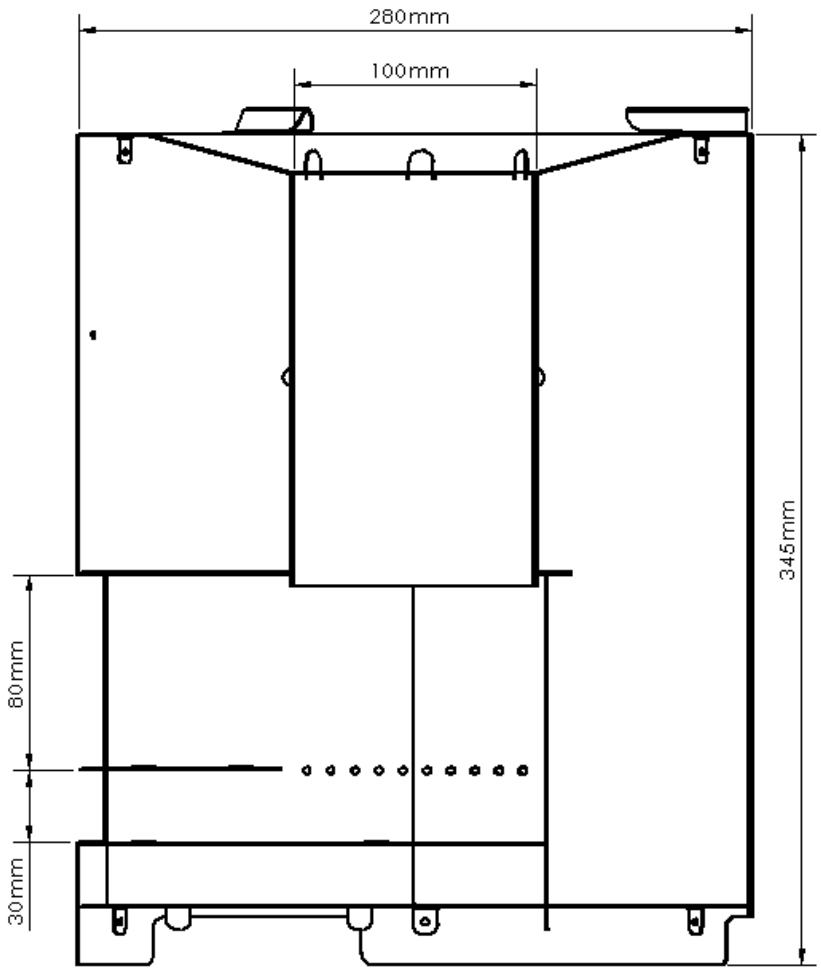

Figure A.1: SFR 9 natural draft cookstove cross-sectional view and dimensions

Additional Results from Cone Deck Optimization Study

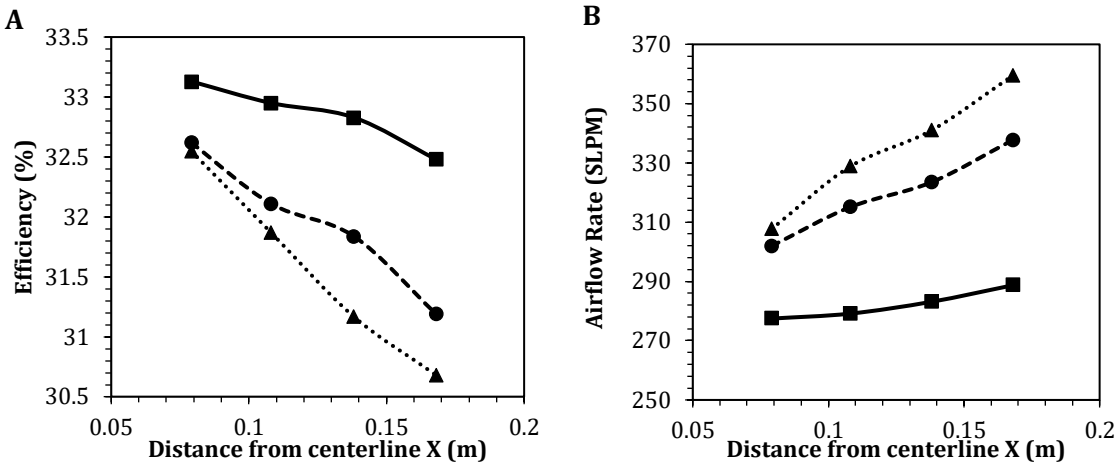

Figure A.2: (A) Heat transfer efficiency as a function of X. The solid curve is for a Y of 8 mm, the dashed curve is for a Y of 16 mm, and the dotted curve is for a Y of 24 mm. (B) Airflow rate as a function of X. Each curve represents the same Y as A.2(A). All curves are for a constant firepower of 4 kW and for a pot support height of 11 mm.

Figure A.2(A) shows the heat transfer efficiency and Figure A.2(B) shows the airflow rate as a function of horizontal distance from the centerline of the cookstove to the top of the cone deck, X. Each curve represents a constant vertical distance from the bottom of the cone deck to the top, Y. We see that the efficiency reduces as X increases, and for a constant X, reduces as Y increases. The difference in efficiency between a Y of 8 mm and 16 mm is much greater than the difference between a Y of 16 mm and 24 mm, provided that the firepower can be held relatively constant. Therefore, the plot suggests that a 'flatter' cone deck is better than the current 'steeper' design. The airflow rate, on the other hand, is the lowest for the smallest value of Y, since the 'flatter' cone deck geometrically restricts the airflow. This also explains why the flatter cone deck has a higher heat transfer efficiency; the air restriction causes the bulk gas temperature in the top part of the riser to increase, hence increasing heat transfer to the pot.

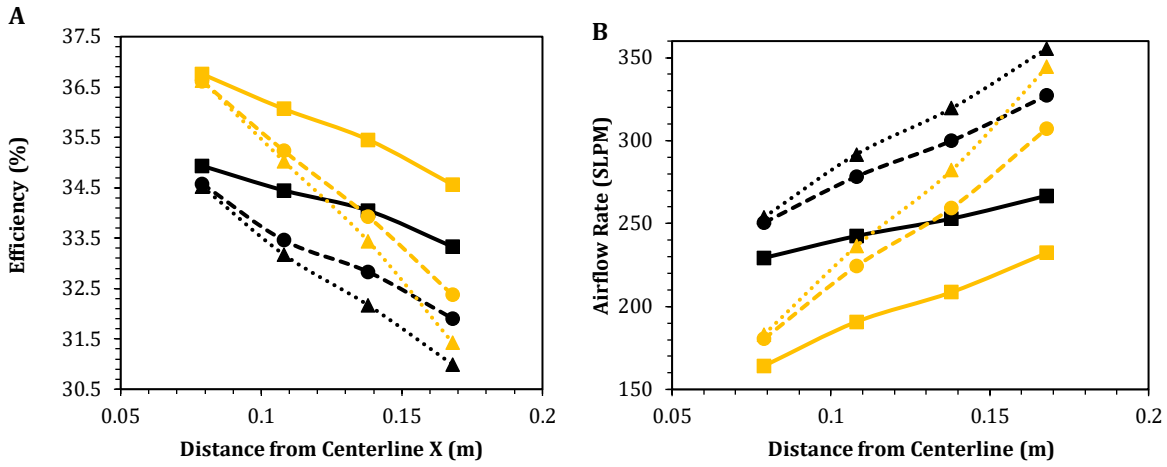

Figure A.3: (A) Heat transfer efficiency as a function of X. The solid curves are for a Y of 8 mm, the dashed curves are for a Y of 16 mm, and the dotted curves are for a Y of 24 mm. The yellow curves are for a pot support height of 7 mm and the black curves are for a pot support height of 9 mm. (B) Airflow rate as a function of X. Each curve represents the same Y and pot support height as Fig A.3(A). All curves are for a constant firepower of 4 kW.

Figure A.3 shows the same plots as Figure A.2, but for pot support heights of 7mm (yellow curves) and 9mm (black curves). We observe that a lower pot support, keeping everything else constant, results in a higher heat transfer efficiency, provided that the firepower can be maintained at 4 kW. Like in Figure A.2(A), a 'flatter' cone deck leads to higher efficiency. Interestingly, for a pot support height of 7 mm and the smallest distance X, the heat transfer efficiency does not depend on Y, but is constant for all Y. We hypothesize that this is because the minimum flow area in the cookstove is not affected, due to the pot support height and the distance from the centerline X being very small. Therefore, the airflow rate remains relatively unchanged, as shown in Figure A.3(B), leading to similar bulk gas temperatures for all values of distance X. This causes the heat transfer efficiency to remain fairly constant, even though the distance Y is varied.

The takeaway from this analysis is that a 'flatter' cone deck with a lower pot support height should increase the heat transfer efficiency by causing the stove to run hotter, provided

that the firepower can be maintained. Considering the restrictions posed to the airflow by the changed geometric parameters, this might not be easy to achieve; we recognize that a lower airflow rate without sufficient mixing may cause increased PM emissions and issues with keeping the fire lit. Therefore, the ideal cone deck is not the one we have exactly optimized for, but one that, in addition to our analysis, also does not constrict the airflow enough to cause the wood sticks to smolder.

We examine the relationship between excess air and thermal efficiency by varying the pot support height. It is known, and we have experimentally observed, that the pot support height strongly impacts the excess air and stove thermal efficiency. Using the computational model, we vary the pot support height from 7 mm to 15 mm for a constant firepower of 4 kW and extract the total air mass flow rate and excess air ratio as shown in Figure A.4(A). The data show the excess air ratio and airflow rate increase and appears to asymptote to a constant value as the pot support height increases. We hypothesize that the air flow rate is primarily a function of the pressure drop across the narrow region of the pot supports and that decreasing the pot support height increases the pressure drop and reduces the total air flow rate. As we increase the pot support height, obstruction to the flow is reduced and the excess air increases. In this case, we expect the excess air ratio and airflow rate curves to have the same shape since the firepower is held constant. Both curves appear to asymptote to a constant value as the pot support height increases since the effect of the pot on the airflow will reduce as the pot is moved further away from the cookstove.

Figure A.4(B) shows the stove efficiency as a function of pot support height. We define the stove efficiency as the percentage of the total heating value of the fuel that is delivered to the pot of water. We observe that the efficiency is 35% for a pot support height of 7 mm

and reduces to 30% as the pot support height is increased to 15 mm. The efficiency decreases with pot support height because airflow through the cookstove increases as the pot support height is increased which results in a lower bulk gas temperature and less heat transferred to the pot. This result is similar to that of Baldwin [14], who predicted that narrower gaps in the cookstove lead to higher heat transfer to the pot. Further reducing the pot support height would, however, increasingly reduce the airflow rate until combustion can no longer be sustained.

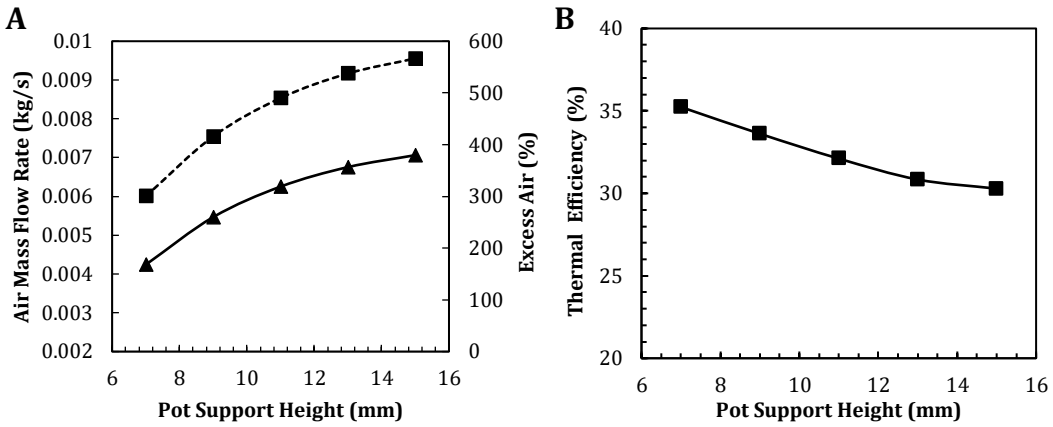

Figure A.4: (A) Air mass flow rate (solid line with triangles) and excess air (dashed line with squares) as a function of pot support height. (B) Heat transfer efficiency to the pot as a function of pot support height.

Appendix B: Fluent UDF's

This section contains Fluent User Defined Functions (UDF's) for the Method of Moments with Interpolative Closure model for predicting soot behavior. These UDF's model source terms for nucleation, surface growth, coagulation and oxidation for the first three moments of the soot PSDF.

```
#include "udf.h"

/* universal constants and environmental conditions */
#define avogad 6.024e26 /* kmole^-1 */
#define kB 1.3806e-23 /* J/K */
#define R 8.314 /* kJ kmole^-1 Kelvin^-1 */
#define pi 3.14159
#define oneThird 1.0/3.0
#define oneHalf 1.0/2.0
#define oneSixth 1.0/6.0
#define twoThird 2.0/3.0
#define Patm 1.01e5 /* Pa */
#define ScT 0.7 /* Turbulent Schmidt Number */
#define PrT 0.85 /* Turbulent Prandtl Number */

/* molecular weights in kg/kmol */
#define C2H2MW 26.04
#define H2MW 2.01
#define HMW 1.007
#define O2MW 32
#define OHMW 13
#define H2OMW 16
#define pyrMW 202.25
#define benzeneMW 78.11
#define naphMW 128.17
#define phenanMW 178.234

/* masses and diameters of atoms */
#define mC 1.9944e-26 /* kg/atom */
#define mOH 2.8232e-26 /* kg/atom */
#define dAir 3.6e-10 /* m */
#define dC 2.2e-10 /* m */
#define dA 1.395*sqrt(3)
#define dPyr 2.5*1.395e-10*sqrt(3) /* m */
#define dBenzene 1.395e-10 /* m */
```

```
/* number of C atoms in species */
#define NPyr 16
#define NBenzene 6
#define NPhenan 14
#define NNaph 10

/* MOMIC parameters */
#define gammaAcet 1e-10
#define gammaPyr 0.001
#define gammaBenzene 0.001
#define vDW 4.0
#define siteDensity 2.3e19 /* m^2 */
#define rhoSoot 1800 /* kg/m^3 */
#define normParameter 1e15
#define a1 12.65
#define a2 -56.3e-4
#define b1 -1.38
#define b2 6.8e-4

/* MOMIC kinetic parameters SI units */
#define A1f 4.2e10
#define Ea1f 13000*4.18
#define A1r 3.9e9
#define Ea1r 11000*4.18
#define A2f 1.0e7
#define n2f 0.734
#define Ea2f 1430*4.18
#define A2r 3.68e5
#define n2r 1.139
#define Ea2r 17100*4.18
#define A3 2.0e10
#define A4 8.0e4
#define n4 1.56
#define Ea4 3800*4.18
#define A5 2.2e9
#define Ea5 7500*4.18
#define gammaOH 0.13

real lagInterp3mom(real p, real m0, real m1, real m2); /* Lagragian
interpolation */
real pyrNucSource(cell_t c,Thread *t);
real chiSootCalc(cell_t c,Thread *t, real cellTemp, real cellRho);
real HACAalphaCalc(real Temp, real cellM0, real cellM1);
real fractionalMoments(real p, real m0, real m1, real m2);
real GcCalc(r, Kc, KcPrime, cellM0, cellM1, cellM2);
real fracMomFirstDiffM0(real p, real m0, real m1, real m2);
real fracMomFirstDiffM1(real p, real m0, real m1, real m2);
real fracMomFirstDiffM2(real p, real m0, real m1, real m2);
real GcDiffM2Calc(r, Kc, KcPrime, cellM0, cellM1, cellM2);
real factorialCalc(n);
```

```
DEFINE_SOURCE (m_0_NucSourcePyr,c,t,dS,eqn)
{


    real sourcePyr = pyrNucSource(c,t);

    dS[eqn] = 0.0;
    C_UDMI(c,t,0) = sourcePyr;
    return sourcePyr;
}

DEFINE_SOURCE (m_1_NucSourcePyr,c,t,dS,eqn)
{

    real sourcePyr = (2*NPyr)*pyrNucSource(c,t);
    real source = sourcePyr;


    dS[eqn] = 0.0;
    C_UDMI(c,t,1) = source;
    return source;
}

DEFINE_SOURCE (m_2_NucSourcePyr,c,t,dS,eqn)
{

    real sourcePyr = (2*NPyr)*(2*NPyr)*pyrNucSource(c,t);
    real source = sourcePyr;

    dS[eqn] = 0.0;
    C_UDMI(c,t,2) = source;
    return source;
}

DEFINE_SOURCE (m_1_C2H2Source,c,t,dS,eqn)
{
    real source;
    real cellRho = C_R(c,t);
    real cellTemp = C_T(c,t);
    real cellM0 = cellRho*C_UDSI(c,t,0);
    real cellM1 = cellRho*C_UDSI(c,t,1);
    real cellM2 = cellRho*C_UDSI(c,t,2);
    real a = a1 + a2*cellTemp;
    real b = b1 + b2*cellTemp;
    real alpha = tanh(a/log10(cellM1/cellM0)+b);
    if (alpha < 0 ) { alpha = 0.01; }

    C_UDMI(c,t,19) = alpha;

    Material *mat1 = THREAD_MATERIAL(t);

    int idC2H2 = mixture_specie_index(mat1, "c2h2");
    real C2H2Mf = Pdf_Yi(c,t,idC2H2);
    real C2H2Mc = C2H2Mf*cellRho/C2H2MW;
```

```
    real k4 = A4*pow(cellTemp, n4)*exp(-Ea4/(R*cellTemp));
    real chiSoot = chiSootCalc(c,t,cellTemp,cellRho);
    real Cs = pow((6*mC/(pi*rhoSoot)),oneThird);

    real muTwoThird = pow(10, lagInterp3mom(twoThird, 0.0,
         log10(cellM1/cellM0), log10(cellM2/cellM0)));

    source =
         2*k4*C2H2Mc*alpha*chiSoot*pi*pow(Cs,2)*muTwoThird*cellM0*fudgeFa
         c2;
    dS[eqn] =
         2*k4*C2H2Mc*alpha*chiSoot*pi*pow(Cs,2)*pow(cellM0,twoThird/3)*po
         w(cellM2,-oneThird/3)*pow(cellM1,-oneThird/3)*8.0/9.0*fudgeFac2;

    C_UDMI(c,t,3) = source;

    return source;
}

DEFINE_SOURCE (m_2_C2H2Source,c,t,dS,eqn)
{
    real source;
    real cellRho = C_R(c,t);
    real cellTemp = C_T(c,t);
    real cellM0 = cellRho*C_UDSI(c,t,0);
    real cellM1 = cellRho*C_UDSI(c,t,1);
    real cellM2 = cellRho*C_UDSI(c,t,2);
    real a = a1 + a2*cellTemp;
    real b = b1 + b2*cellTemp;
    real alpha = tanh(a/log10(cellM1/cellM0)+b);
    if (alpha < 0 ) { alpha = 0.01; }

    Material *mat = THREAD_MATERIAL(t);

    int idC2H2 = mixture_specie_index(mat, "c2h2");
    real C2H2Mf = Pdf_Yi(c,t,idC2H2);
    real C2H2Mc = C2H2Mf*cellRho/C2H2MW;

    real k4 = A4*pow(cellTemp, n4)*exp(-Ea4/(R*cellTemp));
    real chiSoot = chiSootCalc(c,t,cellTemp,cellRho);
    real Cs = pow((6*mC/(pi*rhoSoot)),oneThird);

    real MtwoThird = cellM0*pow(10, lagInterp3mom(twoThird,
         log10(cellM0/cellM0), log10(cellM1/cellM0),
         log10(cellM2/cellM0)));
    real MfiveThird = cellM0*pow(10, lagInterp3mom(5*oneThird,
         log10(cellM0/cellM0), log10(cellM1/cellM0),
         log10(cellM2/cellM0)));

    source = k4*C2H2Mc*alpha*chiSoot*pi*pow(Cs,2)*(4*MtwoThird +
         4*MfiveThird)*fudgeFac2;
```

```
    dS[eqn] = k4*C2H2Mc*alpha*chiSoot*pi*pow(Cs,2)*(-
         4*pow(cellM0,twoThird/3)*pow(cellM2,-11*oneThird/3)*\
         pow(cellM1,-8*oneThird/3)/9.0+4*5.0/9.0*pow(cellM0,-
         oneThird/3)*pow(cellM2,-
         4*oneThird/3)*pow(cellM1,5*oneThird/3))*fudgeFac2;

    C_UDMI(c,t,4) = source;

    return source;
}

DEFINE_SOURCE(m_1_OxSource,c,t,dS,eqn)
{
    real source;
    real sourceO2;
    real sourceOH;
    real cellRho = C_R(c,t);
    real cellTemp = C_T(c,t);
    real cellM0 = cellRho*C_UDSI(c,t,0);
    real cellM1 = cellRho*C_UDSI(c,t,1);
    real cellM2 = cellRho*C_UDSI(c,t,2);
    real a = a1 + a2*cellTemp;
    real b = b1 + b2*cellTemp;
    real alpha = tanh(a/log10(cellM1/cellM0)+b);
    if (alpha < 0 ) { alpha = 0.01; }

    Material *mat = THREAD_MATERIAL(t);

    int idO2 = mixture_specie_index(mat, "o2");
    int idOH = mixture_specie_index(mat, "oh");

    real O2Mf = Pdf_Yi(c,t,idO2);
    real OHMf = Pdf_Yi(c,t,idOH);

    real O2Mc = O2Mf*cellRho/O2MW;
    real OHMc = OHMf*cellRho/OHMW;

    real k5 = A5*exp(-Ea5/(R*cellTemp));
    real chiSoot = chiSootCalc(c,t,cellTemp,cellRho);
    real Cs = pow((6*mC/(pi*rhoSoot)),oneThird);

    real MtwoThird = cellM0*pow(10, lagInterp3mom(twoThird,
        log10(cellM0/cellM0), log10(cellM1/cellM0),
        log10(cellM2/cellM0)));

    sourceO2 = -2*k5*O2Mc*alpha*chiSoot*pi*pow(Cs,2)*MtwoThird;
    sourceOH = -
        gammaOH*OHMc*sqrt(pi*kB*cellTemp/(2*mOH))*pi*pow(Cs,2)*MtwoThird*a
        vogad;
    source = sourceO2 + sourceOH;

    C_UDMI(c,t,5) = sourceO2;
    C_UDMI(c,t,6) = sourceOH;
```

```
    C_UDMI(c,t,7) = source*fudgeFac1;

    dS[eqn] = -
        2*k5*O2Mc*alpha*chiSoot*pi*pow(Cs,2)*pow(cellM0,twoThird/3)*pow(ce
        llM2,-oneThird/3)*pow(cellM1,-oneThird/3)*8.0/9.0;

    return source*fudgeFac1;
}

DEFINE_SOURCE(m_2_OxSource,c,t,dS,eqn)
{
    real source;
    real sourceO2;
    real sourceOH;
    real cellRho = C_R(c,t);
    real cellTemp = C_T(c,t);
    real cellM0 = cellRho*C_UDSI(c,t,0);
    real cellM1 = cellRho*C_UDSI(c,t,1);
    real cellM2 = cellRho*C_UDSI(c,t,2);
    real a = a1 + a2*cellTemp;
    real b = b1 + b2*cellTemp;
    real alpha = tanh(a/log10(cellM1/cellM0)+b);
    if (alpha < 0 ) { alpha = 0.01; }

    Material *mat = THREAD_MATERIAL(t);

    int idO2 = mixture_specie_index(mat, "o2");
    int idOH = mixture_specie_index(mat, "oh");

    real O2Mf = Pdf_Yi(c,t,idO2);
    real OHMf = Pdf_Yi(c,t,idOH);

    real O2Mc = O2Mf*cellRho/O2MW;
    real OHMc = OHMf*cellRho/OHMW;

    real k5 = A5*exp(-Ea5/(R*cellTemp));
    real chiSoot = chiSootCalc(c,t,cellTemp,cellRho);
    real Cs = pow((6*mC/(pi*rhoSoot)),oneThird);

    real MtwoThird = cellM0*pow(10, lagInterp3mom(twoThird,
         log10(cellM0/cellM0), log10(cellM1/cellM0),
         log10(cellM2/cellM0)));
    real MfiveThird = cellM0*pow(10, lagInterp3mom(5*oneThird,
         log10(cellM0/cellM0), log10(cellM1/cellM0),
         log10(cellM2/cellM0)));

    sourceO2 = k5*O2Mc*alpha*chiSoot*pi*pow(Cs,2)*(4*MtwoThird -
         4*MfiveThird);
    sourceOH =
         gammaOH*OHMc*sqrt(pi*kB*cellTemp/(2*mOH))*pi*pow(Cs,2)*(4*MtwoTh
         ird - 4*MfiveThird);

    source = sourceO2 + sourceOH;
```

```
    C_UDMI(c,t,8) = sourceO2;
    C_UDMI(c,t,9) = sourceOH;

    dS[eqn] = k5*O2Mc*alpha*chiSoot*pi*pow(Cs,2)*(-
         4*pow(cellM0,twoThird/3)*pow(cellM2,-11*oneThird/3)*\
                 pow(cellM1,-8*oneThird/3)/9.0+4*5.0/9.0*pow(cellM0,-
         oneThird/3)*pow(cellM2,-4*oneThird/3)*pow(cellM1,5*oneThird/3));


    C_UDMI(c,t,10) = source*fudgeFac1;
    return source*fudgeFac1;
}

DEFINE_SOURCE (m_0_CoagSource,c,t,dS,eqn)
{
    real source;
    real cellPressure = C_P(c,t) + Patm;
    real cellRho = C_R(c,t);
    real cellTemp = C_T(c,t);
    real cellM0 = cellRho*C_UDSI(c,t,0);
    real cellM1 = cellRho*C_UDSI(c,t,1);
    real cellM2 = cellRho*C_UDSI(c,t,2);
    real lamVisc = C_MU_L(c,t);

    real muOneThird = pow(10, lagInterp3mom(oneThird,
         log10(cellM0/cellM0), log10(cellM1/cellM0),
         log10(cellM2/cellM0)));

    real meanFreePath = kB*cellTemp/(sqrt(2)*pi*pow(dAir,2)*cellPressure);
    real avgDia = pow(10, lagInterp3mom(oneThird, log10(cellM0/cellM0),
         log10(cellM1/cellM0), log10(cellM2/cellM0)))*dC;
    real Kn = 2*meanFreePath/avgDia;

    C_UDMI(c,t,20) = meanFreePath;
    C_UDMI(c,t,21) = avgDia;
    C_UDMI(c,t,22) = Kn;

    real Kc = 2*kB*cellTemp/(3*lamVisc);
    real KcPrime = 2.514*meanFreePath*pow(pi*rhoSoot/6,oneThird);
    real Kf =
         vDW*sqrt(6*kB*cellTemp/rhoSoot)*pow(3*mC/(4*pi*rhoSoot),oneSixth
         );

    real muTwoThird = pow(10, lagInterp3mom(twoThird,
         log10(cellM0/cellM0), log10(cellM1/cellM0),
         log10(cellM2/cellM0)));
    real muFourThird = pow(10, lagInterp3mom(4*oneThird,
         log10(cellM0/cellM0), log10(cellM1/cellM0),
         log10(cellM2/cellM0)));
    real muFiveThird = pow(10, lagInterp3mom(5*oneThird,
         log10(cellM0/cellM0), log10(cellM1/cellM0),
         log10(cellM2/cellM0)));

□
```

```
real muSevenThird = pow(10, lagInterp3mom(7*oneThird,
     log10(cellM0/cellM0), log10(cellM1/cellM0),
     log10(cellM2/cellM0)));
real muEightThird = pow(10, lagInterp3mom(8*oneThird,
     log10(cellM0/cellM0), log10(cellM1/cellM0),
     log10(cellM2/cellM0)));
real muMinusOneThird = pow(10, lagInterp3mom(-oneThird,
     log10(cellM0/cellM0), log10(cellM1/cellM0),
     log10(cellM2/cellM0)));
real muMinusTwoThird = pow(10, lagInterp3mom(-twoThird,
     log10(cellM0/cellM0), log10(cellM1/cellM0),
     log10(cellM2/cellM0)));

real muMinusOneHalf = pow(10, lagInterp3mom(-oneHalf,
     log10(cellM0/cellM0), log10(cellM1/cellM0),
     log10(cellM2/cellM0)));
real muMinusOneSixth = pow(10, lagInterp3mom(-oneSixth,
     log10(cellM0/cellM0), log10(cellM1/cellM0),
     log10(cellM2/cellM0)));
real muOneSixth = pow(10, lagInterp3mom(oneSixth,
     log10(cellM0/cellM0), log10(cellM1/cellM0),
     log10(cellM2/cellM0)));
real muOneHalf = pow(10, lagInterp3mom(oneHalf, log10(cellM0/cellM0),
     log10(cellM1/cellM0), log10(cellM2/cellM0)));
real muThreeHalf = pow(10, lagInterp3mom(3*oneHalf,
     log10(cellM0/cellM0), log10(cellM1/cellM0),
     log10(cellM2/cellM0)));
real muFiveSixth = pow(10, lagInterp3mom(5*oneSixth,
     log10(cellM0/cellM0), log10(cellM1/cellM0),
     log10(cellM2/cellM0)));
real muSevenSixth = pow(10, lagInterp3mom(7*oneSixth,
     log10(cellM0/cellM0), log10(cellM1/cellM0),
     log10(cellM2/cellM0)));
real muElevenSixth = pow(10, lagInterp3mom(11*oneSixth,
     log10(cellM0/cellM0), log10(cellM1/cellM0),
     log10(cellM2/cellM0)));
real muThirteenSixth = pow(10, lagInterp3mom(13*oneSixth,
     log10(cellM0/cellM0), log10(cellM1/cellM0),
     log10(cellM2/cellM0)));



real f_0_0_0 = 2*(muMinusOneHalf*muOneSixth + pow(muMinusOneSixth,2));
real f_1_0_0 = 2*(muMinusOneHalf*muSevenSixth +
     2*muMinusOneSixth*muFiveSixth + muOneSixth*muOneHalf);
real f_2_0_0 = 2*(muMinusOneHalf*muThirteenSixth +
     2*muMinusOneSixth*muElevenSixth + muOneSixth*muThreeHalf + \
      2*muOneHalf*muSevenSixth + 2*pow(muFiveSixth,2));

real f_oneHalf_0_0 = pow(10, lagInterp3mom(oneHalf, log10(f_0_0_0),
     log10(f_1_0_0), log10(f_2_0_0)));
```

```
    real Gc = -Kc*(1 + muOneThird*muMinusOneThird +
         KcPrime*(muMinusOneThird +
         muOneThird*muMinusTwoThird))*pow(cellM0,2)*normParameter;
    real Gf = -0.5*Kf*pow(cellM0,2)*f_oneHalf_0_0*normParameter;


    C_UDMI(c,t,13) = Gc;
    C_UDMI(c,t,14) = Gf;


    if (Kn < 0.1) { source = Gc; }

    else if (Kn > 8.0) { source = Gf; }

    else { source = Gc*Gf/(Gc + Gf); }

    dS[eqn] = 0.0;

    C_UDMI(c,t,15) = source;
    return source;

}
```

Complete documentation can be found at:

github.com/anamol/MethodOfMomentsSootModel

Appendix C: Experimental Raw Data

Table C.1: Measured soot emission, flame lift-off and flame length data for free flames.

Flame	Nozzle diameter (mm)	Ethylene flow rate (SLPM)	Avg Exit Velocity (m/s)	Lift off (mm)	Flame Length (m)	Soot emissions (mg/min)
A	1.5	5.3	50	12	0.407	0.3
B	1.5	6.36	60	19	0.433	0.154
C	1.5	7.42	70	26	0.436	0.12
D	1.5	8.48	80	32	0.453	0.186
E	2.18	6.72	30	8	0.475	4.81
F	2.18	8.95	40	10	0.52	1.31
G	2.18	10.52	47	16	0.569	0.63
H	2.18	13.44	60	31	0.598	0.505
I	3	10.6	25	4	0.573	16.035
J	3	12.73	30	9	0.63	10.63
K	3	14.84	35	12	0.636	6.41
L	3	16.96	40	15	0.703	2.95
M	3	22.05	52	26	0.758	2.41
N	4.5	5.72	6	0	0.467	22.25
O	4.5	8.11	8	0	0.554	27.05
P	4.5	14.31	15	0	0.648	50.12
Q	4.5	19.08	20	0	0.741	58.41

Table C.2: Measured particle size distributions $\left(dN/dlogD_p\right)$ of emitted soot for free flames.

Flame	11.5 nm (#/cm3)	15.4 nm (#/cm3)	20.5 nm (#/cm3)	27.4 nm (#/cm3)	36.5 nm (#/cm3)	48.7 nm (#/cm3)	64.9 nm (#/cm3)	86.6 nm (#/cm3)	115.5 nm (#/cm3)	154 nm (#/cm3)	205.4 nm (#/cm3)	273.8 nm (#/cm3)
A	9358	16125	19586	36657	41320	37051	31214	28568	22760	11544	1314	0
B	1567	3940	5267	9020	11220	11768	11052	9501	6363	2337	0	0
C	569	1438	1910	3637	5540	6827	6935	5785	3579	1150	0	0
D	555	1304	1693	3213	4863	5935	5979	4978	3149	1141	0	0
E	37875	92898	137934	281344	413786	638170	924994	1135900	1052996	661800	174252	0
F	22939	71469	102271	166275	224043	284620	333275	340965	266450	131273	9585	0
G	17455	33310	38660	71406	93011	103125	103798	95763	68207	27286	1660	0
H	8122	17484	21612	34222	41568	42445	38397	31333	19671	6286	0	0
I	58923	249361	485672	911264	1354607	2430940	3951187	5108976	4760958	2882737	574756	0
J	114953	302107	501171	1009149	1550225	2456788	3533489	4212511	3715070	2121794	311586	0
K	150662	332137	497030	1021467	1471399	2050560	2668403	3007541	2533242	1339835	71890	0
L	141527	328418	441487	819590	1202922	1583550	1848147	1844067	1375456	601040	0	0
M	27832	56216	67172	107040	122901	116329	99208	81229	53683	19283	0	0
N	0	38943	152679	268751	183344	628195	1734109	2987609	3398189	2548941	989809	0
O	0	76805	204059	298255	393746	1204298	2676600	4075861	4321575	3078387	1095740	0
P	46983	261976	662848	1317500	1735602	3596259	6824995	9791672	9822309	6456099	1790059	0
Q	46020	296558	747600	1512429	2306004	4765542	8550090	11718965	11439628	7392762	2013812	0

Table C.3: Measured soot emission data for flames impinging on cold surface

Flame	Surface height (mm)	Non-dimensionalized surface height	Ethylene flow rate (SLPM)	Soot Emissions (mg/min)
A	69	0.170	5.3	8.967
	103	0.253	5.3	11.731
	138	0.339	5.3	16.812
	172	0.423	5.3	22.646
	206	0.506	5.3	24.206
	241	0.592	5.3	17.904
	275	0.676	5.3	11.868
B	69	0.159	6.36	5.401
	103	0.238	6.36	5.660
	138	0.319	6.36	9.756
	172	0.397	6.36	9.623
	206	0.476	6.36	8.303
	241	0.557	6.36	8.119
	275	0.635	6.36	4.967
C	69	0.158	7.42	1.436
	103	0.236	7.42	0.714
	138	0.317	7.42	3.056
	172	0.394	7.42	3.101
	206	0.472	7.42	3.067
	241	0.553	7.42	3.285
	275	0.631	7.42	2.017
D	69	0.152	8.48	0.180
	103	0.227	8.48	0.493
	138	0.305	8.48	1.142
	172	0.380	8.48	1.503
	206	0.455	8.48	2.020
	241	0.532	8.48	2.358
	275	0.607	8.48	2.642

Table C.3 (continued): Measured soot emission data for flames impinging on cold surface

Flame	Surface height (mm)	Non-dimensionalized surface height	Ethylene flow rate (SLPM)	Soot Emissions (mg/min)
E	100	0.211	6.72	26.695
	150	0.316	6.72	52.435
	200	0.421	6.72	64.577
	250	0.526	6.72	58.613
	300	0.632	6.72	41.692
	350	0.737	6.72	23.237
	400	0.842	6.72	10.258
F	100	0.192	8.95	11.695
	150	0.288	8.95	28.981
	200	0.385	8.95	36.888
	250	0.481	8.95	37.757
	300	0.577	8.95	31.326
	350	0.673	8.95	16.188
	400	0.769	8.95	4.440
G	100	0.176	10.52	3.802
	150	0.264	10.52	10.697
	200	0.351	10.52	18.163
	250	0.439	10.52	21.906
	300	0.527	10.52	20.359
	350	0.615	10.52	9.577
	400	0.703	10.52	3.016
H	100	0.167	13.44	1.234
	150	0.251	13.44	1.555
	200	0.334	13.44	2.588
	250	0.418	13.44	6.222
	300	0.502	13.44	6.125
	350	0.585	13.44	3.645
	400	0.669	13.44	2.814

Table C.3 (continued): Measured soot emission data for flames impinging on cold surface

Flame	Surface height (mm)	Non-dimensionalized surface height	Ethylene flow rate (SLPM)	Soot Emissions (mg/min)
I	138	0.241	10.6	72.460
	206	0.360	10.6	89.658
	275	0.480	10.6	88.332
	345	0.602	10.6	70.490
	413	0.721	10.6	39.865
	482	0.841	10.6	20.900
	550	0.960	10.6	19.180
J	138	0.219	12.73	44.747
	206	0.327	12.73	55.741
	275	0.437	12.73	59.187
	345	0.548	12.73	58.157
	413	0.656	12.73	33.197
	482	0.765	12.73	12.987
	550	0.873	12.73	9.365
K	138	0.217	14.84	27.114
	206	0.324	14.84	30.100
	275	0.432	14.84	40.746
	345	0.542	14.84	47.648
	413	0.649	14.84	30.281
	482	0.758	14.84	10.576
	550	0.865	14.84	5.260
L	138	0.196	16.96	8.724
	206	0.293	16.96	15.421
	275	0.391	16.96	26.318
	345	0.491	16.96	40.620
	413	0.587	16.96	33.197
	482	0.686	16.96	11.052
	550	0.782	16.96	3.059

Table C.3 (continued): Measured soot emission data for flames impinging on cold surface

Flame	Surface height (mm)	Non-dimensionalized surface height	Ethylene flow rate (SLPM)	Soot Emissions (mg/min)
M	138	0.182	22.05	2.855
	206	0.272	22.05	3.230
	275	0.363	22.05	9.342
	345	0.455	22.05	15.186
	413	0.545	22.05	17.462
	482	0.636	22.05	8.208
	550	0.726	22.05	3.041
N	100	0.214	5.72	39.458
	150	0.321	5.72	34.714
	200	0.428	5.72	36.496
	250	0.535	5.72	42.532
	300	0.642	5.72	41.757
	350	0.749	5.72	38.971
	400	0.857	5.72	34.645
O	100	0.181	8.11	67.630
	150	0.271	8.11	71.903
	200	0.361	8.11	71.729
	250	0.451	8.11	65.222
	300	0.542	8.11	54.208
	350	0.632	8.11	50.666
	400	0.722	8.11	48.867

Table C.4: Measured particle size distributions $\left(dN/dlogD_p\right)$ of emitted soot for Flame A impinging on a cold surface.

Surface Height (mm)	11.5 nm (#/cm3)	15.4 nm (#/cm3)	20.5 nm (#/cm3)	27.4 nm (#/cm3)	36.5 nm (#/cm3)	48.7 nm (#/cm3)	64.9 nm (#/cm3)	86.6 nm (#/cm3)	115.5 nm (#/cm3)	154 nm (#/cm3)	205.4 nm (#/cm3)	273.8 nm (#/cm3)
69	0	39259	161853	194566	216273	1081186	2685056	4138051	4134811	2521165	367839	0
103	0	22351	140788	121003	27467	843152	2555610	4251254	4518698	3008456	728454	0
138	0	68	158965	114885	0	401506	2350125	4627722	5454677	4095557	1511250	0
172	0	0	180802	163375	0	13423	1970041	4664564	5970592	4818187	2088277	0
206	0	0	185526	155444	0	27992	2042737	4692042	5979402	4839120	2117203	0
241	0	2867	163108	212775	0	306483	2061166	4252046	5161100	3976081	1540754	0
275	0	27344	148328	199651	90205	585593	1823062	3172850	3550848	2539812	800950	0

Table C.5: Measured particle size distributions $\left(dN/dlogD_p\right)$ of emitted soot for Flame B impinging on a cold surface.

Surface Height (mm)	11.5 nm (#/cm3)	15.4 nm (#/cm3)	20.5 nm (#/cm3)	27.4 nm (#/cm3)	36.5 nm (#/cm3)	48.7 nm (#/cm3)	64.9 nm (#/cm3)	86.6 nm (#/cm3)	115.5 nm (#/cm3)	154 nm (#/cm3)	205.4 nm (#/cm3)	273.8 nm (#/cm3)
69	4592	88563	186331	329007	698512	1796413	3291604	4318715	3880439	2079557	40128	0
103	3339	73727	171440	262431	525497	1574406	3128810	4291559	3955218	2169780	65618	0
138	0	38775	184234	138724	93987	1156779	3209343	5116058	5234766	3297594	594740	0
172	0	34534	197943	211825	78743	940546	2856234	4785978	5070200	3308693	689649	0
206	0	44282	183284	247801	192230	993153	2649039	4278964	4470900	2904553	616955	0
241	1235	56450	185672	317277	323305	1023847	2418107	3765579	3854400	2434644	431934	0
275	6239	68513	172123	291843	373584	969385	2020664	2956163	2910129	1766005	249329	0

Table C.6: Measured particle size distributions $\left(dN/dlogD_p\right)$ of emitted soot for Flame C impinging on a cold surface.

Surface Height (mm)	11.5 nm (#/cm3)	15.4 nm (#/cm3)	20.5 nm (#/cm3)	27.4 nm (#/cm3)	36.5 nm (#/cm3)	48.7 nm (#/cm3)	64.9 nm (#/cm3)	86.6 nm (#/cm3)	115.5 nm (#/cm3)	154 nm (#/cm3)	205.4 nm (#/cm3)	273.8 nm (#/cm3)
69	85366	212338	333960	749932	1408926	2097014	2470702	2279726	1461750	395808	0	0
103	84670	188522	283511	633273	1077890	1444977	1557960	1338012	799116	174379	0	0
138	39757	132395	225034	462983	866976	1562271	2290502	2612932	2094588	934256	0	0
172	32428	112517	192695	390271	710405	1362729	2135227	2573954	2163954	1045348	0	0
206	19847	117219	196834	329778	681335	1432933	2296625	2749258	2287515	1101627	0	0
241	20888	99030	186830	342756	598952	1251525	2111577	2677324	2342472	1200271	996	0
275	17904	91326	173454	306185	482730	914488	1486626	1865291	1630701	837879	35442	0

Table C.7: Measured particle size distributions $\left(dN/dlogD_p\right)$ of emitted soot for Flame D impinging on a cold surface.

Surface Height (mm)	11.5 nm (#/cm3)	15.4 nm (#/cm3)	20.5 nm (#/cm3)	27.4 nm (#/cm3)	36.5 nm (#/cm3)	48.7 nm (#/cm3)	64.9 nm (#/cm3)	86.6 nm (#/cm3)	115.5 nm (#/cm3)	154 nm (#/cm3)	205.4 nm (#/cm3)	273.8 nm (#/cm3)
69	178712	413190	441528	574075	526458	341420	146276	44913	17353	4642	0	812
103	139545	304163	367391	622876	719686	614052	393848	192502	47085	0	0	0
138	122245	260803	346402	710079	1020174	1134769	1019036	742103	363895	19868	0	0
172	102229	236926	342962	728662	1173001	1549218	1697576	1520017	964803	254549	0	0
206	99019	229693	328557	723641	1289844	1907503	2299767	2216545	1505451	473560	0	0
241	85321	194009	286473	644035	1178199	1810407	2267303	2266402	1609686	579270	0	0
275	60587	174404	247789	482286	935879	1539657	2009948	2044987	1471186	546210	0	0

Table C.8: Measured particle size distributions $\left(dN/dlogD_p\right)$ of emitted soot for Flame E impinging on a cold surface.

Surface Height (mm)	11.5 nm (#/cm3)	15.4 nm (#/cm3)	20.5 nm (#/cm3)	27.4 nm (#/cm3)	36.5 nm (#/cm3)	48.7 nm (#/cm3)	64.9 nm (#/cm3)	86.6 nm (#/cm3)	115.5 nm (#/cm3)	154 nm (#/cm3)	205.4 nm (#/cm3)	273.8 nm (#/cm3)
100	0	71256	237290	202409	0	826214	3261848	5970272	6829133	5037864	1822417	0
150	0	16106	254056	187052	0	298337	3232631	6972628	8825197	7298431	3487010	0
200	0	0	251769	260896	0	0	2511280	6423870	8839451	7923370	4403445	516853
250	0	0	234869	266862	0	0	2620746	6514562	8763012	7638730	4031245	243934
300	0	4457	208647	204570	0	505917	2869460	5765034	7058453	5706661	2672191	5295
350	0	23573	195357	287789	65429	710094	2405646	4315273	4847190	3473776	1153211	0
400	13330	71725	148464	264635	373516	796331	1480697	2067370	2020328	1281413	305178	0

Table C.9: Measured particle size distributions $\left(dN/dlogD_p\right)$ of emitted soot for Flame F impinging on a cold surface.

Surface Height (mm)	11.5 nm (#/cm3)	15.4 nm (#/cm3)	20.5 nm (#/cm3)	27.4 nm (#/cm3)	36.5 nm (#/cm3)	48.7 nm (#/cm3)	64.9 nm (#/cm3)	86.6 nm (#/cm3)	115.5 nm (#/cm3)	154 nm (#/cm3)	205.4 nm (#/cm3)	273.8 nm (#/cm3)
100	3211	93229	233010	369332	474801	1385441	3021085	4516869	4579451	2959467	675663	0
150	0	41088	259957	304518	23777	1174405	4033271	7173735	8120996	5961787	2154837	0
200	0	10873	300940	323417	0	777274	3956351	7747467	9216045	7062588	2796594	0
250	0	220	313888	347182	0	814663	4351240	8579025	10193459	7750537	2970040	0
300	0	11545	300649	373591	14855	1009087	4213561	7924821	9206940	6854403	2491620	0
350	1808	56119	239104	375220	290263	1185407	3141448	5164878	5561103	3816238	1070536	0
400	13207	65731	147427	272692	340290	669508	1252324	1785311	1772652	1115254	213652	0

Table C.10: Measured particle size distributions $\left(dN/dlogD_p\right)$ of emitted soot for Flame G impinging on a cold surface.

Surface Height (mm)	11.5 nm (#/cm3)	15.4 nm (#/cm3)	20.5 nm (#/cm3)	27.4 nm (#/cm3)	36.5 nm (#/cm3)	48.7 nm (#/cm3)	64.9 nm (#/cm3)	86.6 nm (#/cm3)	115.5 nm (#/cm3)	154 nm (#/cm3)	205.4 nm (#/cm3)	273.8 nm (#/cm3)
100	82132	192780	292970	620222	1034688	1689395	2389500	2740261	2275141	1127971	0	0
150	14454	129866	307428	548510	761405	1935337	3955935	5768008	5801692	3749970	871881	0
200	0	73988	331665	466096	327444	1594652	4346623	7160691	7659046	5194779	1400596	0
250	0	77503	333867	397862	346138	1910927	5033287	8069880	8494539	5705871	1530143	0
300	0	64009	310210	473194	436360	1919360	4917082	7866875	8254205	5488412	1388471	0
350	5815	98630	248748	437644	622693	1513529	2988569	4253786	4148208	2554516	470487	0
400	21141	60896	120534	238882	328078	594669	1015162	1369953	1307000	796000	147219	0

Table C.11: Measured particle size distributions $\left(dN/dlogD_p\right)$ of emitted soot for Flame G impinging on a cold surface.

Surface Height (mm)	11.5 nm (#/cm3)	15.4 nm (#/cm3)	20.5 nm (#/cm3)	27.4 nm (#/cm3)	36.5 nm (#/cm3)	48.7 nm (#/cm3)	64.9 nm (#/cm3)	86.6 nm (#/cm3)	115.5 nm (#/cm3)	154 nm (#/cm3)	205.4 nm (#/cm3)	273.8 nm (#/cm3)
100	79061	177416	262144	571571	903125	1254302	1508221	1514479	1092149	397507	0	0
150	51328	125066	181708	372039	626112	906225	1098555	1086506	783828	309252	0	0
200	57728	155560	247265	510443	840247	1315636	1783761	1974380	1584738	740379	0	0
250	73766	210713	368267	770230	1272735	2153778	3155764	3701070	3080528	1491049	0	0
300	34464	208654	406948	735610	1222659	2395332	3922631	4916586	4297675	2223141	7295	0
350	60346	146004	256380	589625	950008	1601381	2386390	2866649	2441463	1214210	11309	0
400	28480	78022	119518	239555	383407	618776	879539	1018384	853276	427537	6573	0

Table C.12: Measured particle size distributions $\left(dN/dlogD_p\right)$ of emitted soot for Flame I impinging on a cold surface.

Surface Height (mm)	11.5 nm (#/cm3)	15.4 nm (#/cm3)	20.5 nm (#/cm3)	27.4 nm (#/cm3)	36.5 nm (#/cm3)	48.7 nm (#/cm3)	64.9 nm (#/cm3)	86.6 nm (#/cm3)	115.5 nm (#/cm3)	154 nm (#/cm3)	205.4 nm (#/cm3)	273.8 nm (#/cm3)
138	0	22082	345561	326051	0	1022887	5267998	10316736	12364068	9652209	4068213	0
206	0	2098	364293	300348	0	641365	5033447	10519129	13091853	10652838	4937669	0
275	0	0	311960	292160	0	523587	4443362	9441735	11940692	9920647	4810398	39262
345	0	1974	283394	301618	0	992443	4597283	8851076	10564694	8252011	3500515	0
413	0	47307	245593	362138	331963	1478627	3826162	6198516	6671953	4725510	1641830	0
482	25639	98230	226313	493665	725988	1466679	2654570	3704271	3703889	2472109	734913	0
550	16674	111266	263738	515920	726652	1438961	2589915	3596563	3562620	2328302	625970	0

Table C.13: Measured particle size distributions $\left(dN/dlogD_p\right)$ of emitted soot for Flame J impinging on a cold surface.

Surface Height (mm)	11.5 nm (#/cm3)	15.4 nm (#/cm3)	20.5 nm (#/cm3)	27.4 nm (#/cm3)	36.5 nm (#/cm3)	48.7 nm (#/cm3)	64.9 nm (#/cm3)	86.6 nm (#/cm3)	115.5 nm (#/cm3)	154 nm (#/cm3)	205.4 nm (#/cm3)	273.8 nm (#/cm3)
100	0	14142	308062	362298	0	1174440	4769532	8855305	10152578	7466723	2682627	0
150	0	7949	298208	340048	0	1088535	4660337	8824848	10399463	8006966	3303729	0
200	0	0	290802	330609	0	1010376	4663499	9026482	10887043	8639382	3809243	0
250	0	0	271312	340949	1153	1196990	4762065	8902983	10526277	8186375	3452532	0
300	0	36323	230469	375708	333679	1424444	3724611	6112741	6705005	4866152	1780711	0
350	23978	89555	194523	420967	637469	1169419	1962045	2634842	2611204	1771800	586735	0
400	34487	105375	204997	435337	675175	1149413	1777749	2242968	2094096	1303794	309577	0

Table C.14: Measured particle size distributions $\left(dN/dlogD_p\right)$ of emitted soot for Flame K impinging on a cold surface.

Surface Height (mm)	11.5 nm (#/cm3)	15.4 nm (#/cm3)	20.5 nm (#/cm3)	27.4 nm (#/cm3)	36.5 nm (#/cm3)	48.7 nm (#/cm3)	64.9 nm (#/cm3)	86.6 nm (#/cm3)	115.5 nm (#/cm3)	154 nm (#/cm3)	205.4 nm (#/cm3)	273.8 nm (#/cm3)
100	0	62567	269075	379630	342886	1598043	4150754	6693428	7141019	4915241	1459267	0
150	0	51020	267486	407303	322331	1483792	3982275	6581489	7196904	5151631	1778833	0
200	0	24968	320391	443893	201751	1737167	5240374	8983479	10004326	7250275	2537687	0
250	0	8364	320639	432656	84089	1785810	5883223	10358294	11692995	8595744	3146724	0
300	0	59724	266962	460470	525398	1864333	4457163	6994686	7384630	5090515	1584321	0
350	29218	97094	210460	447118	601383	1089370	1904481	2649667	2649044	1753902	492237	0
400	50084	120608	201145	446187	664640	978470	1343063	1581891	1408690	828687	150153	0

Table C.15: Measured particle size distributions $\left(dN/dlogD_p\right)$ of emitted soot for Flame L impinging on a cold surface.

Surface Height (mm)	11.5 nm (#/cm3)	15.4 nm (#/cm3)	20.5 nm (#/cm3)	27.4 nm (#/cm3)	36.5 nm (#/cm3)	48.7 nm (#/cm3)	64.9 nm (#/cm3)	86.6 nm (#/cm3)	115.5 nm (#/cm3)	154 nm (#/cm3)	205.4 nm (#/cm3)	273.8 nm (#/cm3)
100	14262	98074	216086	390548	574159	1236483	2275451	3133252	3014382	1843020	327970	0
150	3203	87930	269976	491657	569984	1461610	3162562	4798747	4929052	3243941	819161	0
200	0	73659	349021	598681	636397	2114244	5031249	7884729	8236595	5502719	1450059	0
250	0	30790	357357	534088	353506	2357304	6633195	10988009	11782354	8046134	2274662	0
300	0	55922	299608	439728	539510	2195546	5294533	8230024	8604532	5824564	1651752	0
350	19786	78082	214714	440508	580973	1159370	2149445	3040727	2996072	1887429	398816	0
400	48882	110732	176116	378002	557921	733257	880984	941924	813768	495519	124002	972

Table C.16: Measured particle size distributions $\left(dN/dlogD_p\right)$ of emitted soot for Flame M impinging on a cold surface.

Surface Height (mm)	11.5 nm (#/cm3)	15.4 nm (#/cm3)	20.5 nm (#/cm3)	27.4 nm (#/cm3)	36.5 nm (#/cm3)	48.7 nm (#/cm3)	64.9 nm (#/cm3)	86.6 nm (#/cm3)	115.5 nm (#/cm3)	154 nm (#/cm3)	205.4 nm (#/cm3)	273.8 nm (#/cm3)
100	40031	101542	160727	326923	519302	879977	1318804	1590369	1370971	712359	9871	0
150	33464	103341	184160	364727	536552	972366	1598601	2074531	1897376	1070340	89001	0
200	41442	166281	356957	717310	1040392	1986793	3421558	4573017	4289416	2508359	304727	0
250	34083	213695	460824	912936	1646062	3433221	5800492	7436717	6774191	3870906	406118	0
300	41757	176600	446308	979397	1506706	3181807	5749110	7837041	7441428	4420074	611977	0
350	34083	148460	311102	585617	898134	1701105	2839293	3700470	3448401	2060739	348679	0
400	81637	121897	131199	339061	546632	736827	873168	907742	754088	435742	113372	0

Table C.17: Measured particle size distributions $\left(dN/dlogD_p\right)$ of emitted soot for Flame N impinging on a cold surface.

Surface Height (mm)	11.5 nm (#/cm3)	15.4 nm (#/cm3)	20.5 nm (#/cm3)	27.4 nm (#/cm3)	36.5 nm (#/cm3)	48.7 nm (#/cm3)	64.9 nm (#/cm3)	86.6 nm (#/cm3)	115.5 nm (#/cm3)	154 nm (#/cm3)	205.4 nm (#/cm3)	273.8 nm (#/cm3)
100	0	13893	224087	178788	0	52990	2183339	5111865	6572415	5338115	2316716	0
150	0	1837	227234	188844	0	0	2044557	5156411	6883689	5852344	2858263	0
200	0	15846	246512	184118	0	0	2236534	5402663	6968451	5659840	2482036	0
250	0	67149	274931	214827	0	213059	2516955	5422647	6699808	5278036	2200478	0
300	0	59062	233317	213353	0	356044	2338366	4776420	5804743	4541489	1885728	0
350	0	30886	188863	225546	0	402408	2226865	4485228	5461914	4314318	1847056	0
400	0	30908	180992	213988	1587	583540	2261756	4212760	4946716	3807038	1568023	0

Table C.18: Measured particle size distributions $\left(dN/dlogD_p\right)$ of emitted soot for Flame O impinging on a cold surface.

Surface Height (mm)	11.5 nm (#/cm3)	15.4 nm (#/cm3)	20.5 nm (#/cm3)	27.4 nm (#/cm3)	36.5 nm (#/cm3)	48.7 nm (#/cm3)	64.9 nm (#/cm3)	86.6 nm (#/cm3)	115.5 nm (#/cm3)	154 nm (#/cm3)	205.4 nm (#/cm3)	273.8 nm (#/cm3)
100	0	41693	342455	163321	0	157186	3648557	8022661	9959753	7867769	3297624	0
150	0	3862	365628	214512	0	0	3514731	8423006	10803387	8751784	3858317	0
200	0	17898	368967	201978	0	85211	3642738	8500635	10798232	8668155	3731074	0
250	0	63209	319121	180516	0	449228	3637267	7514048	9192773	7266643	3102942	0
300	0	60012	242939	194253	0	691433	3051191	5782888	6854240	5346044	2290274	0
350	0	15509	213340	254333	0	559238	2842359	5599645	6697662	5184015	2130629	0
400	0	15850	196044	240687	4941	757882	2854320	5259365	6124864	4678988	1909124	0